

Entanglement Generation and Self-Correcting Quantum Memories

INAUGURALDISSERTATION

zur

Erlangung der Würde eines Doktors der
Philosophie

vorgelegt der

Philosophisch-Naturwissenschaftlichen Fakultät
der Universität Basel

von

Beat Röthlisberger
aus Basel (BS), Schweiz

Basel, 2012

Originaldokument gespeichert auf dem Dokumentenserver der Universität Basel
edoc.unibas.ch



Dieses Werk ist unter dem Vertrag „Creative Commons Namensnennung-Keine kommerzielle Nutzung-Keine Bearbeitung 2.5 Schweiz“ lizenziert. Die vollständige Lizenz kann unter

creativecommons.org/licences/by-nc-nd/2.5/ch
eingesehen werden.



Namensnennung-Keine kommerzielle Nutzung-Keine Bearbeitung 2.5 Schweiz

Sie dürfen:



das Werk vervielfältigen, verbreiten und öffentlich zugänglich machen

Zu den folgenden Bedingungen:



Namensnennung. Sie müssen den Namen des Autors/Rechteinhabers in der von ihm festgelegten Weise nennen (wodurch aber nicht der Eindruck entstehen darf, Sie oder die Nutzung des Werkes durch Sie würden entlohnt).



Keine kommerzielle Nutzung. Dieses Werk darf nicht für kommerzielle Zwecke verwendet werden.



Keine Bearbeitung. Dieses Werk darf nicht bearbeitet oder in anderer Weise verändert werden.

- Im Falle einer Verbreitung müssen Sie anderen die Lizenzbedingungen, unter welche dieses Werk fällt, mitteilen. Am Einfachsten ist es, einen Link auf diese Seite einzubinden.
- Jede der vorgenannten Bedingungen kann aufgehoben werden, sofern Sie die Einwilligung des Rechteinhabers dazu erhalten.
- Diese Lizenz lässt die Urheberpersönlichkeitsrechte unberührt.

Die gesetzlichen Schranken des Urheberrechts bleiben hiervon unberührt.

Die Commons Deed ist eine Zusammenfassung des Lizenzvertrags in allgemeinverständlicher Sprache: <http://creativecommons.org/licenses/by-nc-nd/2.5/ch/legalcode.de>

Haftungsausschluss:

Die Commons Deed ist kein Lizenzvertrag. Sie ist lediglich ein Referenztext, der den zugrundeliegenden Lizenzvertrag übersichtlich und in allgemeinverständlicher Sprache wiedergibt. Die Deed selbst entfaltet keine juristische Wirkung und erscheint im eigentlichen Lizenzvertrag nicht. Creative Commons ist keine Rechtsanwalts-gesellschaft und leistet keine Rechtsberatung. Die Weitergabe und Verlinkung des Commons Deeds führt zu keinem Mandatsverhältnis.

Genehmigt von der Philosophisch-Naturwissenschaftlichen
Fakultät auf Antrag von

Prof. Dr. Daniel Loss

Prof. Dr. Jiannis Pachos

Basel, den 18. Oktober 2011

Prof. Dr. M. Spiess
Dekan

Acknowledgments

I would like to thank my advisor Prof. Daniel Loss for accepting me as a student in his group and for allowing me to work on the interesting research topics covered in this thesis. I am truly grateful for the firm guidance, support, advice, and last but not least, appreciation I was fortunate enough to receive from him. Although the times as a young PhD student were sometimes challenging, they were mostly exciting and fun. My thanks also go to Prof. Jiannis Pachos for co-refereeing this thesis and for his collaboration in our work on random lattices.

The work in the following chapters could not have been achieved without the help of the brilliant researchers I had the pleasure to collaborate with over the past few years. My deepest acknowledgments go to Dr. Stefano Chesi, Dr. Jörg Lehmann, Dr. Daniel Saraga, and Dr. James Wootton for their patience and support, and for sharing their insight.

As I am writing these lines, I am remembering countless enjoyable moments with group members and frequent visitors – Samuel Aldana, Daniel Becker, Massoud Borhani, Dan Bohr, Bernd Braunecker, Christoph Bruder, Denis Bulaev, Guido Burkard, Oleg Chalaev, Stefano Chesi, Luca Chirolli, Bill Coish, Anthony Clark, Charles Doiron, Mathias Duckheim, Carlos Egues, Alexander Eichler, Sigurdur Erlingsson, Javad Farahani, Gerson Ferreira, Jan Fischer, Suhas Gangadharaiah, Vitaly Golovach, Marco Hachiya, Kevin van Hoogdalem, Adrian Hutter, Daniel Klauser, Jelena Klinovaja, Christoph Klöffel, Verena Körting, Yong Li, Franziska Maier, Dmitrii Maslov, Andreas Nunnenkamp, Fabio Pedrocchi, Joël Peugiron, Felipe Penha, Poliana Penteado, Diego Rainis, Maximilian Rink, Daniel Saraga, Manuel Schmidt, Thomas Schmidt, Pascal Simon, Dimitrije Stepanenko, Vladimir M. Stojanovic, Grégory Strübi, Björn Trauzettel, Mircea Trif, Luka Trifunovic, Filippo Troiani, Yaroslav Tserkovnyak, Oleksandr Tsyplyatyev, Andreas Wagner, Ying-Dan Wang, James Wootton, Robert Žak, Robert Zielke, Oded Zilberberg, and Dominik Zumbühl – many of whom have become close friends.

Last but not least, I would like to thank my parents for their everlasting support.

Contents

Contents	vii
1 Introduction	1
I Entanglement Measures & Highly Entangled States	
2 Tripartite Systems	9
2.1 Introduction	9
2.2 Model	10
2.3 Ground-state properties	12
2.4 Entanglement measure	13
2.5 Numerical evaluation	14
2.6 Finite temperature	15
2.7 Conclusion	18
3 Algorithms and Multipartite Systems	19
3.1 Introduction	20
3.2 Convex-roof entanglement measures as constrained optimization problems	22
3.3 Numerical algorithms	25
3.4 Physical application	35
3.5 Conclusion	41
4 The Optimization Library libCreme	43
4.1 Introduction	43
4.2 Entanglement measures included in the library	48
4.3 Theoretical background	50
4.4 Optimization algorithms	54
4.5 Examples	61
4.6 Conclusion	65

II Self-Correcting Quantum Memories

5	Extending Kitaev's Toric Code with Long-Range Interactions	69
5.1	Introduction	69
5.2	Repulsive long range interactions in the Kitaev model . . .	71
5.3	Error models and simulations	73
5.4	Diffusion of anyons and memory lifetime	75
5.5	Mean-field analysis of the interacting model	79
5.6	Dynamics of the interacting model	83
5.7	Discussion of the long range interaction	87
5.8	Conclusion	90
6	Incoherent Dynamics in the Toric Code Subject to Disorder	91
6.1	Introduction	91
6.2	Review of the 2D toric code	93
6.3	Classical dynamics and numerical simulations	95
6.4	Random lattices	97
6.5	Random onsite potentials	104
6.6	Quantum dynamics	108
6.7	Conclusion	111

Appendix

A	Derivatives of the Meyer-Wallach Entanglement Measure	115
B	Derivatives of Entanglement Measures	117
B.1	Entropy of entanglement	117
B.2	Three-tangle	119
B.3	Meyer-Wallach measure	119
C	Derivatives of the Function $h(U)$	121
D	Self-Correcting Quantum Memories	123
D.1	Mapping from lattice gas to Ising model	123
D.2	Lifetime in the presence of a single pair	124
D.3	Effective Hamiltonian via Schrieffer-Wolff transformation .	125
E	Critical Fraction of Random Lattices in Contact with an Ohmic Bath	127
F	Gaussian Noise and $1/r$ Interaction	129
G	Supporting Simulations	131
G.1	Polarized Ising randomness	131
G.2	Artificial cutoff of number of anyons	131
	Bibliography	135

Introduction

Adapted from the introductory chapters of:
R. A. Žak, B. Röthlisberger, S. Chesi, and D. Loss,
“Quantum Computing with Electron Spins in Quantum Dots”,
La Rivista del Nuovo Cimento **33**, 7 (2010).

The vision of a quantum-mechanical device performing calculations has its origin in the search for the ultimate computer: What universal machine can efficiently simulate all conceivable algorithmic processes that can, in principle, be carried out in nature? It was not until the eighties of the last century that people began to leave the – by then – familiar and well established territory of classical information theory in order to explore what more fundamental answers the quantum world might have to offer. After all, if nature is ultimately quantum, should a computer based on the principles of quantum mechanics not be at least equally, if not even more powerful than a classical computer [DiV00]? Researchers such as Feynman [Fey82, Fey86] and Deutsch [Deu85] believed that the answer to this question is indeed affirmative when they were envisioning and formalizing the notion of such a *quantum computer* together with its potential applications for the first time.

These early ideas came along hand in hand with major developments in research and industry that had a tremendous influence on the future course of quantum computing. On the one hand, groundbreaking experiments [AGR81, AGR82] confirmed that Nature indeed exhibits peculiar nonlocal behavior whose existence was heavily debated since the early days of quantum mechanics [EPR35]. It was Schrödinger [Sch35] who termed this phenomenon *entanglement*, thereby trying to capture the intricate ‘tangle’ that individual parties can find themselves in as a *part of the whole* within a global quantum state. Entanglement is a ubiquitous

and arguably the most crucial ingredient in the newly emerged field of quantum computer science [NC00, Mer07, Ved07]. On the other hand, the boom in computer industry led to major progress in semiconductor and laser technology. This is another requirement for building a quantum computer, since the latter demands the ability to fabricate, address and coherently manipulate single quantum systems.

Despite all of the development during the past thirty years, building a working quantum computer that is able to perform useful calculations remains a challenge. With this thesis, we are trying to contribute a small piece to this puzzle by addressing three of the many fundamental questions one encounters along the way of reaching that goal. These questions are:

- (i) What is an easy way to create highly entangled states as a resource for quantum computation?
- (ii) What can we do to efficiently quantify states of noisy entanglement in systems coupled to the outside world?
- (iii) How can we protect and store fragile quantum states for arbitrary long times?

The first two questions are the subject of part one of this thesis, ‘Entanglement Measures & Highly Entangled States’, whereas the third question is addressed in part two, ‘Self-Correcting Quantum Memories’. In the following, we would like to give a short motivation for studying these topics along with an outline of the corresponding research presented in the rest of the thesis.

Creating Highly Entangled Quantum States

Another term for ‘entanglement’ is ‘quantum correlations’, implying that there is something more behind it than just ‘classical correlations’. Indeed, Bell [Bel64] has shown that within any physical theory based on *reality* (observables have definite values independent of whether they are being measured or not) and *locality* (measurements cannot immediately influence each other if they are sufficiently far apart), certain correlations of measurement outcomes satisfy an inequality that is violated by quantum mechanics. One can thus think of entangled states as those that contain such strong correlations, stronger than any classical correlations could ever be [¹].

More formally, a pure state $|\psi\rangle$ of an m -partite quantum system is called *entangled* if and only if it is not separable [HHHH09], i.e. if it cannot

¹Admittedly, this is not perfectly true, as there are states known that are entangled in the mathematical sense, but still admit a hidden variable model within local realistic theories [Wer89].

be written in the form

$$|\psi\rangle = |\phi_1\rangle \otimes |\phi_2\rangle \otimes \dots \otimes |\phi_m\rangle, \quad (1.1)$$

where the $|\phi_i\rangle \in \mathcal{H}_i$, $i = 1, \dots, m$, are states of the m Hilbert spaces \mathcal{H}_i associated with the m individual systems. Within the context of mixed states, a state ρ is analogously said to be entangled if it cannot be expressed as

$$\sum_{j=1}^K p_j \rho_1^j \otimes \rho_2^j \otimes \dots \otimes \rho_m^j. \quad (1.2)$$

Here, the integer K (sometimes called ‘cardinality’) satisfies $K \geq \text{rank } \rho$, the p_j ’s are normalized probabilities and the ρ_i^j ’s are density operators acting on the Hilbert spaces \mathcal{H}_i .

Some states are more entangled than others. In the context of Bell inequalities, this translates into the notion that such states contain stronger non-classical correlations and thus violate Bell inequalities by a higher amount. But also the strength of these quantum correlations is limited, and states that do reach this upper bound are said to be maximally non-local. In the case of two qubits [2] with individual basis states labeled by $|\uparrow\rangle$ and $|\downarrow\rangle$, they read

$$|\psi^\pm\rangle = (|\uparrow\rangle \otimes |\downarrow\rangle \pm |\downarrow\rangle \otimes |\uparrow\rangle) / \sqrt{2}, \quad (1.3)$$

$$|\phi^\pm\rangle = (|\uparrow\rangle \otimes |\uparrow\rangle \pm |\downarrow\rangle \otimes |\downarrow\rangle) / \sqrt{2}, \quad (1.4)$$

and are typically called Bell states or Einstein-Podolski-Rosen (EPR) pairs [EPR35]. Analogously, maximally non-local states of m qubits are of the form

$$|\psi\rangle = (|\uparrow\uparrow \dots \uparrow\rangle + |\downarrow\downarrow \dots \downarrow\rangle) / \sqrt{2} \quad (1.5)$$

or local unitary transformations thereof. Consequently, it is natural to define maximally entangled states as exactly those that are of the above form.

As mentioned earlier, entanglement plays a central role within the theory of quantum information. Virtually all protocols and algorithms performing non-classical computations and communication tasks require access to a source of highly or even maximally entangled states [NC00, Mer07]. Furthermore, entanglement has become understood to be a *resource* that can be distilled, shared, and sometimes even irreversibly lost (see, e.g., [HHHH09] for a recent review).

Apart from the use in quantum information theory, highly entangled states also play the key role in experiments that try to verify the fundamental concepts of quantum mechanics. Especially noteworthy in this context is the maximally entangled state of *three* qubits, because it can be used to test certain non-intuitive predictions of quantum mechanics

²A qubit is a quantum two-level system.

in *single-shot* experiments [Mer90, Mer93], as opposed to the averaging over many measurements required by Bell inequalities.

The first part of this thesis is devoted to a particular proposal for generating entanglement within a solid-state setup, starting in chapter 2 with the tripartite case and continuing in chapter 3 with a generalization to four and more qubits. The main idea there is to realize systems with highly entangled ground states in order for entanglement to be created by merely cooling to low enough temperatures. We have found such states in Heisenberg exchange-coupled spin rings of the form

$$H = -J \sum_{i=1}^N \mathbf{S}_i \cdot \mathbf{S}_{i+1} + b \sum_{i=1}^N (S_i^x \cos \alpha_i + S_i^y \sin \alpha_i), \quad (1.6)$$

where the \mathbf{S}_i 's are the vectors of spin- $\frac{1}{2}$ matrices associated with spins $i = 1, \dots, N$, satisfying $\mathbf{S}_{N+1} \equiv \mathbf{S}_1$ to close the loop. The angles α_k are given by

$$\alpha_k = 2\pi(k-1)/N, \quad k = 1, \dots, N, \quad (1.7)$$

and parameterize the directions of local magnetic fields pointing radially outwards the ring. For ferromagnetic coupling between the spins ($J > 0$) and weak magnetic fields ($b \ll J$), a highly entangled ground state emerges as a tunnel doublet from the two degenerate classical configurations given by all spins aligned along a direction perpendicular to the plane of the ring.

However, the nature of these systems poses an intricate obstacle: On the one hand, the maximally entangled ground states are obtained perfectly only in the limit where the strength b of the external magnetic fields goes to zero. On the other hand, the ground-state energy gap vanishes in the same limit. At non-zero temperature, we therefore have to identify the optimal value of b that separates the ground state sufficiently from excited states, but at the same time does not disturb it too much.

We have addressed this issue by numerically calculating mixed-state entanglement measures [PV07] and maximizing the latter as a function of b . These measures are functions that try to quantify the amount of entanglement in a given state. While there are many entanglement measures for pure states that can be evaluated in a straight-forward manner, mixed states bring along the additional complication that their decomposition into pure states is not unique. This results in a particular optimization problem with non-linear constraints that has to be solved for each density matrix of interest. This task was considered to be rather involved [PV07], and no general procedures were known that could deal with it in an efficient way. A large fraction of the first part of this thesis (esp. chapter 3) is thus actually concerned with the development of algorithms that can be used to calculate entanglement measures of mixed states. These

techniques are then in turn employed to analyze the kind of spin systems we have originally started with.

The research along these lines has led to the development of the numerical library `libCreme`, presented in chapter 4. It can handle a broad family of mixed-state entanglement measures – so-called *convex-roofs* – [Uhl00] and is written in a user-friendly and easily extendable way. We hope that the publication of the code will prove to be a useful contribution for other researchers studying entanglement of mixed states.

Self-Correcting Quantum Memories

The second part of the thesis addresses the question how to reliably store quantum states long enough to perform useful calculations. Every computer, be it classical or quantum, needs the information it processes to be protected from corruption caused by faulty gates and perturbations from interactions with its environment. However, quantum states are much more susceptible to these adverse effects than classical states, making the manipulation and storage of quantum information a challenging task. Therefore, and despite the fact that coherence times of physical qubits have been constantly increasing over recent years, the use of *quantum error correction* still is, and probably always will be an unavoidable prerequisite for the realization of a large-scale quantum computer.

The main idea of quantum error-correcting codes is to encode a logical state in a Hilbert space of a larger number of physical qubits [Pre98]. This redundancy can then be exploited to check the system for the occurrence of errors without disturbing the encoded state. If such a *syndrome measurement* is positive, the corresponding error can be corrected, thus bringing the system back into its original uncorrupted state. In this way, the encoded state of a quantum computation can in principle be protected by actively monitoring it with sufficiently high frequency and correcting errors whenever necessary. Unfortunately, this procedure brings along a substantial overhead and thereby makes an already involved endeavor even more complicated.

A therefore desirable alternative approach is to encode information in physical systems that already possess some kind of ‘built-in’ error protection mechanism [DKLP02]. The prime source of inspiration in this context is the storage of classical information (in the form of bits) as the magnetization direction of small magnetic regions. In the ordered phase of such systems, the ferromagnetic exchange interaction favors spin flips caused by thermal fluctuations to be reverted rather than spread further across the system. A spontaneous change of the magnetization thus becomes less and less likely for increasing system size and is virtually impossible already at microscopic length scales. Analogously, a *self-correcting quantum memory* would be a system that could store encoded quantum states for arbitrary long times at large enough system size.

Promising candidates for this are systems exhibiting *topological order*, because they are robust against local perturbations, and information encoded in the ground state can only be manipulated in a non-local fashion [NO09]. In this context, arguably the best studied model is Kitaev's toric code [Kit03]. Its Hamiltonian consists of a sum of mutually commuting local four-body spin operators defined on a lattice with periodic boundary conditions, a *torus*. Encoded states can only be manipulated by applying string-like logical operators that fully wrap around the torus. A major drawback of the toric code is though, that it is not stable within a thermal environment [NO08, KC08, AFH09, BT09, CLBT09]. Its elementary excitations, which are frozen out at zero temperature T , can diffuse freely on the surface of the torus for any $T \neq 0$. While doing so, these so-called *anyons* leave behind traces of errors that eventually act as random logical operators, therefore irreversibly corrupting any encoded information.

In chapter 5, we extend the toric code by repulsive long-range interactions between the anyons and show that this makes the code stable against thermal fluctuations. The reason for this is the suppression of the anyon density with increasing system size. The excitation energy diverges in the thermodynamic limit, thus keeping the system free of anyons essentially forever. We obtained our results from an analytical mean-field analysis on the one hand, and extensive numerical simulations of the anyon dynamics on the other. An important conclusion of our work, besides showing that this type of model is self-correcting, is that the increase of the lifetime is very sensitive to the nature of the thermal environment. The most favorable case turns out to be a super-Ohmic bath, where not only the density, but also the diffusion of anyons is suppressed by the interactions.

Finally, the last chapter of this thesis focusses on incoherent effects of quenched disorder in the toric code and similar systems. First, we numerically determine the error thresholds, that is, the fraction of errors for which the system becomes uncorrectable, in codes obtained from randomly modifying the syndrome operators of the toric code in a specific way. It is shown that these random lattice models are advantageous over the toric code in the presence of biased noise, where spin flip and phase flip errors occur with different probabilities. We further argue that these codes have error thresholds close to the fundamental upper bound valid for a large class of error-correcting codes. Second, we look at the influence of randomness in the anyon onsite energies of Kitaev's toric code. We have discovered that an increase in the strength of this randomness can extend the lifetime of encoded states. We then explain this effect with the disorder-induced suppression of the anyon diffusion.

Part I

Entanglement Measures & Highly Entangled States

CHAPTER 2

Tripartite Systems

Adapted from:

B. Röthlisberger, J. Lehmann, D. S. Saraga, P. Traber, and D. Loss,
“Highly Entangled Ground States in Tripartite Qubit Systems”,
Phys. Rev. Lett. **100**, 100502 (2008).

In this chapter, we investigate the creation of highly entangled ground states in a system of three exchange-coupled qubits arranged in a ring geometry. Suitable magnetic field configurations yielding approximate GHZ and exact W ground states are identified. The entanglement in the system is studied at finite temperature in terms of the mixed-state tangle τ . By generalizing a conjugate gradient optimization algorithm originally developed to evaluate the entanglement of formation, we demonstrate that τ can be calculated efficiently and with high precision. We identify the parameter regime for which the equilibrium entanglement of the tripartite system reaches its maximum.

2.1 Introduction

Entangled quantum systems have been the focus of numerous theoretical and experimental investigations [EPR35, Bel64, AGR82, Wer89, GHZ89, DVC00]. In particular, entanglement has been identified as the primary resource for quantum computation and communication [NC00]. Compared to the case of a bipartite system, multipartite entanglement exhibits various new features. Notably, there are two different equivalence classes of genuine three-qubit entanglement [DVC00], the representatives being any one of the two maximally entangled Greenberger-Horne-Zeilinger (GHZ) states [GHZ89] $|\text{GHZ}^\pm\rangle = (|\uparrow\uparrow\uparrow\rangle \pm |\downarrow\downarrow\downarrow\rangle)/\sqrt{2}$ on the one hand, and the W state [DVC00] $|W\rangle = (|\uparrow\uparrow\downarrow\rangle + |\uparrow\downarrow\uparrow\rangle + |\downarrow\uparrow\uparrow\rangle)/\sqrt{3}$ on the other.

The ability to realize both representatives in real physical systems is thus of high importance in the study of genuine tripartite entanglement. Particularly interesting is the GHZ state, as it represents the strongest quantum correlations possible in a system of three qubits. Furthermore, it is equivalent to the three-qubit cluster state used in one-way quantum computation [RBB03]. It is favorable to obtain the GHZ and W states as the eigenstate of a suitable system, rather than by engineering them using quantum gates. In this chapter, we demonstrate the possibility of obtaining approximate GHZ and exact W states as the ground state of three spin-qubits in a ring geometry coupled via an anisotropic Heisenberg interaction. The use of quantum gates is therefore not required. Rather, the desired states are achieved merely by cooling down to sufficiently low temperatures. We state all our results in terms of the exchange coupling strengths in order to keep our proposal open to a broad set of possible implementations of the qubits. We remark that, while Heisenberg models have been studied frequently in the context of entanglement [Bos03] (also with respect to entangled eigenstates [RR02]), this is the first time that highly entangled states are reported as the non-degenerate ground state of three exchange-coupled qubits.

Our study inevitably involves the issue of quantifying entanglement [PV07, MCKB05, BDSW96, CKW00, WG03]: At finite temperatures, the mixing of the ground state with excited states forces us to evaluate a mixed-state entanglement measure in order to study the entanglement in the system meaningfully. Computationally, this is a rather formidable task. We generalize a numerical scheme that has originally been developed to compute the entanglement of formation [BDSW96, AVDM01]. Our scheme can be used to evaluate *any* mixed-state entanglement measure defined as a so-called convex roof [Uhl00].

2.2 Model

We assume that three spins \mathbf{S}_i , with $S = 1/2$, are located at the corners $i = 1, 2, 3$ of an equilateral triangle lying in the xy -plane. Their interaction is described by the anisotropic Heisenberg Hamiltonian

$$H = -J_{xy} \sum_{i=1}^3 (S_i^x S_{i+1}^x + S_i^y S_{i+1}^y) - J_z \sum_{i=1}^3 S_i^z S_{i+1}^z + H_Z, \quad (2.1)$$

where $\mathbf{S}_4 = \mathbf{S}_1$. Here, J_{xy} and J_z are the in- and out-of-plane exchange coupling constants, respectively, and $H_Z = \sum_{i=1}^3 \mathbf{b}_i \cdot \mathbf{S}_i$ denotes the Zeeman coupling of the spins \mathbf{S}_i to the externally applied magnetic fields \mathbf{b}_i at the sites i [1]. We now seek a configuration of \mathbf{b}_i 's yielding a highly

¹Depending on the actual implementation of the qubits, \mathbf{b}_i can denote an effective magnetic field.

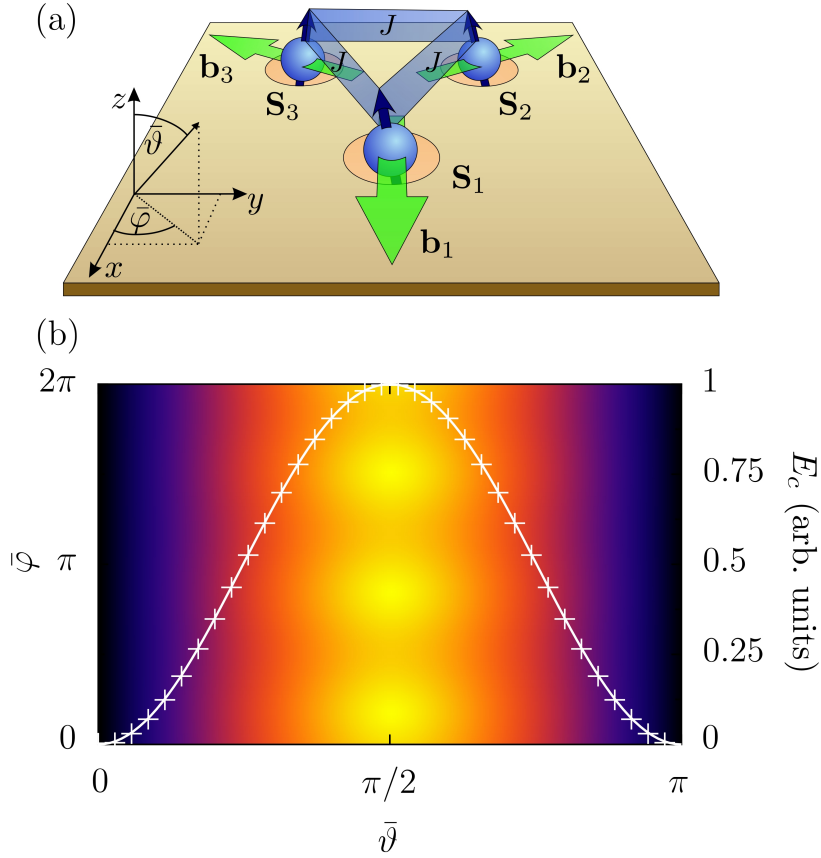


Figure 2.1: (a) Schematic depiction of the system described by the Hamiltonian (2.1) for $J_{xy} = J_z = J$ and radial magnetic field configuration. Three spins S_i are situated at the corners of an equilateral triangle and are ferromagnetically exchange-coupled with coupling strength J . Local radial in-plane magnetic fields b_i (shown as green arrows in the xy -plane) point radially outwards. As discussed in the text, any other in-plane field geometry obeying the same radial symmetry (such as, e.g., a ‘chiral’ field looping around the triangle) leads to equivalent results. (b) Classical energy surface E_c of the system shown in the top panel. The ‘mean’ angles $\bar{\vartheta}$ and $\bar{\varphi}$ (introduced in the top panel) are well suited to characterize the state of the system since fluctuations around these angles are small for $b \ll J$ and sum to zero. The superimposed white line shows the perturbatively calculated energy barrier at $\bar{\varphi} = \pi/2$ [see Eq. (2.2)], whereas the crosses are due to a corresponding numerical minimization of the energy.

entangled GHZ- or W-type *ground state*. Finite-temperature effects will then be studied in a second step.

2.3 Ground-state properties

We first consider isotropic exchange couplings, i.e., $J_{xy} = J_z \equiv J$. For $\mathbf{b}_i = 0$, we naturally find two fourfold-degenerate eigenspaces due to the high symmetry of the system. For $J > 0$, i.e., ferromagnetic coupling, the ground-state quadruplet is spanned by the two GHZ states $|\text{GHZ}^\pm\rangle$, the W and the spin-flipped W state. Appropriately chosen magnetic fields allow one, however, to split off an approximate GHZ state from this degenerate eigenspace. To identify the optimal field geometry, we first observe that the two states $|\text{GHZ}^\pm\rangle$ have the form of a tunnel doublet. If we thus find a set of \mathbf{b}_i 's, which, in the classical spin system, results in precisely two degenerate minima for the configurations $\uparrow\uparrow\uparrow$ and $\downarrow\downarrow\downarrow$ with an energy barrier in between, quantum tunneling will yield the desired states. In order to single out exactly the two directions perpendicular to the xy -plane, the magnetic fields must be in-plane, be of the same strength, and sum to zero. This immediately implies that successive directions of the fields must differ by an angle of $2\pi/3$ from each other. We choose the fields to point radially outwards [see Fig. 2.1], although any other configuration possessing the required symmetry is equivalent. However, this setup is experimentally most feasible, e.g., by placing a bar magnet below the center of the sample (in the case of a solid state implementation). In order to favor parallel spin configurations we consider the regime where $J \gg b$, $b = |\mathbf{b}_i|$ being the Zeeman energy. We may thus assume that for given mean spherical angles $\bar{\vartheta}$ (zenith) and $\bar{\varphi}$ (azimuth), the orientation of each spin will deviate from these values only by a small amount. Expanding the classical energy $E_c(\bar{\vartheta}, \bar{\varphi})$ corresponding to Eq. (2.1) to second order in these deviations and minimizing with respect to them under the constraint that they separately sum to zero yields:

$$E_c \approx -\frac{(b/J)^2}{8}(3 + \cos 2\bar{\vartheta}) + \frac{(b/J)^3}{24} \sin(3\bar{\varphi}) \sin^3 \bar{\vartheta}. \quad (2.2)$$

This expression is minimal for $\bar{\vartheta} = 0$ and $\bar{\vartheta} = \pi$, representing the desired configurations. The paths in $\bar{\vartheta}$ with lowest barrier height connecting these two minima are found for values of $\bar{\varphi} = -\pi/6 + 2\pi n/3 \pmod{2\pi}$, $n = 0, 1, 2$, reflecting the rotational symmetry of the system [see Fig. 2.1]. The corresponding barrier height is approximately given by $[(b/J)^2 - (b/J)^3/6]/4$ [2].

Next we return to the quantum system. The Hamiltonian (2.1) with isotropic exchange coupling J and radial magnetic field can be diagonalized exactly. Expanding for $b/J \ll 1$, the overlap probabilities of the

²Using semiclassical path integration techniques [LDG92], we can calculate the tunnel splitting from Eq. (2.2). However, such a procedure gives accurate results only for large spins ($S \gg 1$) and is thus not pursued here.

exact ground state $|0\rangle$ with $|\text{GHZ}^+\rangle_{\text{l.u.}}$ and the exact first excited state $|1\rangle$ with $|\text{GHZ}^-\rangle_{\text{l.u.}}$, respectively, are identical to second order and are given by ${}_{\text{l.u.}}\langle\text{GHZ}^+|0\rangle|^2 = {}_{\text{l.u.}}\langle\text{GHZ}^-|1\rangle|^2 \approx 1 - \frac{1}{3}(b/J)^2$ ('l.u.' indicates that the states are equivalent to GHZ states via local unitary transformations). The associated energy splitting is given by $\Delta E_{0,1} \approx 2(b/J)^3/3$ (see inset of Fig. 2.2). This confirms the above semiclassical considerations in terms of tunnel doublets. Moreover, we see that the ground state can only approximate a GHZ state although this approximation will turn out to be very good even at finite temperatures where mixing with excited states additionally decreases the entanglement. Before discussing this in greater detail, we study the ground-state of the general anisotropic case with $J_{xy} \neq J_z$ in the Hamiltonian (2.1).

When $J_{xy} \neq J_z$ it is possible to generate highly entangled states by applying a spatially uniform magnetic field either perpendicular to or in the xy -plane. Indeed, a field along the z -axis, i.e., $\mathbf{b}_i = b\mathbf{e}_z$, $i = 1, 2, 3$, with $b > 0$ yields an exact W state as ground state if $J_{xy} > 0$ and $b < J_{xy} - J_z$ (note that this implies the condition $J_{xy} > J_z$). The optimal Zeeman energy b_{opt} leading to the highest energy splitting ΔE_{opt} between the ground state and the first excited state is given by $b_{\text{opt}} = (J_{xy} - J_z)/2$. This yields $\Delta E_{\text{opt}} = 3J_{xy}/2$ if $J_z < -2J_{xy}$ and $\Delta E_{\text{opt}} = (J_{xy} - J_z)/2$ otherwise. The W state is thus best realized by choosing $b = b_{\text{opt}}$ together with a temperature sufficiently small compared to ΔE_{opt} . In order to obtain a GHZ state, one has to apply an in-plane magnetic field $\mathbf{b}_i = b\mathbf{e}_x$. In this case we find for $J_z > 0$, $-2J_z < J_{xy} < J_z$ a situation similar to the one in the case of isotropic coupling and radial magnetic field: The ground state converges to a GHZ state for vanishing field but also the energy difference to the first excited state goes to zero in this limit.

2.4 Entanglement measure

Below, we will quantitatively study the effects of finite temperature $T > 0$ on the amount of entanglement present in the system. For this purpose, we evaluate a suitable mixed-state entanglement measure of the canonical density matrix ρ of the system. The three-tangle, or simply *tangle* τ_p (originally called residual entanglement), is an entanglement measure for pure states $|\psi\rangle \in \mathcal{H}_1 \otimes \mathcal{H}_2 \otimes \mathcal{H}_3$ of three qubits. It reads [CKW00]

$$\tau_p(|\psi\rangle) = 4 \det \text{Tr}_{2,3} \rho_p - \mathcal{C}^2(\text{Tr}_3 \rho_p) - \mathcal{C}^2(\text{Tr}_2 \rho_p), \quad (2.3)$$

where $\rho_p = |\psi\rangle\langle\psi|$, Tr_i denotes the partial trace over subsystem i , and \mathcal{C} is the two-qubit concurrence [Woo98]. The tangle takes values between 0 and 1 and is maximal for GHZ states. It is also known that τ_p is an entanglement monotone [DVC00]. The generalization of pure-state monotones to mixed states is given by the so-called convex roof

[Uhl00, MCKB05, LOSU06]. Accordingly, the mixed-state tangle τ is defined as

$$\tau(\rho) = \inf_{\{p_i, |\psi_i\rangle\} \in \mathfrak{D}(\rho)} \sum_i p_i \tau_p(|\psi_i\rangle). \quad (2.4)$$

Here, $\mathfrak{D}(\rho)$ denotes the set of all pure-state decompositions $\{p_i, |\psi_i\rangle\}_{i=1}^K$ of ρ , with $\sum_{i=1}^K p_i |\psi_i\rangle\langle\psi_i| = \rho$, $p_i \geq 0$, $\sum_{i=1}^K p_i = 1$ and $K \geq R = \text{rank } \rho$. The above definition of τ ensures that $\tau(\rho) = \tau_p(|\psi\rangle)$ if $\rho = |\psi\rangle\langle\psi|$, and that τ itself is an entanglement monotone [MCKB05].

2.5 Numerical evaluation

In order to tackle the optimization problem in Eq. (2.4) numerically, the set of all pure-state decompositions $\mathfrak{D}(\rho)$ needs to be given in an explicitly parameterized form. It is known [HJW93, Kir05] that every pure state decomposition $\{p_i, |\psi_i\rangle\}_{i=1}^K$ of ρ is related to a complex $K \times R$ matrix U satisfying the unitary constraint $U^\dagger U = \mathbb{1}_{R \times R}$, i.e., a matrix having orthonormal column vectors [3]. In fact, the set of all such matrices, the so-called Stiefel manifold $St(K, R)$, provides a complete parameterization of all pure-state decompositions $\{p_i, |\psi_i\rangle\}_{i=1}^K \in \mathfrak{D}(\rho)$ of ρ with fixed cardinality K . The minimization problem in Eq. (2.4) can thus be rewritten as

$$f(\rho) = \min_{K \geq R} \inf_{U \in St(K, R)} h(U, \rho), \quad (2.5)$$

where in our case h is the sum over the weighted pure-state tangles with probabilities and state vectors obtained from ρ via the matrix U . Problems of this kind are considered to be extremely difficult to solve in general [PV07]. We have performed the minimization over the Stiefel manifold numerically using the method described below. We have found that the thereby obtained values converge quickly as K is increased, and have thus fixed $K = R + 4$ throughout all of our calculations, yielding an accuracy which is by far sufficient for our purpose (note that decompositions with smaller cardinality are contained as well). The numerical method we used is a generalization of the conjugate gradient algorithm presented in Ref. [AVDM01]. It is however only suited for searching over the unitary manifold $St(K, K)$. At the cost of over-parameterizing the search space, we have to minimize over $K \times K$ matrices using only the first R columns. The iterative algorithm builds conjugate search directions X (skew-hermitian $K \times K$ matrices) from the gradient G at the current iteration point U and the previous search direction using a modified Polak-Ribière update formula. A line search along the geodesic

³Given ρ and U with $U^\dagger U = \mathbb{1}_{R \times R}$, $\{p_i, |\psi_i\rangle\}_{i=1}^K$ is obtained as $p_i = \langle \tilde{\psi}_i | \tilde{\psi}_i \rangle$, $|\psi_i\rangle = (1/\sqrt{p_i}) |\tilde{\psi}_i\rangle$, where $|\tilde{\psi}_i\rangle = \sum_{j=1}^R U_{ij} \sqrt{\lambda_j} |\chi_j\rangle$ and $|\chi_i\rangle$ are the R eigenvectors of ρ with non-zero eigenvalues λ_i .

$g(t) = U \exp(tX)$ going through U in direction X is performed in every step. In Ref. [AVDM01], an analytical expression for the gradient G is given in the case where f is the entanglement of formation. The algorithm is however also applicable to a generic convex-roof entanglement measure f of the form (2.5). We find the matrix elements G_{jk} of the general gradient G to be

$$G_{jk} = (A_{jk} - A_{kj})/2 + i(S_{jk} + S_{kj})/2, \quad (2.6)$$

where

$$A_{jk} = \sum_{i=1}^K \left(\frac{\partial h}{\partial \operatorname{Re} U_{ik}} \operatorname{Re} U_{ij} + \frac{\partial h}{\partial \operatorname{Im} U_{ik}} \operatorname{Im} U_{ij} \right), \quad (2.7)$$

$$S_{jk} = \sum_{i=1}^K \left(\frac{\partial h}{\partial \operatorname{Im} U_{ik}} \operatorname{Re} U_{ij} - \frac{\partial h}{\partial \operatorname{Re} U_{ik}} \operatorname{Im} U_{ij} \right). \quad (2.8)$$

The derivatives of h with respect to the real and imaginary parts of U_{ik} , $\operatorname{Re} U_{ik}$ and $\operatorname{Im} U_{ik}$, respectively, are taken at U and can be evaluated numerically using finite differences. We have tested our implementation by comparing our numerical results to known analytical results. The maximal encountered absolute error was smaller than 10^{-13} for the entanglement of formation of isotropic 2×2 states [TV00], 10^{-12} for 3×3 states and 10^{-10} for the tangle of a GHZ/W mixture [LOSU06]. This suggests that, although our method can only provide an upper bound, this bound is very tight. It was shown only recently that also a (typically tight) lower bound on any entanglement monotone can be estimated using entanglement witnesses [GRW07, EBaA07]. This is an interesting subject which is left for future research.

2.6 Finite temperature

We return to the study of the three qubits described by the Hamiltonian (2.1). Using the generalized conjugate gradient algorithm, we are able to investigate the entanglement as a function of the temperature T , the magnetic field strength b and the exchange couplings J_{xy} and J_z by calculating the mixed-state tangle $\tau(\rho)$, where $\rho = \exp(-H/k_B T) / \operatorname{Tr} \exp(-H/k_B T)$ is the canonical density matrix of the system. To our knowledge, this is the first time that $\tau(\rho)$ has been evaluated for states arising from a physical model. Our main goal now is to maximize the entanglement as a function of $b \equiv |\mathbf{b}_i|$, i.e., the Zeeman energy. For this purpose we consider only GHZ states in the following, since our W ground states are b -independent (see above). In the system with isotropic exchange coupling $J > 0$ and radial magnetic field, the tangle τ tends to zero for $b/J \rightarrow 0$ due to the vanishing energy splitting $\Delta E_{0,1}$ (see Fig. 2.2). We remark that

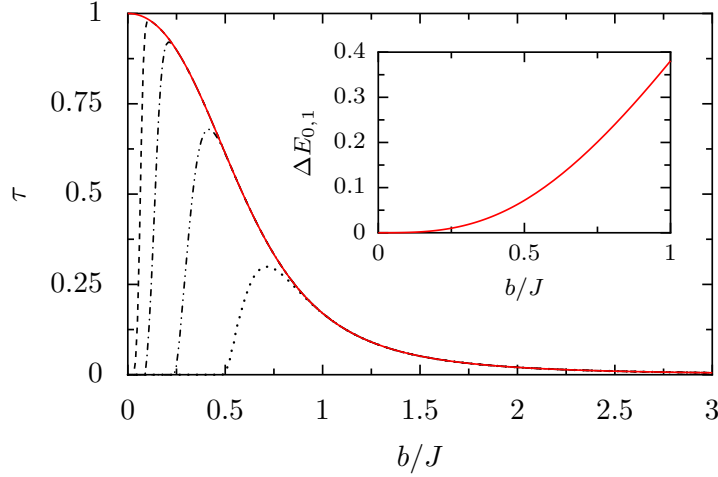


Figure 2.2: The tangle τ of the system with isotropic positive (ferromagnetic) coupling J and radial magnetic field as a function of b/J for different temperatures $T = 10^{-4}J/k_B$ (dashed line), $10^{-3}J/k_B$ (dash-dotted line), $10^{-2}J/k_B$ (dash-dot-dotted line) and $5 \times 10^{-2}J/k_B$ (dotted line). Note the twofold influence of the temperature on τ : Although higher temperatures reduce the maximally achievable entanglement, a stabilizing effect is observed as well. A maximum in the tangle is more robust against fluctuations in b at higher temperatures due to the less rapid drop-off of τ as b/J is reduced. Conversely, τ of the approximate GHZ ground state $|\text{GS}\rangle$ ($T = 0$, red line) shows a discontinuity at $b = 0$, where $\tau(\rho) = 0$. For $b > 0$, we find the simple algebraic expression $\tau_p(|\text{GS}\rangle) = (3 - 8b/J)/C + 2/\sqrt{C}$, where $C = 9 + 4b(4b/J - 3)/J$. Inset: Energy splitting $\Delta E_{0,1}$ of the ground-state doublet as a function of b/J .

this behavior is discontinuous at $T = 0$, where $\tau(\rho) \rightarrow 1$ for $b/J \rightarrow 0$, but $\tau(\rho) = 0$ at $b = 0$. With larger b/J , the ground state contributes dominantly to ρ but simultaneously deviates increasingly from a GHZ state. The entanglement in the system is therefore reduced (cf. solid line in Fig. 2.2). For a given temperature, the maximal tangle τ_{max} is therefore obtained at a finite optimal value $(b/J)_{\text{opt}}$ of the scaled magnetic field strength as a trade-off between having a highly entangled ground state and separating the latter from excited states in order to avoid the negative effects of mixing. For low temperatures $T \lesssim 10^{-2}J/k_B$, we numerically find the power laws $(b/J)_{\text{opt}} \propto (k_B T/J)^\alpha$ and $1 - \tau_{\text{max}} \propto (k_B T/J)^\beta$ with the exponents $\alpha \approx 0.30$ and $\beta \approx 0.63$. Specifically, we obtain $\tau(\rho) = 0.98$ (0.92) for $T = 10^{-4}J/k_B$ ($10^{-3}J/k_B$) and $b = 0.11J$ ($0.21J$). Apart from the effect of reducing τ_{max} , finite temperatures also possess the advantageous feature of broadening the discontinuity of τ at $T = 0$ and $b = 0$ which makes τ_{max} more stable against fluctuations of b around

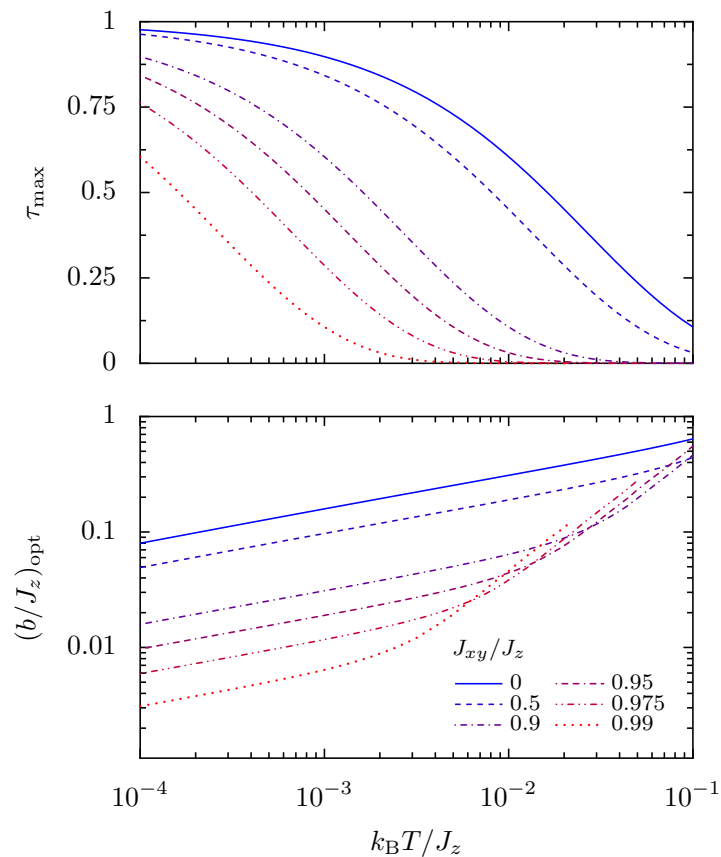


Figure 2.3: Top: Maximally achievable tangle τ_{\max} in the anisotropic system (GHZ ground state) with homogeneous in-plane magnetic field and $J_z > 0$ as a function of temperature for six anisotropy ratios J_{xy}/J_z (see legend). The curves end at $\tau(\rho) = 10^{-5}$. Bottom: The corresponding optimal values $(b/J_z)_{\text{opt}}$ of the scaled magnetic field strength b/J_z .

b_{opt} (see Fig. 2.2).

We finally come back to the general anisotropic model (2.1) with $J_{xy} \neq J_z$ subject to a homogeneous in-plane magnetic field. In Fig. 2.3 we show the maximally achievable tangle τ_{\max} (optimized with respect to b/J_z) as a function of temperature for various anisotropy ratios J_{xy}/J_z (where, as before, $J_z > 0$). Since we are interested in high values of τ_{\max} , an arbitrary but low cutoff was introduced in the calculation at $\tau(\rho) = 10^{-5}$. The lower panel of Fig. 2.3 depicts the corresponding optimal field values $(b/J_z)_{\text{opt}}$. At low temperatures T , a power-law dependence of $(b/J_z)_{\text{opt}}$ on T is observed, similar to the above isotropic case. Note that a higher amount of entanglement can be realized in systems with stronger anisotropies. E.g., for Ising coupling ($J_{xy}/J_z = 0$) we find $\tau(\rho) = 0.98$ (0.89) for $T = 10^{-4}J/k_B$ ($10^{-3}J/k_B$) and $b = 0.080J_z$ ($0.16J_z$). At $T = 10^{-4}J/k_B$ but with $J_{xy}/J_z = 0.9$, still a very good value $\tau(\rho) = 0.90$

is achieved for $b = 0.016J_z$. We remark that still higher tangles are obtained for negative (antiferromagnetic) $J_{xy} > -2J_z$. In this case, the maximal tangle as a function of T decays even more slowly than the curves displayed in the top panel of Fig. 2.3.

Possible implementations of the qubits include GaAs and InAs quantum dots, InAs nanowires or single-wall carbon nanotubes. Assuming a typical value of $|J| \sim 1$ meV [CCGL05, HKP⁺07] we obtain $\tau \approx 0.9$ at $T \approx 10$ mK and $B \approx 2$ T (assuming a g -factor of $|g| = 2$). Ferromagnetic coupling is achieved by operating the dots with more than one electron per dot.

2.7 Conclusion

We have found highly entangled states in the case of isotropic, ferromagnetic exchange coupling and an applied radial magnetic field, as well as in the case of anisotropic coupling and a homogeneous in-plane field. The mixed-state entanglement measure we have used to study the effects of finite temperatures has been evaluated numerically for the first time for general states. Due to the generic formulation of the numerical scheme implemented here, entanglement in systems with more than three parties can be investigated further.

CHAPTER 3

Algorithms and Multipartite Systems

Adapted from:
B. Röthlisberger, J. Lehmann, and D. Loss,
“Numerical evaluation of convex-roof entanglement
measures with applications to spin rings”,
Phys. Rev. A **80**, 042301 (2009).

We have successfully applied a numerical algorithm to evaluate the mixed-state tangle of three qubits in the previous chapter. Here, we generalize this idea and present two ready-to-use numerical algorithms to evaluate convex-roof extensions of arbitrary pure-state entanglement monotones. The first one is the method from chapter 2, but is discussed here in greater detail, whereas the second one is a quite different approach to the subject. Both their implementations merely leave the user with the task of calculating derivatives of the respective pure-state measure. We provide numerical tests of the algorithms and demonstrate their good convergence properties. We further employ them in order to investigate the entanglement in particular few-spins systems at finite temperature. Namely, we consider generalizations of the model studied in the previous chapter, i.e., ferromagnetic Heisenberg exchange-coupled spin- $\frac{1}{2}$ rings subject to an inhomogeneous in-plane field geometry obeying full rotational symmetry around the axis perpendicular to the ring through its center. We demonstrate that highly entangled states can be obtained in these systems at sufficiently low temperatures and by tuning the strength of a magnetic field configuration to an optimal value which is identified numerically.

3.1 Introduction

Entanglement, one of the most intriguing features of quantum mechanics [Sch35, EPR35], is undoubtedly an indispensable ingredient as a resource to any quantum computation or quantum communication scheme [NC00]. The ability to (sometimes drastically) outperform classical computations using multipartite quantum correlations has been demonstrated in various theoretical proposals which by now have become well known standard examples [DJ92, CEMM98, Gro96, Sho97]. Due to the rapid progress in the fields of quantum computation, communication, and cryptography, both on the theoretical and the experimental side, it has become a necessity to quantify and study the production, manipulation and evolution of entangled states theoretically.

However, this has turned out to be a rather difficult task, as the dimension of the state space of a quantum system grows exponentially with the number of qudits and thus permits the existence of highly non-trivial quantum correlations between parties. While bipartite entanglement is rather well understood (see, e.g., [PV07]), the study of multipartite states (with three or more qudits) is an active field of research.

Several different approaches towards the study of entanglement exist. Bell's original idea [Bel64] that certain quantum states can exceed classically strict upper bounds on expressions of correlators between measurement outcomes of different parties sharing the same state has been widely extended and improved to detect entanglement in a great variety of states. Entanglement between photons persisting over large distances has been demonstrated with the use of Bell-type inequalities (see, e.g., Ref. [UTSM⁺07] and references therein). Another more recent approach is the concept of entanglement witnesses [HHH96, Ter00]. These are observables whose expectation value is non-negative for separable states and negative for some entangled states. Thirdly, the concept of entanglement measures is focussing more on the quantification of entanglement: if state A has lower entanglement than state B , then A cannot be converted into B by means of local operations and classical communication. Remarkably, there exist interesting relations between entanglement measures and Bell inequalities [EB04] on the one hand, and entanglement witnesses [GRW07, EBaA07] on the other hand. In this work, we focus on the direct evaluation of entanglement measures.

Among the many features one can demand of such a measure, monotonicity is arguably the most important one: an entanglement measure should be non-increasing under local operations and classical communication (reflecting the fact that it is impossible to create entanglement in a separable state by these means). A measure exhibiting this property is called an entanglement monotone, with prominent examples being, e.g., the entanglement of formation [BDSW96], the tangle [CKW00], the concurrence [MKB05] or the measure by Meyer and Wallach [MW02].

While one measure captures certain features of some states especially well, other measures focus on different aspects of different states.

Often, entanglement monotones are defined only for pure states and are given as analytical expressions of the state's components in a standard basis. Unfortunately, quantifying mixed-state entanglement is more involved. This is somewhat intuitive, since the measure needs to be capable of distinguishing quantum from classical correlations. A manifestation of this difficulty is the fact that the problem of determining whether a given density matrix is separable or not is apparently very hard and has no known general solution for an arbitrary number of subsystems with arbitrary dimensions. The ability to study mixed-state entanglement is, however, highly desirable since mixed-states appear naturally due to various coupling mechanisms of the system under examination to its environment. There exists a standard way to construct a mixed-state entanglement monotone from a pure-state monotone, the so-called convex-roof construction [Uhl00], but the evaluation of functions obtained in this way requires the solution of a rather involved constrained optimization problem (see Sec. 3.2).

We present in this chapter two algorithms targeted at solving this optimization problem numerically for any given convex-roof entanglement measure. In principle, these algorithms can also be applied to any optimization problem subjected to the same kind of constraints. The first algorithm is an extension of a procedure originally used to calculate the entanglement of formation [AVDM01]. It is a conjugate gradient method exploiting the geometric structure of the nonlinear search space emerging from the optimization constraint. The second algorithm is based on a real parameterization of the search space, which allows one to carry out the optimization problem in the more familiar Euclidean space using standard techniques.

In the second part of this chapter, we use these algorithms in order to study the entanglement properties of a certain type of spin rings. These systems form a generalization to N qubits of our study in the previous chapter, where we had only considered the case $N = 3$. In the presence of an isotropic and ferromagnetic Heisenberg interaction and local in-plane magnetic fields obeying a radial symmetry, it can be argued (see sections 2.3 and 3.4) that the ground state becomes a local unitary equivalent of an almost perfect N -partite Greenberger-Horne-Zeilinger (GHZ) state [GHZ89]

$$|\text{GHZ}_N^\pm\rangle = (|\uparrow\uparrow \dots \uparrow\rangle \pm |\downarrow\downarrow \dots \downarrow\rangle) / \sqrt{2}. \quad (3.1)$$

Such a system could hence be used for the production of highly entangled multipartite states merely by cooling it down to low temperatures. One finds, however, that the energy splitting between the ground and first excited state vanishes in the same limit as the N -partite approximate

GHZ states become perfect, namely for the magnetic field strength going to zero. Therefore, in order to quantitatively identify the magnetic field strengths yielding maximal entanglement at finite temperature, one has to study the system in terms of a suitable mixed-state entanglement measure.

The outline of this chapter is as follows: In Sec. 3.2 we review how the evaluation of a convex-roof entanglement measure is related to a constrained optimization problem. We then develop and describe the numerical algorithms capable of tackling this problem in Sec. 3.3. We also present some benchmark tests, comparing our methods to another known algorithm. In Sec. 3.4, we describe the spin rings mentioned earlier and study their entanglement properties in terms of a convex-roof entanglement measure evaluated using our algorithms. We conclude the work presented in this chapter in Sec. 3.5.

3.2 Convex-roof entanglement measures as constrained optimization problems

Given a pure-state entanglement monotone m , the most reasonable properties one can demand of a generalization of m to mixed states are that this generalization is itself an entanglement monotone, and that it properly reduces to m for pure states. A standard procedure which achieves this is the so-called convex-roof construction [Uhl00, MCKB05]. Given a mixed state ρ acting on a Hilbert space \mathcal{H} of finite dimension d , it is defined as

$$M(\rho) = \inf_{\{p_i, |\psi_i\rangle\} \in \mathfrak{D}(\rho)} \sum_i p_i m(|\psi_i\rangle), \quad (3.2)$$

where

$$\mathfrak{D}(\rho) = \left\{ \{p_i, |\psi_i\rangle\}_{i=1}^s, s \geq \text{rank } \rho \mid \{|\psi_i\rangle\}_{i=1}^s \subset \mathcal{H}, \right. \\ \left. p_i \geq 0, \sum_{i=1}^s p_i = 1, \rho = \sum_{i=1}^s p_i |\psi_i\rangle\langle\psi_i| \right\} \quad (3.3)$$

is the set of all pure-state decompositions of ρ . Note that the pure states $|\psi_i\rangle$ are understood to be normalized. The numerical value of $M(\rho)$ is hence defined as an optimization problem over the set $\mathfrak{D}(\rho)$.

In order to apply numerical algorithms to this problem, $\mathfrak{D}(\rho)$ must be accessible in a parametric way. This parameterization is well-known and is often referred to as the Schrödinger-HJW theorem [HJW93, Kir05], which we briefly outline here for the sake of completeness.

Let $St(k, r)$ denote the set of all $k \times r$ matrices $U \in \mathbb{C}^{k \times r}$ with the property $U^\dagger U = 1_{r \times r}$, i.e., matrices with orthonormal column vectors

(hence we have $k \geq r$). The first part of the Schrödinger-HJW theorem states that every $U \in St(k, r)$ yields a pure-state decomposition $\{p_i, |\psi_i\rangle\}_{i=1}^k \in \mathfrak{D}(\rho)$ of the density matrix ρ by the following construction. Let $\lambda_i, |\chi_i\rangle, i = 1, \dots, r = \text{rank } \rho$ denote the eigenvalues and corresponding normalized eigenvectors of ρ , i.e.,

$$\rho = \sum_{i=1}^r \lambda_i |\chi_i\rangle\langle\chi_i|. \quad (3.4)$$

Note that we have $\lambda_i > 0$ since ρ is a density matrix and as such a positive semi-definite operator. Given a matrix $U \in St(k, r)$, define the auxiliary states

$$|\tilde{\psi}_i\rangle = \sum_{j=1}^r U_{ij} \sqrt{\lambda_j} |\chi_j\rangle, \quad i = 1, \dots, k. \quad (3.5)$$

It is then readily checked that

$$p_i = \langle\tilde{\psi}_i|\tilde{\psi}_i\rangle, \quad (3.6)$$

$$|\psi_i\rangle = (1/\sqrt{p_i})|\tilde{\psi}_i\rangle \quad (3.7)$$

is indeed a valid decomposition of ρ into a convex sum of k projectors.

The second part of the theorem states that for any given pure-state decomposition $\{p_i, |\psi_i\rangle\}_{i=1}^k$ of ρ , there exists a $U \in St(k, r)$ realizing the decomposition by the above construction. This guarantees that by searching over the set $St(k, r)$ and obtaining the decompositions according to the Schrödinger-HJW theorem, we do not ‘miss out’ on any part of the subset of $\mathfrak{D}(\rho)$ with a fixed number of states k . The parameterization is thus complete, i.e., searching the infimum over $St(k, r)$ is equivalent to searching over all decompositions with fixed so-called cardinality k . This allows us to reformulate the optimization problem Eq. (3.2) as

$$M(\rho) = \min_{k \geq r} \inf_{U \in St(k, r)} h(U), \quad (3.8)$$

where $h(U)$ is the sum on the right-hand side of Eq. (3.2) obtained via the matrix U from ρ , i.e.,

$$h(U) = \sum_{i=1}^k p_i(U) m(|\psi_i(U)\rangle). \quad (3.9)$$

Note that we have dropped the ρ -dependence in the above expressions, since ρ is fixed within a particular calculation and only the dependence of h on U is of relevance in the following.

It is clear that in a numerical calculation only a finite number of different values for k can be investigated. However, it is also intuitive to expect that for some large enough value of k , increasing the latter even

further has only marginal effects. In fact, we have observed numerically that already $k = \text{rank } \rho + 4$ yields very accurate results in all tests we have performed (also in the ones presented in Sec. 3.3), and we have used this choice throughout all numerical calculations within this work. Note that for a fixed value of k , also all other decompositions with cardinality smaller than k are considered as well, since the probabilities p_i in the elements of $\mathfrak{D}(\rho)$ are allowed to go to zero (with the convention that the corresponding states $|\psi_i\rangle$ are then discarded).

Since the algorithms presented in the next section will both be gradient-based, the derivatives of Eq. (3.9) with respect to the real and imaginary parts of U evaluated at U will be required at some point. We state them here for the convenience of the reader. They are given by

$$\begin{aligned} \frac{\partial h}{\partial \text{Re } U_{kl}} &= 2\lambda_l \text{Re}(U_{kl})m(|\psi_k(U)\rangle) \\ &+ \sum_{i=1}^d \left[\text{Re } \phi_{R,kl}^{(i)} \frac{\partial m}{\partial \text{Re } \psi^{(i)}} \Big|_{|\psi_k(U)\rangle} + \text{Im } \phi_{R,kl}^{(i)} \frac{\partial m}{\partial \text{Im } \psi^{(i)}} \Big|_{|\psi_k(U)\rangle} \right], \end{aligned} \quad (3.10)$$

$$\begin{aligned} \frac{\partial h}{\partial \text{Im } U_{kl}} &= 2\lambda_l \text{Im}(U_{kl})m(|\psi_k(U)\rangle) \\ &+ \sum_{i=1}^d \left[\text{Re } \phi_{I,kl}^{(i)} \frac{\partial m}{\partial \text{Re } \psi^{(i)}} \Big|_{|\psi_k(U)\rangle} + \text{Im } \phi_{I,kl}^{(i)} \frac{\partial m}{\partial \text{Im } \psi^{(i)}} \Big|_{|\psi_k(U)\rangle} \right], \end{aligned} \quad (3.11)$$

where

$$|\phi_{R,kl}(U)\rangle = \left[\sqrt{p_k(U)\lambda_l}|\chi_l\rangle - \lambda_l \text{Re}(U_{kl})|\psi_k(U)\rangle \right], \quad (3.12)$$

$$|\phi_{I,kl}(U)\rangle = \left[\text{i}\sqrt{p_k(U)\lambda_l}|\chi_l\rangle - \lambda_l \text{Im}(U_{kl})|\psi_k(U)\rangle \right], \quad (3.13)$$

and superscripts such as in $\psi^{(i)}$ denote the i th component of the state $|\psi\rangle$ in an arbitrary but fixed basis.

As a last remark, we would like to point out that the constraint set $St(k, r)$ is, in fact, a closed embedded submanifold of $\mathbb{C}^{k \times r}$, called the complex Stiefel manifold [AMS08]. The geometric structure emerging thereof is exploited in one of the two algorithms following shortly. The dimension of the Stiefel manifold is $\dim St(k, r) = 2kr - r^2$ [AMS08]. Since we have $k \geq r$, we can set $k = r + n$, $n = 0, 1, \dots$. The number of free parameters N in the optimization is thus $N = r^2 + 2nr$. Hence, N grows linearly with n , but quadratically with r . The numerical evaluation in larger systems will thus be restricted to low-rank density matrices. The flexibility of choosing n is however less restricted. As mentioned above, $n = 4$ already yields satisfying results.

3.3 Numerical algorithms

The study of optimization problems on matrix manifolds is a rather new and still active field of research (see [EAS98, AMS08] and references therein). Only recently, two ready-to-use algorithms for minimization over the complex Stiefel manifold have been presented [Man02]. To our knowledge, these are the only general purpose algorithms applicable to generic target functions over $St(k, r)$ found in the literature. One is a steepest descent-type method, the other one is of Newton-type. We will compare the performance of the modified steepest descent algorithm, as it is referred to in the original work, with the methods presented in this section. We have found that our algorithms generally show better convergence properties in the cases we have examined.

We will, however, not make use of the modified Newton algorithm for the following reasons. The second derivatives (as required by any Newton-type algorithm) of the function $h(U)$ [Eq. (3.9)] are in general quite involved and their number grows quadratically with the size of U . Hence, they are very expensive to evaluate, even if one resorts to numerical finite differences. Moreover, the good convergence properties of Newton-type methods may only be expected in the very proximity of a local minimum. One therefore first typically employs gradient-based techniques to approach a minimum sufficiently enough. However, what ‘sufficiently enough’ means in a particular case is often not known beforehand. We will later make use of a quasi-Newton algorithm, which approaches local minima satisfyingly and shows strong convergence similar to Newton methods automatically when being close enough to a minimum.

Generalized Conjugate-Gradient Method

In Ref. [AVDM01] a conjugate-gradient algorithm on the unitary group $U(k) = St(k, k)$ was presented. The goal there was to calculate the entanglement of formation also for systems with dimensions different from 2×2 [Woo98]. Here, we extend this result by noting that the method is applicable to any optimization problem on $St(k, k)$, particularly to the evaluation of entanglement measures other than the entanglement of formation, and we calculate the required general expression of the gradient of $h(U)$.

Optimizing over $St(k, k)$ instead of $St(k, r)$ comes at the cost of over-parameterizing the search space. When using this algorithm to calculate convex-roof entanglement measures, we simply took into account only the first r columns of the matrix obtained at every iteration. This is certainly an aspect one could improve upon in future research.

The algorithm presented here is a conjugate gradient-type method, meaning that instead of simply going downhill, i.e., in the direction of

steepest descent, previous search directions are taken into account at the current iteration step. Once the search direction X_i at iteration step i , a skew-Hermitian $k \times k$ matrix, is known, a line search along the geodesic $U_i \exp(tX_i)$ is performed, where U_i is the current iteration point. In particular, one iteration step of the algorithm may be described as follows [AVDM01]:

1. Perform a line minimization, i.e., set

$$t_{i+1} \leftarrow \arg \min_t h(U_i \exp(tX_i)) \quad (3.14)$$

and set

$$U_{i+1} \leftarrow U_i \exp(t_{i+1}X_i). \quad (3.15)$$

2. Compute the new gradient G_{i+1} at U_{i+1} and set

$$T \leftarrow \exp(t_{i+1}X_i/2)G_i \exp(-t_{i+1}X_i/2). \quad (3.16)$$

T is the gradient G_i parallel-transported to the new point U_{i+1} .

3. Calculate the modified Polak-Ribière parameter

$$\gamma \leftarrow \frac{\langle G_{i+1} - T, G_{i+1} \rangle}{\langle G_i, G_i \rangle}, \quad (3.17)$$

where $\langle X, Y \rangle = \text{Tr } XY^\dagger$.

4. Set the new search direction to

$$X_{i+1} \leftarrow -G_{i+1} + \gamma X_i. \quad (3.18)$$

5. $i \leftarrow i + 1$.

6. Repeat from step 1 until convergence.

The starting point U_0 can be chosen arbitrarily, and the initial search direction is set to $X_0 = -G_0$. In order to find a good approximation to the global minimum, one should restart the procedure several times using random initial conditions. For the line search in step 1, we utilized the derivative-free algorithm `linmin` described in Ref. [PTVF92].

In the following, we calculate the general expression for the gradient G of the function h , evaluated at the point U (we drop iteration indices for simplicity). The gradient G is defined in terms of the directional derivative of h , namely as

$$\left. \frac{dh(U^{(\varepsilon)}(X))}{d\varepsilon} \right|_{\varepsilon=0} = \langle G, X \rangle, \quad (3.19)$$

where $U^{(\varepsilon)}(X) = V \exp(\varepsilon X)$ is a geodesic on $St(k, k)$ in direction X (skew-Hermitian matrix) and passing through V . The inner product is defined as in step 3 of the algorithm. We will eventually read off the gradient G from its definition in Eq. (3.19).

Treating $h(U)$ as a function of the real and imaginary matrix elements of U , $\text{Re } U_{ik}$ and $\text{Im } U_{ik}$, respectively, we have

$$\begin{aligned} \left. \frac{dh(U^{(\varepsilon)}(X))}{d\varepsilon} \right|_{\varepsilon=0} &= \sum_{ik} \left(\left. \frac{\partial h}{\partial \text{Re } U_{ik}} \right|_V \left. \frac{\partial \text{Re } U_{ik}^{(\varepsilon)}}{\partial \varepsilon} \right|_{\varepsilon=0} \right. \\ &\quad \left. + \left. \frac{\partial h}{\partial \text{Im } U_{ik}} \right|_V \left. \frac{\partial \text{Im } U_{ik}^{(\varepsilon)}}{\partial \varepsilon} \right|_{\varepsilon=0} \right). \end{aligned} \quad (3.20)$$

The partial derivatives of h with respect to $\text{Re } U_{ik}$ and $\text{Im } U_{ik}$ have already been stated in Eqs. (3.10, 3.11). Inserting the derivatives of $U_{ik}^{(\varepsilon)}$ into Eq. (3.20) and sorting all terms with respect to $\text{Re } X$ and $\text{Im } X$, we obtain

$$\left. \frac{dh(U^{(\varepsilon)}(X))}{d\varepsilon} \right|_{\varepsilon=0} = \sum_{kl} (A_{kl} \text{Re } X_{kl} + S_{kl} \text{Im } X_{kl}), \quad (3.21)$$

where

$$A_{kl} = \sum_i \left(\left. \frac{\partial h}{\partial \text{Re } U_{il}} \right|_V \text{Re } V_{ik} + \left. \frac{\partial h}{\partial \text{Im } U_{il}} \right|_V \text{Im } V_{ik} \right), \quad (3.22)$$

$$S_{kl} = \sum_i \left(\left. \frac{\partial h}{\partial \text{Im } U_{il}} \right|_V \text{Re } V_{ik} - \left. \frac{\partial h}{\partial \text{Re } U_{il}} \right|_V \text{Im } V_{ik} \right). \quad (3.23)$$

Taking into account the symmetry conditions on X by using the relations $\text{Re } X = (X - X^T)/2$ and $\text{Im } X = -i(X + X^T)/2$ we further obtain

$$\left. \frac{dh(U_\varepsilon(X))}{d\varepsilon} \right|_{\varepsilon=0} = \frac{1}{2} \sum_{kl} ((A_{kl} - A_{lk}) - i(S_{kl} + S_{lk})) X_{kl}. \quad (3.24)$$

By comparing this to the right-hand side of Eq. (3.19), i.e.,

$$\langle G, X \rangle = \text{Tr } GX^\dagger = - \sum_{kl} G_{lk} X_{kl}, \quad (3.25)$$

we finally obtain the desired expression for the matrix elements of the gradient G ,

$$G_{kl} = (A_{kl} - A_{lk})/2 + i(S_{kl} + S_{lk})/2. \quad (3.26)$$

One readily sees that G is skew-Hermitian, as required.

By this, we have completed the description of the conjugate gradient algorithm capable of evaluating any convex-roof entanglement measure presented in the form of Eq. (3.8).

Parameterization with Euler-Hurwitz angles

Here we present an alternative approach to optimization problems over the Stiefel manifold $St(k, r)$. We will obtain a parameterization of $St(k, r)$ in terms of a set of real numbers which we will call Euler-Hurwitz angles, therefore unconstraining the optimization problem and mapping it to Euclidean space, where optimization problems have been investigated for much longer. We will therefore be able to employ a standard algorithm to tackle the transformed problem Eq. (3.8) [NW99].

The idea of parameterizing $St(k, r)$ is somewhat motivated by a theorem known in classical mechanics, where it is stated that any rotation in three-dimensional Euclidean space can be written as a sequence of three elementary rotations described by three angles, the Euler angles. In other words, any orthogonal 3×3 matrix is parameterized by three real numbers. It was already Euler himself who generalized this idea to arbitrary $k \times k$ orthogonal matrices [Eul87], and Hurwitz [Hur33] extended the parameterization to unitary matrices. We remark that ideas in a similar fashion to the ones promoted here have been used to calculate an entanglement measure for Werner states [THLD02] but were not discussed in greater detail.

We now derive the parameterization of $St(k, r)$. Let $A \in St(k, r)$. The basic idea is to generate zeroes in A and bring it to upper triangular form by applying so-called (complex) Givens rotations $G_s(\vartheta, \varphi)$ [GVL96] to A from the left. The $k \times k$ matrices $G_s(\vartheta, \varphi)$, $s = 1, \dots, k - 1$, are defined as

$$G_s^{i,j}(\vartheta, \varphi) = \begin{cases} e^{i\varphi} \cos \vartheta, & \text{if } i = j = s, \\ e^{-i\varphi} \sin \vartheta, & \text{if } i = s, j = s + 1, \\ -e^{i\varphi} \sin \vartheta, & \text{if } i = s + 1, j = s, \\ e^{-i\varphi} \cos \vartheta, & \text{if } i = s + 1, j = s + 1, \\ \delta_{ij}, & \text{otherwise.} \end{cases} \quad (3.27)$$

Multiplying A from the left with $G_s(\vartheta, \varphi)$, i.e., $\tilde{A} = G_s(\vartheta, \varphi)A$, has the action

$$\tilde{A}_{i,\cdot} = \begin{cases} e^{i\varphi} \cos \vartheta A_{s,\cdot} + e^{-i\varphi} \sin \vartheta A_{s+1,\cdot}, & \text{if } i = s, \\ -e^{i\varphi} \sin \vartheta A_{s,\cdot} + e^{-i\varphi} \cos \vartheta A_{s+1,\cdot}, & \text{if } i = s + 1, \\ A_{i,\cdot}, & \text{otherwise,} \end{cases} \quad (3.28)$$

where $A_{i,\cdot}$ denotes the i th row of A .

Let us write the matrix elements $A_{s,j}$ and $A_{s+1,j}$, with j arbitrary but fixed, in polar form, i.e., $A_{s,j} = x e^{i\phi_x}$ and $A_{s+1,j} = y e^{i\phi_y}$, with $x, y \geq 0$. We stick to the convention that the phases ϕ_x and ϕ_y be in the interval $]-\pi, \pi]$ in order to make this representation unique. It is now easy to see that by

choosing

$$\varphi = (\phi_y - \phi_x)/2, \quad (3.29)$$

$$\vartheta = \arctan \frac{y}{x}, \quad (3.30)$$

we obtain

$$(G_s(\vartheta, \varphi)A)_{s+1,j} = 0, \quad (3.31)$$

while all the other entries in the s th and $(s + 1)$ th row have changed according to Eqs. (3.28). In the case $x = 0$, we set $\vartheta = \pi/2$ and $\varphi = 0$. In the case $y = 0$, we have $\vartheta = 0$, and we choose to set $\varphi = 0$ as well. The angles ϑ and φ are thus restricted to the intervals $\vartheta \in [0, \frac{\pi}{2}]$ and $\varphi \in]-\pi, \pi[$.

By successively applying Givens rotations with appropriately chosen angles according to Eqs. (3.29) and (3.30), we may now generate zeroes in A column by column, from left to right, bottom to top. In greater detail, we first erase the whole first column, except for the top entry which will generally remain non-zero. Continuing at the bottom of the second column, we may generate zeros up to (and including) the third entry from the top of the column. If we tried to make the second entry zero, we would in general generate a non-zero entry in the second row of the first column according to the transformation Eq. (3.28). It is convenient to label the angles calculated during this process by two indices, and to use the abbreviation $G_s(i, j) = G_s(\vartheta_{ij}, \varphi_{ij})$. Eventually, we obtain a matrix \tilde{R} given by

$$\tilde{R} = \tilde{Q}^{-1}A = \prod_{i=0}^{r-1} \left[\prod_{j=r-i}^{k-1} G_j(r-i, k-j) \right] A. \quad (3.32)$$

The inner of the two products generates zeros in column $r - i$ from the bottom up to (and including) row number $r - i + 1$. The upper block of \tilde{R} consisting of the first r rows is of upper triangular form, while the lower block is zero. As a product of unitary Givens rotations, \tilde{Q}^{-1} is itself unitary and in particular invertible. Hence, \tilde{Q} always exists and is unitary. We may therefore write

$$A = \tilde{Q}\tilde{R} = QR, \quad (3.33)$$

where $Q \in St(k, r)$ consists of the first r columns of \tilde{Q} and R is the upper $r \times r$ block of \tilde{R} . Since we assumed that $A \in St(k, r)$, we have

$$1_{r \times r} = A^\dagger A = (QR)^\dagger QR = R^\dagger Q^\dagger QR = R^\dagger R, \quad (3.34)$$

and hence, R is unitary. It is straightforward to see that a unitary upper triangular matrix can only be of the form

$$R_{ij} = \delta_{ij} e^{ix_i}, \quad (3.35)$$

i.e., a diagonal matrix with only phases on the diagonal. Again, we may choose $\chi_i \in]-\pi, \pi]$.

We have thus achieved a *unique* parameterization of an arbitrary matrix $A \in St(k, r)$ by a tuple of Euler-Hurwitz angles $(\vartheta, \varphi, \chi) \in \mathfrak{S}$, where

$$\mathfrak{S} = [0, \frac{\pi}{2}]^{r(k-\frac{r+1}{2})} \times]-\pi, \pi]^{r(k-\frac{r+1}{2})} \times]-\pi, \pi]^r. \quad (3.36)$$

As required, we find that the number of free parameters in this representation is equal to the dimension of the Stiefel manifold, i.e., $\dim St(k, r) = 2kr - r^2$. It is clear that the procedure described above is fully invertible. Hence, we have obtained a one-to-one mapping $F : \mathfrak{S} \rightarrow St(k, r)$. In detail, this mapping, for a vector $(\vartheta, \varphi, \chi) \in \mathfrak{S}$, is carried out by filling an otherwise empty $k \times r$ matrix B with the entries $B_{ii} = e^{i\chi_i}$, $i = 1, \dots, r$. Then, we apply inverse Givens rotations (specified by the Euler-Hurwitz angles ϑ and φ) from the left to B , in inverse order with respect to Eq. (3.32).

In conclusion, we have transformed the optimization problem Eq. (3.8) into the new problem

$$M(\rho) = \min_{k \geq r} \inf_{s \in \mathfrak{S}} h(F(s)). \quad (3.37)$$

Due to the periodic dependence of $F(s)$ on the angles s , it is practical to expand the search space from \mathfrak{S} to the whole Euclidean space, making Eq. (3.37) a completely unconstrained optimization problem (at the cost of over-parameterizing the search space [1]). This problem can then be solved using standard numerical techniques. In all our calculations, we have used a quasi-Newton algorithm [NW99] together with the line search `linmin` mentioned earlier. This method requires first derivatives of the target function with respect to the angles. The derivatives with respect to F have already been stated in Eqs. (3.10, 3.11), and the derivatives of F with respect to the angles are obtained straightforwardly since each angle appears only once in the product representation presented above. In order to find a good approximation to the global minimum, one should restart with random initial conditions several times and take the over-all minimum.

Test Cases

Here, we briefly present some performance results of the two algorithms presented above. We have applied them to the evaluation of two different convex-roof entanglement measures for which the numerical data

¹Allowing the iteration points to move outside of \mathfrak{S} may result in large absolute values of the angles, possibly leading to reduced precision in the output. Such effects can be prevented by projecting the current iteration point back to \mathfrak{S} a few times in the first couple of iterations.

can be verified by analytically known results. Although our algorithms show comparatively good performance in these cases, we would like to stress that the efficiency of a certain method depends strongly on the type of problem present, and may even be related to the particular instance of the problem (see the GHZ/W example below). We have for instance also studied certain matrix approximation problems, in some of which the parameterized quasi-Newton method converged very poorly, whereas the modified steepest descent and the generalized conjugate gradient method were equally strong and very efficient. One thus cannot generically claim one algorithm to be better than the other. It is just beneficial to have several different techniques at hand, out of which one can choose the best-performing one when applied to a particular given problem.

Entanglement of formation of random 2×2 states

The entanglement of formation [BDSW96] is a popular entanglement measure for bipartite mixed states. It is defined as the convex roof of the entropy of entanglement [BBPS96], which is, for a state $|\psi\rangle$, the von-Neumann entropy $S(\rho) = -\text{Tr} \rho \log_2 \rho$ of the reduced density matrix $\rho = \text{Tr}_B |\psi\rangle\langle\psi|$, Tr_B denoting the partial trace over the second subsystem.

Figure 3.1 shows the convergence behavior of the algorithms applied to ten random full-rank two-qubit density matrices. Displayed is the error at each step of the iteration between the respective iteration value and the true result. The latter is known analytically from Ref. [Woo98].

Compared to the algorithms described here, the modified steepest descent algorithm due to Ref. [Man02] (top panel) performs rather poorly. We are aware of the fact that we are comparing here a steepest descent algorithm with two superlinear algorithms. However, apart from presenting convergence properties, we would like to point out that the modified steepest descent algorithm often converges to imprecise solutions, i.e., it gets stuck in undesirable local minima. Rather than on the starting point, this phenomenon seems to depend more on the actual density matrix itself.

The conjugate gradient algorithm due to Ref. [AVDM01] (middle panel) also shows some dependence on the form of the density matrix, but always reaches satisfactory accuracy. The results for the parameterized quasi-Newton method (bottom panel) do not, at first glance, show the typical fast drop to the solution when close to a good local minimum. This is due to the effect that changing the starting point seems to have more influence on the number of required iterations in the case of the quasi-Newton method (see insets in Fig. 3.1). When considering single (non-averaged) runs of the algorithm, the fast convergence to the minimum becomes visible. In conclusion, the conjugate gradient and the parameterized quasi-Newton methods perform best in this case, the latter

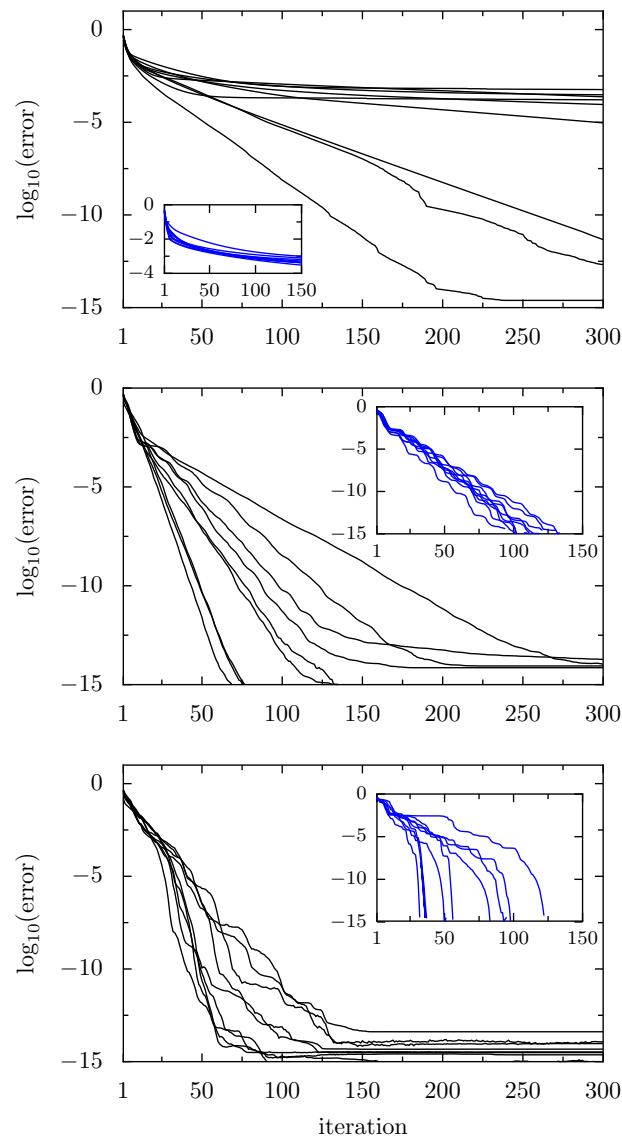


Figure 3.1: Convergence plots of the algorithms used to evaluate the entanglement of formation on ten random full-rank two-qubit states (each plot was done using the same ten states) showing the difference between the numerical data and the analytical result as a function of the iteration number. Top: The modified steepest descent algorithm from Ref. [Man02]; Middle: The generalized conjugate gradient method from Sec. 3.3; Bottom: Quasi-Newton on the parameterized search space, Sec. 3.3. Each curve in the main plot is averaged over ten randomly chosen initial points. The typical behavior of the algorithms for a single fixed density matrix, but with varying initial points of the iteration, is displayed in the insets.

even slightly better than the former.

Tangle of GHZ/W mixtures

The second test case we present here is concerned with the evaluation of the tangle of the rank-2 mixed states

$$\rho(\eta) = \eta|\text{GHZ}_3^+\rangle\langle\text{GHZ}_3^+| + (1 - \eta)|\text{W}\rangle\langle\text{W}|, \quad (3.38)$$

where $|\text{GHZ}_3^+\rangle$ has been defined in Eq. (3.1),

$$|\text{W}\rangle = \frac{1}{\sqrt{3}}(|\uparrow\downarrow\downarrow\rangle + |\downarrow\uparrow\downarrow\rangle + |\downarrow\downarrow\uparrow\rangle) \quad (3.39)$$

is the three-qubit W state [DVC00], and $0 \leq \eta \leq 1$. The tangle τ_p [CKW00] is an entanglement measure for pure states of three qubits and is known to be an entanglement monotone [DVC00]. It can hence be generalized to mixed states by the convex roof construction (3.2). We will denote the mixed-state tangle by τ , in contrast to the pure-state version τ_p . The definition of τ_p reads

$$\tau_p(|\psi\rangle) = 4 |d_1 - 2d_2 + 4d_3|, \quad (3.40)$$

where

$$d_1 = \psi_1^2\psi_8^2 + \psi_2^2\psi_7^2 + \psi_3^2\psi_6^2 + \psi_5^2\psi_4^2, \quad (3.41)$$

$$d_2 = \psi_1\psi_8\psi_4\psi_5 + \psi_1\psi_8\psi_6\psi_3 + \psi_1\psi_8\psi_7\psi_2 + \psi_4\psi_5\psi_6\psi_3 \\ + \psi_4\psi_5\psi_7\psi_2 + \psi_6\psi_3\psi_7\psi_2, \quad (3.42)$$

$$d_3 = \psi_1\psi_7\psi_6\psi_4 + \psi_8\psi_2\psi_3\psi_5, \quad (3.43)$$

and $\psi_1, \psi_2, \dots, \psi_8$ denote the components of the state $|\psi\rangle$ represented in an arbitrary product basis. In this form, the derivatives of τ_p with respect to the real and imaginary parts of the components of $|\psi\rangle$, as required by the gradient Eqs. (3.10, 3.11), can be read off most easily. The tangle takes values between 0 and 1 and is maximal for GHZ states. The tangle of the states $\rho(\eta)$ has been studied in Ref. [LOSU06], where analytical expressions as a function of η were presented [2]. Particularly, it was found that the tangle vanishes for all $0 \leq \eta \leq \eta_0$, where $\eta_0 = \frac{4\sqrt[3]{2}}{3+4\sqrt[3]{2}} \approx 0.6269$, and then continuously increases to unity at $\eta = 1$.

In Figure 3.2 we plot the error between the numerically obtained and analytically calculated values of $\tau(\rho(\eta))$ as a function of the iteration

²The entanglement of $\rho(\eta)$ (and other states) has also been studied in Ref. [BC08] in terms of the ‘global robustness’ [VT99]. The search over all separable (pure and mixed) states appearing in the evaluation of this measure could in principle also be accomplished with the parameterized quasi-Newton method (similar in spirit to Sec. 3.3).

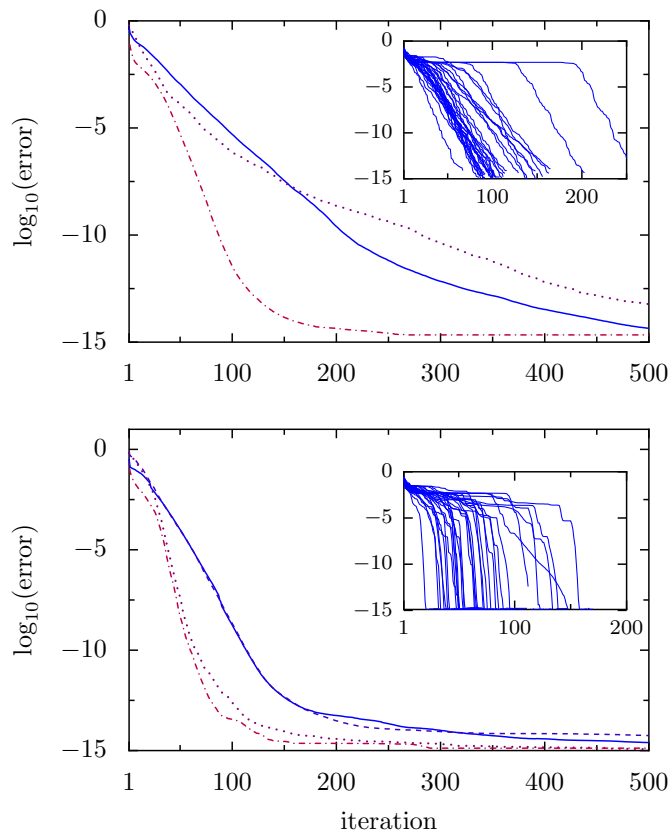


Figure 3.2: Convergence of the generalized conjugate gradient (top) and the parameterized quasi-Newton (bottom) algorithms for the tangle of GHZ/W states Eq. (3.38). The curves for the values $\eta = \frac{1}{5}\eta_0$ (solid line), $\eta = (1 - 10^{-4})\eta_0$ (dashed line), $\eta = (1 + 10^{-4})\eta_0$ (dotted line), and $\eta = \frac{7}{5}\eta_0$ (dashed-dotted line) have each been obtained by averaging 100 successful runs starting with random initial points. The typical behavior of single runs is shown in the insets, where the 100 successful tries that yield one curve in the main plots are displayed.

number for four particular values of η (see caption of the figure). Only the results of the generalized conjugate gradient (top panel) and the parameterized quasi-Newton (bottom panel) method are shown. The modified steepest descent algorithm from Ref. [Man02] did not succeed to converge to a reasonable local minimum for the lowest three values of η considered. In these cases, we empirically find the success rate, which we define as the relative number of final errors smaller than 10^{-6} , to be $\lesssim 0.1\%$. For the largest value of η examined, the algorithm showed typical linear convergence behavior and arrived at a precision around $10^{-12} - 10^{-6}$ after 1000 iterations with a rather high success rate of about 60%. Similarly, the generalized conjugate gradient algorithm failed to obtain reasonable results for the value of η slightly below the threshold value p_0 in most at-

tempts, and we find a success rate of $\lesssim 0.2\%$. The success probability for the other three values of η are between 12% and 95%, whereas they are between 25% and 80% for the parameterized quasi-Newton algorithm. One can see, with the help of looking more detailed into the behavior of single runs (see insets), that the averaged convergence plots are slightly flattened out due to some rather rare occurrences of slow convergence. Still, one can observe that the parameterized quasi-Newton method converges faster to good local minima.

Local unitary equivalence

We would like to remark here that the parameterized quasi-Newton method is also capable of determining whether two arbitrary mixed states are equivalent up to local unitary transformations. While this problem has an operational solution in some special cases (see, e.g., Ref. [FJ05] and references therein), there is no generally applicable operational criterion known capable of making this decision. Using the parameterization developed in Sec. 3.3, one can express each local unitary transformation U_i in the matrix $U = U_1 \otimes U_2 \otimes \dots \otimes U_n$ by its Euler-Hurwitz angles and optimize over the whole set of all angles simultaneously. Furthermore, one can study in this way how ‘close’ two mixed state are with respect to local unitary equivalence. Note that such kind of analyses are not possible with the modified steepest descent or the generalized conjugate gradient methods, since, as there is no parameterization, one can optimize over only one unitary matrix at a time.

3.4 Physical application

In this section, we use the algorithms developed and described above to evaluate a multipartite mixed-state entanglement measure of a concrete physical system.

Exchange-coupled spin rings with inhomogeneous magnetic field geometry

In the following, we consider the Hamiltonian

$$H = -J \sum_{i=1}^N \mathbf{S}_i \cdot \mathbf{S}_{i+1} + b \sum_{i=1}^N (S_i^x \cos \alpha_i + S_i^y \sin \alpha_i), \quad (3.44)$$

where $\mathbf{S}_i = (S_i^x, S_i^y, S_i^z)$, $S_i^k = \sigma^k/2$ with σ^k being the standard Pauli matrices acting on the i th spin, $\mathbf{S}_{N+1} \equiv \mathbf{S}_1$ and the angles $\alpha_k = 2\pi(k-1)/N$, $k = 1, \dots, N$. Equation (3.44) describes a closed ring of $N \geq 2$ equidistant exchange-coupled spin qubits with local in-plane magnetic fields

$\mathbf{b}_i \equiv (b \cos \alpha_i, b \sin \alpha_i, 0)^T$ which are chosen such that the system is invariant under rotations by multiples of $2\pi/N$ about the center of the ring. The exchange coupling J is throughout assumed to be ferromagnetic (i.e., $J > 0$). The fields in Eq. (3.44) are chosen to point radially outwards, but the following discussion and results also hold for any other local in-plane field configuration possessing the same rotational symmetry, since all these systems are local unitary equivalents. The system is depicted schematically in Fig. 2.1 (a) for three spins.

In fact, we are considering here a generalization of one of the $N = 3$ cases studied in chapter 2. There, the particular field configuration resulted from semiclassical considerations with the goal of obtaining a state which is close to a GHZ state [see Eq. (3.1)] as the ground state of the system. In that case, entanglement can be created by merely cooling the system to low enough temperatures. In principle, the argumentation for the occurrence of a GHZ ground state presented in chapter 2 can be extended to a number of qubits $N > 3$. However, it can be expected that for $N \rightarrow \infty$, the lowest-lying multiplet becomes a continuous spectrum. Hence, the question arises up to which numbers of spins N this setup still allows generating GHZ-type entanglement. Before further investigating this question, we briefly restate the arguments from chapter 2 for the convenience of the reader.

We start from the fact that in the ground state of the classical analog of the Hamiltonian (3.44), all spins are aligned for $b = 0$. However, no direction of alignment is favored, reflecting the full rotational symmetry of the system in spin space. Small local magnetic fields ($b \ll J$), applied in the way described above, break this symmetry and one is left with the two degenerate ground states $\uparrow\uparrow \dots \uparrow$ and $\downarrow\downarrow \dots \downarrow$ where the representation ('quantization') axis is the usual z -direction. In fact, each spin is slightly tilted against its local magnetic field, but there is no *globally* favored direction of orientation, such as with, e.g., a global spatially uniform magnetic field. Note that this effect of tilting vanishes as $b \rightarrow 0$. Due to the Zeeman term in Eq. (3.44) there is an energy barrier between any path connecting the two degenerate minima. In the quantum case, tunneling through this barrier lifts the degeneracy between the ground states and one obtains a tunnel doublet. Thus, in the limit $b \rightarrow 0^+$, the two lowest lying states are the generalized GHZ states given in Eq. (3.1).

As an illustration, we have plotted the energy surface of the classical three-spin system corresponding to Eq. (3.44) in Fig. 2.1 (b). We have previously argued in chapter 2 that this energy can be expressed in terms of two 'mean' spherical angles $\bar{\varphi}$ and $\bar{\vartheta}$ [cf. Fig. 2.1 (a)], since all spins will basically align in the present limit $b \ll J$, up to small fluctuations which sum to zero and are chosen to minimize the total energy. One can nicely see how the out-of-plane configurations at $\bar{\vartheta} = 0$ and $\bar{\vartheta} = \pi$ are energetically favored. For any value of $\bar{\varphi}$, a path connecting the two

minima has to overcome an energy barrier which scales as $O(b^2)$. In the figure, this barrier is displayed by the superimposed white line for the specific value $\bar{\varphi} = \pi/2$.

Independently of N , we are generally confronted with the following problem if we want to achieve the systems considered here to be in a highly entangled state at non-zero temperature. On the one hand, the energy splitting between the ground state and the first excited state vanishes as b goes to zero. On the other hand, a perfect GHZ state is obtained exactly in this limit. For increasing magnetic field, the states continuously deviate from the maximally entangled GHZ state, as can be imagined with the help of the classical picture, where the spins start to tilt. One therefore has to choose the strength of b as a tradeoff between having a highly entangled ground state and separating this state in energy from the next higher state.

In order to find this optimal magnetic field strength at a given temperature $T \neq 0$ we evaluate a suited mixed-state entanglement measure on the system's canonical density matrix $\rho = \exp(-\beta H) / \text{Tr} \exp(-\beta H)$ where $\beta = 1/k_B T$ and k_B is Boltzmann's constant. When we studied the case $N = 3$ in chapter 2 we used the tangle [see Eq. (3.40)] as our pure-state measure of choice, since it is an entanglement measure for three qubits. The generalization to mixed states was done via the convex-roof construction Eq. (3.2). Here, however, we need a pure-state entanglement measure which is defined for any $N \geq 2$.

Entanglement measure

In principle, an exponentially increasing number of distinct entanglement measures is required to capture all possible quantum correlations in a general pure state of N qudits. This may be viewed as the reason for the rather large number of proposals for multipartite entanglement measures that have been put forward over the last years. Various insights about the structure and characterization of multipartite entanglement have been gained by studying such measures. For our purpose, we want to have a measure that is easy (and fast) to compute (in particular, that is an analytic function whose complexity grows at most polynomially with N), that captures the type of entanglement present in our system well, and that possibly has a nice (physical) interpretation. We found that the Meyer-Wallach measure [MW02], defined for an arbitrary number of qubits, fulfills all these criteria. According to Ref. [Bre03], it can be written in the compact form

$$\gamma(|\psi\rangle) = 2 \left[1 - \frac{1}{N} \sum_{k=1}^N \text{Tr}(\rho_k^2) \right], \quad (3.45)$$

where ρ_k is the density matrix obtained by tracing out all but the k th qubit out of $|\psi\rangle\langle\psi|$. This is simply the subsystem linear entropy averaged over all bipartite partitions involving one qubit and the rest [3]. Moreover, it was shown that this entanglement measure is experimentally observable by determining a set of parameters that grows linearly with N , in contrast to the exponentially increasing complexity of quantum state tomography [Bre03]. We note at this point that the Meyer-Wallach entanglement has been generalized to a broader family of entanglement measures [Sco04] that might give deeper insight into the structure of multipartite entanglement. However, we stick to the simple form (3.45) for our numerical calculations, as this measure turns out to describe our type of entanglement well.

The Meyer-Wallach measure is an entanglement monotone (and can thus be extended to mixed states via the convex-roof construction), lies between zero and one, vanishes only for full product states (i.e., states of the form $|\psi\rangle = \bigotimes_i |\psi_i\rangle, i = 1, \dots, N$), and is maximal for generalized GHZ states Eq. (3.1) [4]. The upper bound is however also reached by other states, for instance by the so-called cluster states [Bre03, BR01]. A drawback of the Meyer-Wallach measure is that it can also be maximized by partially separable states. For example, the state $|\Psi\rangle = |\Phi\rangle \otimes |\Phi\rangle$, where $|\Phi\rangle = (|\uparrow\uparrow\rangle + |\downarrow\downarrow\rangle)/\sqrt{2}$ is a bipartite Bell state, gives $\gamma(|\Psi\rangle) = 1$ although it is clearly not globally entangled [Bre03]. This is however not a problem in our study for two reasons. First of all, we can check by numerical diagonalization that the ground state of our systems indeed converges to a multipartite GHZ state (at least for the first few $N \lesssim 20$). Secondly, comparing the data for $N = 3$ with our previous study in chapter 2 where we had employed the tangle, we find the same qualitative behavior of both entanglement measures. Moreover, the optimal values of b for which the measures reach their maxima at a given temperature coincide almost perfectly. It is thus reasonable to assume that the Meyer-Wallach entanglement measure is well suited for quantifying entanglement in our systems.

The numerical evaluation of the Meyer-Wallach measure extended to mixed states via the convex-roof construction requires the derivatives of $\gamma(|\psi\rangle)$ with respect to the real and imaginary components of $|\psi\rangle$ [see Eqs. (3.10, 3.11)]. Due to the partial traces, these expressions are a bit cumbersome. However, exploiting the rotational symmetry of the Hamiltonian studied here, they can be considerably simplified (see Appendix A).

³The subsystem linear entropy $S_L(|\psi\rangle) = 2[1 - \text{Tr}(\tilde{\rho}^2)]$, where $\tilde{\rho} = \text{Tr}_B |\psi\rangle\langle\psi|$, is a well-established bipartite entanglement measure that is often used instead of the von-Neumann entropy in order to simplify calculations [Sco04].

⁴We mention, however, that there are also measures of entanglement which are not maximized by the n -partite GHZ-state Eq. (3.1). Moreover, some measure ascribe this state an unexpectedly low amount of entanglement for $n > 3$. See, e.g., Ref. [BPB⁺07] for an extensive numerical study.

Results

Before we present and discuss our numerical results, we would like to mention that studying the system Eq. (3.44) analytically for arbitrary N is rather difficult. An exact diagonalization of the Hamiltonian is not known for arbitrary N , and perturbation theory to constant order in b (independent of N) is not suitable to study the ground-state properties of the system, since the ground-state splitting is lifted only in N -th order. One can thus generally expect that the ground-state splitting scales with the number of spins as b^N . Since we must always have $b \ll 1$, this goes to zero for large N , as discussed in Sec. 3.4 above. Obtaining highly entangled states at finite temperature with this approach will thus be increasingly difficult for an increasing number of spins N .

Our numerical results are presented in Figs. 3.3 and 3.4. Figure 3.3 shows the Meyer-Wallach measure for $N = 2, 3, 4$, and 5 spins at four different temperatures (see caption of the figure). Each data point is the result of whichever of the two algorithms described in Sec. 3.3 performed better in a few trials with random initial conditions.

For a fixed number of spins, the entanglement as a function of the magnetic field strength b assumes a maximum. This maximal entanglement $\gamma_{\max}(T)$ is increased and its position is shifted to smaller magnetic field values as the temperature is lowered. This is due to the fact that at low temperatures, only a small magnetic field is required in order to make the ground-state splitting sufficiently large compared with temperature. Since these small field values only slightly disturb the ideal GHZ configuration, almost maximal values of the entanglement measure (corresponding to almost perfect GHZ-states) are observed. With higher temperature, larger field values are required to protect the ground state. Consistent with the semiclassical picture, this perturbs the desired spin configuration and leads to a lower amount of entanglement. For large magnetic fields, all curves coincide eventually, as the system is always found in the ground state in that case.

Figure 3.4 gives more insight into the dependence of maximal entanglement $\gamma_{\max}(T)$ on temperature and the number of particles. The plot was obtained by maximizing the Meyer-Wallach measure over the magnetic field strength b (using a simple golden section bracketing algorithm [PTVF92]) while holding the temperature fixed. Displayed is the difference between the resulting data to the zero-temperature maximum (being equal to 1) as a function of temperature for different numbers of particles (see caption of the figure). Clearly, the maximally achievable entanglement $\gamma_{\max}(T)$ decreases for both increasing temperature and increasing number of particles. The qualitative dependence on the temperature was discussed already above. Here we additionally see an almost linear behavior on a log-log scale at low temperatures, suggesting a power-law decay of the maximal entanglement of the form $1 - \gamma_{\max}(T) \propto T^\alpha$ with

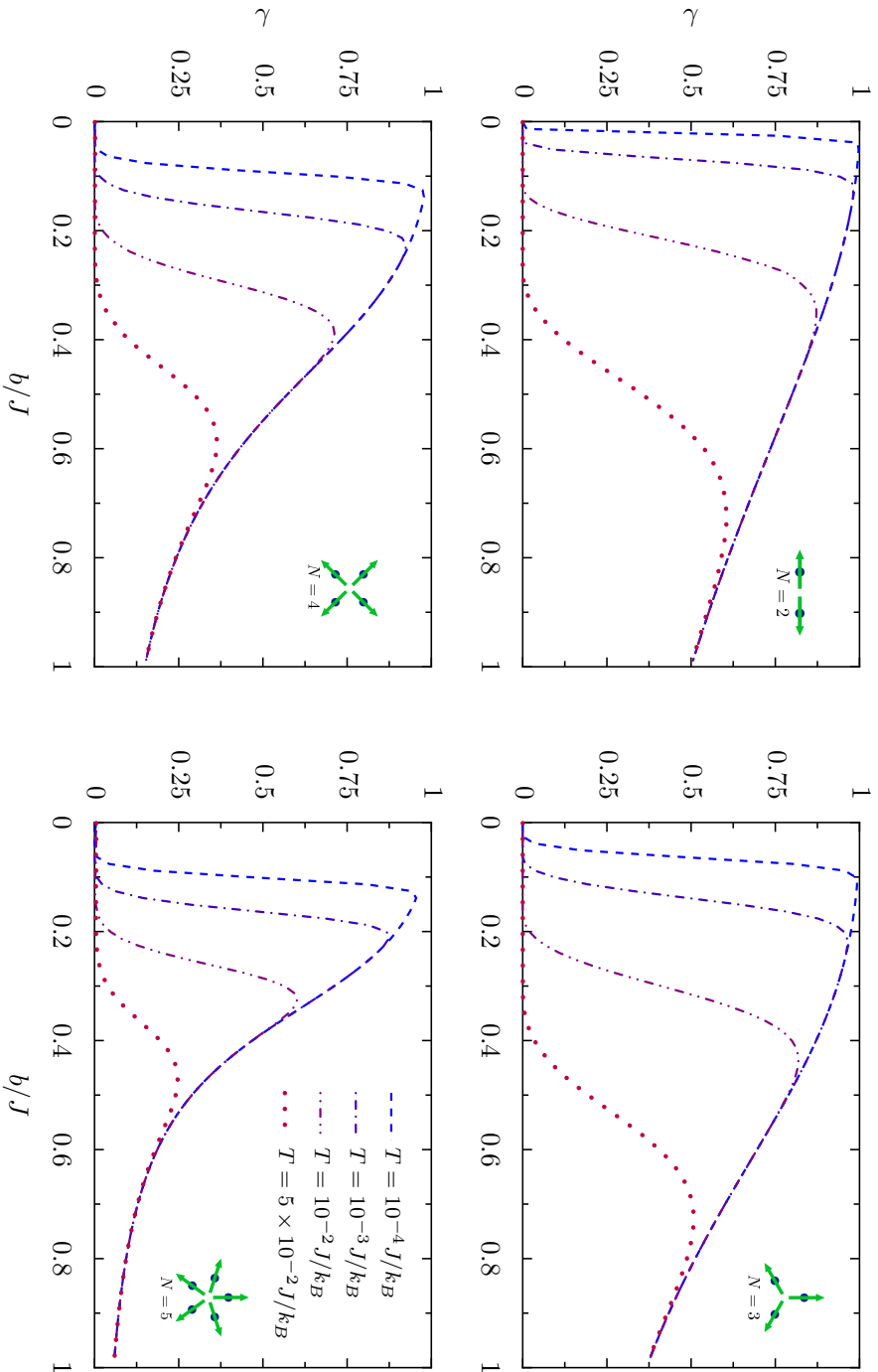


Figure 3.3: Meyer-Wallach entanglement measure for the system described by the Hamiltonian Eq. (3.44) at different temperatures for several numbers of particles. Concretely, the cases $N = 2$ (top left), $N = 3$ (top right), $N = 4$ (bottom left), and $N = 5$ (bottom right) are studied at temperatures $T = 10^{-4} J/k_B$ (dashed line), $T = 10^{-3} J/k_B$ (dashed-dotted line), $T = 10^{-2} J/k_B$ (dashed-dot-dotted line), and $T = 5 \times 10^{-2} J/k_B$ (dotted line).

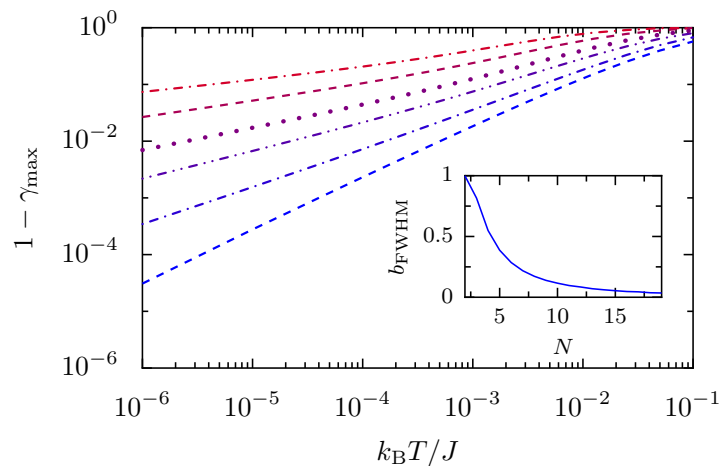


Figure 3.4: Difference between zero-temperature and finite-temperature maximally achievable Meyer-Wallach entanglement measure as a function of temperature for systems with $N = 2, 3, 4, 5, 7, 10$ spins (from bottom to top). Inset: Value of the magnetic field strength b as a function of system size at which the ground state yields the Meyer-Wallach value 0.5 (full width at half maximum).

an exponent α depending on the number of particles N .

The decrease of $\gamma_{\max}(T)$ with the number of spins N at fixed temperature is due to the fact that the energy splitting between the ground and first excited state scales as b^N . With a larger number of particles, a higher magnetic field is required to achieve a sufficiently large splitting. This in turn lowers the entanglement in the ground state, due to its b -dependence, resulting in a lowered maximum of the Meyer-Wallach measure. As an additional obstacle, the ground-state entanglement as a function of b decays even more rapidly as the number of particles is increased. This can be seen from the inset of figure 3.4, where, at $T = 0$, the b -values yielding the Meyer-Wallach measure 0.5 (full width at half maximum, since the maximum at $T = 0$ is always 1) are shown as a function of N .

3.5 Conclusion

We have presented two ready-to-use numerical algorithms to evaluate any generic convex-roof entanglement measure. While one is based on a conjugate gradient algorithm operating directly on the search space, the other one is a quasi-Newton procedure performing the search in the transformed unconstrained Euclidean space. All required formulas to implement either of the two algorithms have been stated explicitly, which, in order to calculate different convex-roof extended pure-state measures,

merely leaves the user with the task of calculating its derivatives with respect to the real and imaginary components of the pure-state argument. The relatively different nature of the two procedures increases the chances that at least one of them performs well in the concrete application. In a series of numerical tests, we have found that the algorithms perform well and especially significantly better than previously presented (non Newton-type) ready-to-use optimization problems on the Stiefel manifold. However, it is found that the convergence properties, as is often the case in involved optimization problems, depend on the cost function. This suggests to try applying different techniques to a particular optimization problem and examine which one performs best in that case.

Further, we have applied our algorithms to evaluate a multipartite entanglement measure on density matrices originating from a real physical system. The latter consists of N ferromagnetically exchange-coupled spin- $\frac{1}{2}$ particles placed on the edges of a regular polygon with N edges. We have argued that a particular local magnetic field geometry, namely radially symmetric in-plane fields, favor a highly entangled ground state configuration. We have confirmed this argumentation by evaluating the mixed-state Meyer-Wallach entanglement measure, defined for an arbitrary number of qubits, and found indeed high values of entanglement at low temperatures and specific magnetic field strengths. This not only quantifies the entanglement properties present in this system, but also serves more generally as a proof-of-principle for the usefulness and applicability of our algorithms.

The Optimization Library

libCreme

Adapted from:
B. Röthlisberger, J. Lehmann, and D. Loss,
“*libCreme: An optimization library for evaluating
convex-roof entanglement measures*”,
Comput. Phys. Commun. **183**, 155 (2012).

We present the software library `libCreme` which we have used in chapters 2 and 3 to calculate convex-roof entanglement measures of mixed quantum states appearing in realistic physical systems. Evaluating the amount of entanglement in such states is in general a non-trivial task requiring to solve a highly non-linear complex optimization problem. The algorithms provided here are able to achieve to do this for a large and important class of entanglement measures. The library is mostly written in the MATLAB programming language, but is fully compatible to the free and open-source OCTAVE platform. Some inefficient sub-routines are written in C/C++ for better performance. This manuscript discusses the most important theoretical concepts and workings of the algorithms, focussing on the actual implementation and usage within the library. Detailed examples in the end should make it easy for the user to apply `libCreme` to specific problems.

4.1 Introduction

The role of non-local quantum correlations, more familiarly known as entanglement, in modern quantum theory cannot be overstated [NC00]. On the one hand, entanglement lies at the heart of quantum information

theory [Ved07], where it is a crucial ingredient to computation and communication schemes. On the other hand, it is intricately related to phenomena such as decoherence [MCKB05] and quantum phase transitions in many-body systems [AFOV08]. One has come to realize that entanglement is also a resource that can for instance be purified, shared, and possibly irreversibly lost, and should therefore not only be detectable, but also quantifiable [HHHH09]. One way of doing so is by virtue of entanglement measures [PV07]. These are mathematical functions mapping quantum states to the set of real numbers. While there is no unique or strict definition for the notion of an entanglement measure, there are a set of properties which are commonly regarded useful, e.g., that the measure is zero only for separable states and is invariant under local unitary transformations. Another important property which we will assume throughout this work is monotonicity: An entanglement measure must not increase (on average) under any protocol involving only local unitary transformations and classical communication. In the following, we will use the terms ‘entanglement measure’ and ‘entanglement monotone’ interchangeably.

Rather understandably, it is difficult to capture all properties of even a pure entangled state with just a single real number, especially in the setting of higher-dimensional and multi-partite systems. It is thus no surprise that there is quite a number of proposed entanglement monotones of various levels of complexity, generality, and the ability to capture different aspects of entangled states more or less successfully than others. As indicated previously, most of these entanglement monotones share the fact that they are conveniently defined only for pure states, namely as a function of the amplitudes of the state expressed in a certain standard basis.

The situation becomes more involved in the case of mixed states, where classical and quantum correlations need to be distinguished from one another. Given a density matrix ρ , it is not sufficient to simply calculate the average entanglement of a given decomposition, because this decomposition is not unique. Since there are in general infinitely many ways to write a density matrix as a sum of projectors onto pure states, only the infimum of entanglement over all these possible decompositions can make a reliable statement about the quantum correlations in ρ , because there might be a decomposition of ρ in which all pure states are separable and the total entanglement hence would vanish. Taking this infimum of an averaged pure-state entanglement monotone over all decompositions of ρ is called ‘convex-roof construction’ or ‘convex-roof extension’ of that monotone [Uhl00]. Notably, the thereby obtained measure for mixed states is again an entanglement monotone. Calculating the convex-roof for a generic quantum state is considered extremely difficult [PV07]. In fact, even deciding whether or not a merely bipartite

mixed state is separable is a hard problem itself which has no known general solution in Hilbert space dimensions larger than six [HHHH09].

In this work, we present the computer programs we have written and successfully applied previously to calculate such convex-roof entanglement measures of multi-partite mixed states in chapters 2 and 3. While we have already described the theory behind our algorithms to some extent in the previous chapter, we complete this work by describing here the full source code in the form a user-friendly high-level library called `libCreme` [1]. The package is to a large part written in the MATLAB programming language [2], but great care has been taken to make the library fully compatible with GNU OCTAVE [3], a free and open-source MATLAB clone. For the sake of simplicity, we will refer to their common language as M-script. Additionally, functions which have been identified as crucial bottlenecks in terms of execution speed are provided in the form of fast C extensions and have been adapted to be easily callable from MATLAB and OCTAVE through their native C and C++ interfaces, respectively.

While the library already comes with the ability to evaluate a choice of popular entanglement monotones, it is easily extend to calculate user-specified functions. All that needs to be implemented is the entanglement measure itself and its gradient with respect to the real and imaginary parts of the quantum state vector [4]. The library is written in a self-contained and consistent way, making it extremely easy to use in practice and to experiment with different settings, measures, and optimization algorithms. Furthermore, we provide convenience functions hiding most of the steps required to arrive at function handles ready to be optimized. This essentially simplifies the calculation of a convex-roof entanglement measure to a one-line task. Table 4.1 lists each function provided in the library together with a short description of its meaning.

We would briefly like to mention two other numerical libraries dealing with quantum computing and entanglement. One is the freely available ‘quantum information package’ by T. Cubitt [5] written in M-script as well. The other one is the CPC library FEYNMAN (catalog identifier ADWE_v5_0) written by T. Radtke and S. Fritzsche [RF10] for MAPLE.

¹The library can be downloaded at <http://goo.gl/kXZJD>.

²See <http://www.mathworks.com/products/matlab/>.

³See <http://www.gnu.org/software/octave/>.

⁴It is easily seen from the Cauchy-Riemann equations that non-constant functions from \mathbb{C} to \mathbb{R} , such as the kind of entanglement measures we are addressing in this work, cannot be analytic. We therefore have to treat the real and imaginary part of complex numbers as independent variables.

⁵Package can be downloaded at <http://www.dr-qubit.org/matlab.php>.

Entanglement measures

<code>convexSum</code>	Convex sum parameterized by a Stiefel matrix
<code>grad_convexSum</code>	Gradient of convex sum
<code>eof2x2</code>	Entanglement of formation for 2 qubits (analytically exact result)
<code>entropyOfEntanglement</code>	Entropy of entanglement
<code>grad_entropyOfEntanglement</code>	Gradient of entropy of entanglement
<code>meyer_wallach</code>	Meyer-Wallach measure
<code>grad_meyer_wallach</code>	Gradient of Meyer-Wallach measure
<code>tangle</code>	Tangle
<code>grad_tangle</code>	Gradient of Tangle

Optimization routines

<code>cg_min</code>	Conjugate-gradient method
<code>bfgs_min</code>	BFGS quasi-Newton method
<code>minimize1d_exp</code>	Minimization along a geodesic on the Stiefel manifold
<code>minimize1d_lin</code>	Minimization along a line in Euclidean space
<code>get_termination_criteria</code>	Helper function to check and handle termination criteria for the optimization algorithms

Utilities

<code>randDensityMatrix</code>	Random density matrix
<code>randState</code>	Random pure quantum state
<code>randUnitaryMatrix</code>	Random Stiefel matrix
<code>decomposeUnitary</code>	Get angles parameterizing a Stiefel matrix
<code>dimSt</code>	Dimension of Stiefel manifold
<code>densityEig</code>	Get eigendecomposition of a density matrix in the form required by many functions within the library
<code>psDecomposition</code>	Get pure-state decomposition parameterized by a Stiefel matrix
<code>createConvexFunctions</code>	Create convex-sum function handles for use with <code>cg_min</code>
<code>createEHFunctions</code>	Create convex-sum function handles for use with <code>bfgs_min</code>
<code>grad_eh_adapt</code>	Adapter function to calculate the gradient of a convex sum parameterized by Stiefel matrix angles

<code>buildUnitary</code>	Build a complex Stiefel matrix from a parameterization vector
<code>grad_buildUnitary</code>	Gradient of the above function
<code>pTrace</code>	Partial trace over any subsystems of arbitrary (finite) dimensions
<code>completeGramSchmidt</code>	Helper function for numerical stability used within <code>cg_min</code>
<i>Examples</i>	
<code>example_eofIsotropic</code>	Main script to run the example from Sec. 4.5
<code>eofIsotropic</code>	Entanglement of formation of an ‘isotropic’ density matrix (analytically exact result)
<code>example_tangleGHZW</code>	Main script to run the example from Sec. 4.5
<code>tangleGHZW</code>	Tangle of GHZ/W mixture (analytically exact result)

Table 4.1: List of all functions within `libCreme`. Additional information about the usage of each function can be obtained by calling ‘`help function_name`’ from within `MATLAB` or `OCTAVE`.

Quantum states obtained from calculations and simulations within these libraries can conveniently be analyzed further using `libCreme`’s ability to calculate more complex entanglement measures.

This chapter is organized as follows: In Sec. 4.2, we briefly list and discuss the default entanglement measures coming along with `libCreme`. Sec. 4.3 reviews the theory of convex-roof entanglement measures and how to address their calculation on a computer. Sec. 4.4 describes the two central algorithms in `libCreme` to solve the optimization problem related to the evaluation of such measures. In Sec. 4.5, we discuss two complete examples demonstrating the usage of the library, and Sec. 4.6 concludes the work. Note that the focus of this manuscript lies mainly on the functionality of the library: We have tried to provide short code examples throughout this chapter for all important functions and concepts in a user-friendly bottom-up way. These snippets are all valid M-script (including the line breaks ‘`...`’ which we sometimes use due to spacial restrictions) and can be copied directly into `MATLAB` or `OCTAVE`. Finally, we would like to mention that all functions in `libCreme` are documented, and more information about them can be inquired by calling ‘`help function_name`’.

4.2 Entanglement measures included in the library

We start the description of our library by listing the entanglement measures currently implemented. Note that pure quantum states, such as the arguments of functions calculating entanglement monotones, are always expected to be represented as column vectors in the standard computational basis. In practice, this means that the n orthonormal basis states $|\psi_i\rangle$ of each n -dimensional subsystem (where n may be different for different subsystems) are always chosen as $|\psi_1\rangle = (1, 0, \dots, 0)^T$, $|\psi_2\rangle = (0, 1, 0, \dots, 0)^T, \dots, |\psi_n\rangle = (0, 0, \dots, 1)^T$. Multipartite states are then assumed to be represented consistently with the implementation of the M-script command `kron`, i.e., the Kronecker product of two arbitrary input matrices.

Since the optimization algorithms used in `libCreme` are gradient-based, the gradients of these measures with respect to the real and imaginary parts of the input state vector are also provided. The convention is that gradients (i) are named identical to the original functions but with the prefix `'grad_'` added, (ii) require the same arguments as their function counterparts, and (iii) return derivatives with respect to real and imaginary parts of a variable in the form $[\nabla f(x)]_i = \partial f / \partial \text{Re } x_i + i \partial f / \partial \text{Im } x_i$, where i is the imaginary unit. Analytical expressions for all gradients of the measures discussed in this section can be found in B.

Entropy of entanglement

The entropy of entanglement [BBPS96] is an entanglement monotone for bipartite quantum systems of arbitrary dimensions. It is defined as the von Neumann-entropy of the reduced density matrix, i.e.,

$$E(|\psi\rangle) = -\text{Tr}[(\text{Tr}_B \rho) \log_2(\text{Tr}_B \rho)], \quad (4.1)$$

where $\text{Tr}_B \rho$ denotes the partial trace of $\rho = |\psi\rangle\langle\psi|$ over the second subsystem (note that one could equally use the trace over the first subsystem). This measure is implemented in `entropyOfEntanglement` and requires as a first argument the state vector to be evaluated, and as the second a two-dimensional row vector specifying the dimensions of the two subsystems. Note that `entropyOfEntanglement` makes use of `pTrace`, a C/C++ implementation for the fast calculation of partial traces over an arbitrary set and number of subsystems of arbitrary dimensions. Usage:

```
% Create states p_01 and p_10 in the total
% Hilbert space of two qubits by applying the
% Kronecker product to the single-qubit basis
% states [1; 0] and [0; 1].
```

```

%
% Note that in M-script, [a1; a2; ... an]
% denotes a column vector, whereas
% [a1, a2, ... an] is a row vector.
p_01 = kron([1; 0], [0; 1]);
p_10 = kron([0; 1], [1; 0]);

% Define a random superposition of the
% above states.
%
% rand() yields a random number chosen
% uniformly from the interval (0, 1).
r1 = 2*pi*rand(); r2 = 2*pi*rand();
psi = sin(r1)*p_01 + exp(1i*r2)*cos(r1)*p_10;

% Dimensions of subsystems
sys = [2, 2];

% Calculate measure and gradient
e = entropyOfEntanglement(psi, sys)
g = grad_entropyOfEntanglement(psi, sys)

```

Note that the entropy of entanglement is of particular importance, because its convex-roof extension is the well-known and widely used ‘entanglement of formation’ [BDSW96]. In the special case of a bipartite system composed of two-dimensional subsystems (qubits), there exists an operational solution for the entanglement of formation [Woo98], which we have implemented in `eof2x2`.

Three-tangle

The three-tangle [CKW00] is defined specifically for a system of three two-dimensional subsystems. It reads

$$\tau(|\psi\rangle) = 4 |d_1 - 2d_2 + 4d_3|, \quad (4.2)$$

where

$$d_1 = \psi_1^2\psi_8^2 + \psi_2^2\psi_7^2 + \psi_3^2\psi_6^2 + \psi_5^2\psi_4^2, \quad (4.3)$$

$$d_2 = \psi_1\psi_8\psi_4\psi_5 + \psi_1\psi_8\psi_6\psi_3 + \psi_1\psi_8\psi_7\psi_2 \\ + \psi_4\psi_5\psi_6\psi_3 + \psi_4\psi_5\psi_7\psi_2 + \psi_6\psi_3\psi_7\psi_2, \quad (4.4)$$

$$d_3 = \psi_1\psi_7\psi_6\psi_4 + \psi_8\psi_2\psi_3\psi_5, \quad (4.5)$$

and $\psi_i, i = 1 \dots, 8$, are the complex amplitudes of the vector $|\psi\rangle$ in the standard computational basis. The tangle is implemented in the function `tangle`, taking an 8-dimensional vector `psi` as its only argument. Here follows a short example:

```

% Define an 8-dimensional random state
psi = randState(8);

% Calculate tangle and its gradient
t = tangle(psi)
g = grad_tangle(psi)

```

In the above code, we have introduced the function `randState`, which returns a random pure quantum state of arbitrary specified dimension uniformly distributed according to the Haar measure of the unitary group [Mez07].

Meyer-Wallach measure

Finally, the measure of Meyer and Wallach [MW02] for an arbitrary number N of qubits is an entanglement monotone that can be written in the compact form [Bre03]

$$\gamma(|\psi\rangle) = 2 \left[1 - \frac{1}{N} \sum_{k=1}^N \text{Tr}(\rho_k^2) \right], \quad (4.6)$$

where ρ_k is the density matrix obtained by tracing out all but the k th subsystem out of $|\psi\rangle\langle\psi|$. The implementation is given in `meyer_wallach`. This function also makes use of `pTrace`. The usage is analogous to the example given for the three-tangle above.

4.3 Theoretical background

In this section, we review how to arrive at an optimization problem (whose solution is the desired value of the convex-roof entanglement measure) in a form that can be dealt with on a computer. Let m be an entanglement monotone for pure states from a Hilbert space \mathcal{H} of finite dimension d . Let ρ be a density matrix acting on that space. Our goal is to numerically evaluate the convex roof $M(\rho)$ of m , given by

$$M(\rho) = \inf_{\{p_i, |\psi_i\rangle\} \in \mathfrak{D}(\rho)} \sum_i p_i m(|\psi_i\rangle), \quad (4.7)$$

where

$$\mathfrak{D}(\rho) = \left\{ \{p_i, |\psi_i\rangle\}_{i=1}^k, k \geq \text{rank } \rho \mid \{|\psi_i\rangle\}_{i=1}^k \subset \mathcal{H}, \right. \\ \left. \langle\psi_i|\psi_i\rangle = 1, p_i \geq 0, \sum_{i=1}^k p_i = 1, \rho = \sum_{i=1}^k p_i |\psi_i\rangle\langle\psi_i| \right\} \quad (4.8)$$

is the set of all pure-state decompositions of ρ . With respect to numerical optimization, a convenient parameterization of all subsets of $\mathfrak{D}(\rho)$ with a constant number of terms k (sometimes referred to as the ‘cardinality’) is due to the Schrödinger-HJW theorem [HJW93, Kir05]. The latter states that (i), every decomposition of a density matrix ρ with $\text{rank } \rho = r$ into a convex sum of k projectors onto pure states can be expressed in terms of a complex $k \times r$ matrix U obeying $U^\dagger U = \mathbb{I}_{r \times r}$ and that (ii), conversely, from every such matrix one can obtain a pure-state decomposition of ρ . The set $St(k, r) = \{U \in \mathbb{C}^{k \times r} | U^\dagger U = \mathbb{I}_{r \times r}\}$ with $k \geq r$ is also known as the Stiefel manifold. Part (i) and (ii) together ensure that optimizing over $St(k, r)$ is equivalent to optimizing over the full subset of $\mathfrak{D}(\rho)$ with fixed cardinality k . Part (ii) also provides an explicit construction of the pure-state decomposition related to an arbitrary given matrix $U \in St(k, r)$: Let $\lambda_i, |\chi_i\rangle, i = 1, \dots, r = \text{rank } \rho$ be the non-zero eigenvalues and corresponding normalized eigenvectors of ρ , i.e.,

$$\rho = \sum_{i=1}^r \lambda_i |\chi_i\rangle \langle \chi_i|, \quad (4.9)$$

and $\langle \chi_i | \chi_j \rangle = \delta_{ij}$. Note that we have $\lambda_i > 0$ due to the positive semi-definiteness of ρ . Define the auxiliary states

$$|\tilde{\psi}_i\rangle = \sum_{j=1}^r U_{ij} \sqrt{\lambda_j} |\chi_j\rangle, \quad i = 1, \dots, k, \quad (4.10)$$

and set

$$p_i = \langle \tilde{\psi}_i | \tilde{\psi}_i \rangle, \quad (4.11)$$

$$|\psi_i\rangle = (1/\sqrt{p_i}) |\tilde{\psi}_i\rangle. \quad (4.12)$$

One can easily verify that we have

$$\rho = \sum_{i=1}^k p_i |\psi_i\rangle \langle \psi_i|. \quad (4.13)$$

In `libCreme`, the function `densityEig` calculates only the non-zero eigenvalues and corresponding eigenvectors. The eigenvalues are guaranteed to be sorted in decreasing order, which is particularly convenient if one wishes to discard some parts of the density matrix occurring with low probability, such as, e.g., high-energy sectors in density matrices $\rho \sim \exp(-\beta H)$ originating from some Hamiltonian H . The function `psDecomposition` returns the pure-state decomposition from Eqs. (4.9, 4.10, 4.11, 4.12). As an example, let `rho` store a $d \times d$ density matrix of rank r , and let `U` be a matrix from $St(k, r)$, with arbitrary $k \geq r$. Then

```

% Note that in M-script, functions can return
% multiple values of arbitrary dimensions. The
% syntax to assign several return values to
% local variables is
% [A, B, ...] = foo(...);
[chi, lambda] = densityEig(rho);
[psi, p] = psDecomposition(U, chi, lambda);

```

first yields the eigenvectors of ρ in the columns of the $d \times r$ matrix chi with the corresponding r eigenvalues in the vector lambda . On the second line then, the pure-state decomposition of ρ (given in terms of the parameters chi and lambda) corresponding to the parameterization U is calculated, with the k state vectors $|\psi_i\rangle$ stored in the columns of the $d \times k$ matrix psi and the k corresponding probabilities p_i in the vector p .

By virtue of the Schrödinger-HJW theorem, we can restate the optimization problem Eq. (4.7) as

$$M(\rho) = \min_{k \geq r} \inf_{U \in \text{St}(k,r)} h(U), \quad (4.14)$$

$$h(U) = \sum_{i=1}^k p_i(U) m(|\psi_i(U)\rangle), \quad (4.15)$$

where the dependence on ρ enters implicitly as the dependence of the p_i and $|\psi_i\rangle$ on the eigenvalues and eigenvectors of ρ . In practice, it has turned out to be possible to drop the minimization over k completely and set k to a constant but large enough value instead. Note that this actually includes all cardinalities k' with $r \leq k' \leq k$ in the search because up to $k - r$ of the p_i are allowed to go to zero without breaking the optimization constraint. In `libCreme`, the function `convexSum` calculates the value of the expression $h(U)$ in Eq. (4.15), which is, in fact, the objective function of the optimization. `convexSum` takes as its first argument a parameterization matrix from the Stiefel manifold, as its second a function handle [6] to the entanglement monotone to be extended, and as its third and fourth arguments the eigendecomposition of the density matrix obtained by `densityEig`. Here is a full example:

⁶In M-script, functions can be passed as arguments using ‘function handles’ (conceptually similar to function pointers in C). For a function with name `foo`, the corresponding function handle is given by `@foo`. Subroutines are then able to call `foo` through its function handle, given the number and type of parameters are correct. A related feature of M-script used frequently in `libCreme` are ad hoc, also called ‘anonymous’, function handles. These are handles to functions which are neither built-in, nor defined in a script file, but rather created on the spot. As an example, consider the following syntax to create a function of two parameters calculating the sine of the parameter’s product:

```
sinxy = @(x, y) sin(x*y);
```

The variable names used to define the function are listed in the parentheses after

```

% Random 8-by-8 density matrix
rho = randDensityMatrix(8);

% Calculate eigendecomposition of rho for
% later use
[chi, lambda] = densityEig(rho);

% Random matrix from St(12, 8)
U = randUnitaryMatrix(12, 8);

% Evaluate convex sum Eq. (15) with the tangle
h = convexSum(U, @tangle, chi, lambda)

```

Note that we have introduced the functions `randDensityMatrix` and `randUnitaryMatrix` to create random density matrices and random matrices from the Stiefel manifold, respectively. It is important to understand that `convexSum` is the key function in the whole library in the sense that it is always this function (or more specifically, an anonymous function handle to it, see Sec. 4.4), which is ultimately optimized.

As mentioned earlier, the optimization algorithms in `libCreme` require the knowledge of the gradient of the objective function, or more precisely, the derivatives of $h(U)$ with respect to the real and imaginary parts of the matrix elements of U . These expressions and their derivation can be found in C. Within the library, this gradient of h is implemented in `grad_convexSum`. It requires 5 arguments: The matrix U , the entanglement monotone to be extended, the gradient of the latter, and the eigendecomposition of ρ (eigenvectors and -values). The following code illustrates its application in practice, using the variables `chi`, `lambda`, and `U` from the previous example:

```

% Evaluate gradient of the convex sum Eq. (15),
% given in Eqs. (B4 - B7) with the tangle
gh = grad_convexSum(U, @tangle, ...
    @grad_tangle, chi, lambda)

```

the '@' sign. Directly following is the actual definition of the function. It can then be called in the usual way, yielding, e.g.,

```

>> sinxy(0.5, pi)

ans =

1

```

4.4 Optimization algorithms

We describe in this section two conceptually different optimization algorithms which are both provided in `libCreme`. One is a conjugate gradient method based on the concepts introduced in Refs. [EAS98, AVDM01, AMS08]. It exploits the differential-geometric structure of the nonlinear search space emerging from the optimization constraint $U^\dagger U = \mathbb{I}$. The other algorithm is a standard Broyden-Fletcher-Goldfarb-Shanno (BFGS) quasi-Newton method employing a transformation of the constrained search space to an unconstrained one. Both algorithms have been discussed in greater detail in chapter 3, where the expressions for the gradients and parameterization of the Stiefel manifold given below have been derived. Here, we just state the final results for the sake of completeness and focus particularly on the implementation and usage within `libCreme`.

Conjugate-Gradient Method

This algorithm exploits the geometric structure of the unitary group $U(k) = St(k, k)$ and therefore generally over-parameterizes the true search space $St(k, r)$, $r \leq k$. This is however not a problem in practice, since we can simply discard the last $k - r$ columns of U when calculating the decomposition of the density matrix based on U [7]. The full algorithm for an input initial guess U_0 is given as follows:

1. Initialization: Set $i \leftarrow 0$. Calculate the gradient $G_0 = G(U_0)$ according to the formula

$$G(U) = \frac{1}{2}(A(U) - A(U)^T) + \frac{\mathbf{i}}{2}(S(U) + S(U)^T), \quad (4.16)$$

where the matrices $A(U)$ and $S(U)$ are given by

$$A(U) = \operatorname{Re} U^T \cdot \nabla_{\operatorname{Re} U} h(U) + \operatorname{Im} U^T \cdot \nabla_{\operatorname{Im} U} h(U), \quad (4.17)$$

$$S(U) = \operatorname{Re} U^T \cdot \nabla_{\operatorname{Im} U} h(U) - \operatorname{Im} U^T \cdot \nabla_{\operatorname{Re} U} h(U), \quad (4.18)$$

and the gradient of $h(U)$ can be found in C.

Finally, set $X_0 \leftarrow -G_0$.

2. Perform the one-dimensional minimization

$$t_{i+1} \leftarrow \arg \min_t h(U_i \exp(tX_i)), \quad (4.19)$$

⁷However, in the case where one chooses $k \gg r$, it is advantageous to employ an algorithm that works directly on the Stiefel manifold instead of the unitary group. The concepts discussed in Ref. [EAS98] for the real Stiefel manifold can be adapted to the complex case by replacing transpositions with Hermitian conjugates and the Frobenius inner product $\langle X, Y \rangle = \operatorname{Tr} X^T Y$ by $\langle X, Y \rangle = \operatorname{Re} \operatorname{Tr} X^\dagger Y$.

set

$$U_{i+1} \leftarrow U_i \exp(t_{i+1} X_i), \quad (4.20)$$

and compute the new gradient $G_{i+1} \leftarrow G(U_{i+1})$ according to Eqs. (4.16, 4.17, 4.18).

3. Define

$$T \leftarrow \exp(t_{i+1} X_i / 2) G_i \exp(-t_{i+1} X_i / 2). \quad (4.21)$$

T is the gradient G_i parallel-transported to the new point U_{i+1} .

4. Calculate the modified Polak-Ribière parameter

$$\gamma \leftarrow \frac{\langle G_{i+1} - T, G_{i+1} \rangle}{\langle G_i, G_i \rangle}, \quad (4.22)$$

where $\langle X, Y \rangle = \text{Tr } XY^\dagger$.

5. Set the new search direction to

$$X_{i+1} \leftarrow -G_{i+1} + \gamma X_i. \quad (4.23)$$

6. Set $i \leftarrow i + 1$.

7. Repeat from step 2 until convergence.

This algorithm is implemented in the function `cg_min`. The minimization in step 2 is performed by the derivative-based method `minimize1d_exp`. `cg_min` requires the function to be minimized, its gradient, an initial point, and optionally a struct with user-specified termination criteria discussed below. At this point, we would like to work through a full example demonstrating the use of `cg_min` to calculate the convex-roof extended three-tangle of a mixed state.

```
% Random 8-by-8 density matrix
rho = randDensityMatrix(8);

% Calculate eigendecomposition of rho for
% later use
[chi, lambda] = densityEig(rho);

% Define anonymous function handles to
% the objective function and its gradient
f_opt = @(x) convexSum(x, @tangle, ...
    chi, lambda);
g_opt = @(x) grad_convexSum(x, @tangle, ...
    @grad_tangle, chi, lambda);
```

```

% Choose a random starting point, here for
% a decomposition with cardinality 12
U0 = randUnitaryMatrix(12, 12);

% Perform the optimization
[t, Ut, info] = cg_min(f_opt, g_opt, U0);

```

A few comments about the above code are in order. First, note that because `cg_min` requires the objective and its gradient in the form of one-parameter functions, we need to define the anonymous function handles `f_opt` and `g_opt` before continuing. In this way, `f_opt` is a new function that evaluates `convexSum` at a variable unitary input matrix while keeping the constant arguments `@tangle`, `chi`, and `lambda` fixed. A similar description holds for `g_opt`. Second, note that the initial search point `U0` is a unitary and therefore square matrix, although matrices from $St(12, 8)$ would be sufficient in the example above to parameterize pure-state decompositions. The reason is, as mentioned above, that `cg_min` is operating on the unitary group instead of the Stiefel manifold. However, this is hidden from the user by the fact that both `convexSum` and `grad_convexSum` can accept larger input than required, and automatically discard any dispensable columns. Third, we would like to draw the reader's attention to the output values of `cg_min`. In the above example, `t` stores the convex-roof of the entanglement monotone to be evaluated (in this case the three-tangle) and `Ut` (or more precisely, the first r columns of it) represent the pure-state decomposition of ρ arriving at this value. The variable `info` is a struct that carries useful additional information, namely the criterion that terminated the iteration (`info.status`), the function values along the iteration, excluding intermediate values during line searches (`info.fvals`), and finally, the traversed points in the search space corresponding to `fvals` (`info.xvals`).

An optional fourth argument containing settings for the termination of the algorithm can be passed to `cg_min`. The following code illustrates the possible struct variables (the values in this example are also the defaults for any variables not set).

```

% Create a struct
opts = struct();

% Maximum number of iterations
opts.MaxIter = 1000;

% Tol. on consecutive function values
opts.TolFun = 1e-12;

% Tolerance on norm of difference between

```

```

% two consecutive gradients
opts.TolG = 1e-10;

% Tolerance on norm of difference between
% two consecutive iteration points
opts.TolX = 1e-10;

```

The iteration is stopped if either the maximum number of iterations is reached, or one of the checked values is lower than its respective tolerance. Finally, we would like to mention that for the convenience of the user, there is a function called `createConvexFunctions` which performs all the necessary steps before the actual optimization in one line:

```

% Again using the tangle as an example
[f_opt, g_opt] = createConvexFunctions(rho, ...
                                     @tangle, @grad_tangle);
[t, Ut, info] = cg_min(f_opt, g_opt, U0);

```

As with any other numerical optimization procedure, it is advisable to repeat the computations with different (random) initial conditions in order to reach a better approximation to the global minimum.

BFGS Quasi-Newton Method

The second algorithm is a classical BFGS quasi-Newton method [NW99] that makes use of a transformation which is able to unconstrain the optimization problem Eq. (4.14) from the Stiefel manifold to ordinary Euclidean space. This transformation is conceptually identical to the example where one has an optimization problem with the constraint $x^2 + y^2 = 1$ and then sets $x = \sin \theta$, $y = \cos \theta$ and performs the optimization over the new variable θ . Again, we only state in the following the main results required to implement the algorithm and refer the reader interested in a thorough derivation to the previous chapter.

The number of independent real parameters required to parameterize $St(k, r)$ is equal to its dimension which is given by $\dim St(k, r) = 2kr - r^2$. Given a tuple of ‘angles’ X_i , $i = 1, \dots, \dim St(k, r)$, we relabel them in the following (arbitrary but fixed) way: $\vartheta = \{X_i\}$ for $i = 1, \dots, r[k - (r + 1)/2]$, $\varphi = \{X_i\}$ for $i = r[k - (r + 1)/2] + 1, \dots, r(2k - r - 1)$, and $\chi = \{X_i\}$ for $i = r(2k - r - 1) + 1, \dots, \dim St(k, r)$. Then, we calculate $U \in St(k, r)$ according to

$$U(X) \equiv U(\vartheta, \varphi, \chi) = \left[\prod_{i=1}^r \prod_{j=1}^{k-i} G_{k-j}^{-1}(\vartheta_{c_{ij}}, \varphi_{c_{ij}}) \right] R \quad (4.24)$$

where $c_{ij} = (i - 1)(k - i/2) + j$, R is a $k \times r$ matrix with the only non-zero elements being $R_{ii} = \exp(i\chi_i)$ for $i = 1, \dots, r$, and the ‘inverse Givens

matrices' G_s^{-1} are defined in terms of their matrix elements as

$$[G_s^{-1}(\vartheta, \varphi)]_{ij} = \begin{cases} e^{-i\varphi} \cos \vartheta, & \text{if } i = j = s, \\ -e^{-i\varphi} \sin \vartheta, & \text{if } i = s, j = s + 1, \\ e^{i\varphi} \sin \vartheta, & \text{if } i = s + 1, j = s, \\ e^{i\varphi} \cos \vartheta, & \text{if } i = s + 1, j = s + 1, \\ \delta_{ij}, & \text{otherwise.} \end{cases} \quad (4.25)$$

In `libCreme`, calculating a Stiefel matrix from a vector of angles X by Eq. (4.24) is implemented in `buildUnitary` as a fast C/C++ extension and is demonstrated in the following:

```
% Dimensions of the Stiefel manifold
k = 10; r = 7;

% Random vector of angles with proper size
% (Uses dimSt for the dimension of the
% Stiefel manifold).
%
% randn(m, n) yields an m-by-n matrix of
% normally distributed random numbers.
X = 2*pi*randn(1, dimSt(k, r));

% Finally, the Stiefel matrix
U = buildUnitary(X, k, r);
```

The derivatives of $U(X)$ with respect to the angles X_i are implemented in the function `grad_buildUnitary`. The inverse operation of `buildUnitary`, namely obtaining the parameterizing angles for a given matrix U can be performed by `decomposeUnitary` as in

```
X = decomposeUnitary(U);
```

This function is implemented in regular in M-script, because it is called only infrequently and thus is not time critical.

We have now all the tools to describe the full BFGS quasi-Newton algorithm starting from an initial vector of angles X_0 .

1. Set $i \leftarrow 0$, $H_0 \leftarrow \mathbb{I}$, $G_0 = \nabla_X h(U(X))|_{X=X_0}$, and $S_0 = -G_0$. H_0 is the initial guess for the approximate Hessian, h is the convex sum Eq. (4.15), and $U(X_0)$ is the transformation Eq. (4.24).
2. Perform the line minimization

$$t_{i+1} \leftarrow \arg \min_t h(U(X_i + tS_i)) \quad (4.26)$$

and set

$$X_{i+1} \leftarrow X_i + t_{i+1}S_i. \quad (4.27)$$

3. Compute the new gradient

$$G_{i+1} \leftarrow \nabla_X h(U(X))|_{X=X_{i+1}}. \quad (4.28)$$

4. Update the approximate Hessian as [Fle00]

$$H_{i+1} \leftarrow H_i + \left(1 + \frac{\gamma^T (H_i \gamma)}{\delta^T \gamma} \right) \frac{\delta \delta^T}{\delta^T \gamma} - \frac{\delta^T (H_i \gamma) + (H_i \gamma)^T \delta}{\delta^T \gamma}, \quad (4.29)$$

where the column vectors δ and γ are defined as $\delta = X_{i+1} - X_i$ and $\gamma = G_{i+1} - G_i$.

5. Set the new search direction to

$$S_{i+1} \leftarrow -H_{i+1} G_{i+1}. \quad (4.30)$$

6. Set $i \leftarrow i + 1$.

7. Repeat from step 2 until convergence.

The line minimization in step 2 is performed by `minimize1d.lin`, a subroutine that is conceptually identical to the function `minimize1d.exp` used above in the conjugate-gradient method. The full algorithm is implemented in `bfgs_min` and its input and output parameters are identical to the ones in `cg_min`. Hence, the descriptions in the previous section can be adapted analogously to `bfgs_min`. However, the target function (and its gradient) look slightly different in the current case and are somewhat more cumbersome in terms of function handles, because the additional intermediate transformation Eq. (4.24) needs to be incorporated. The following is a fully working example that should help to clarify this issue.

```
% Random 8-by-8 density matrix
rho = randDensityMatrix(8);
[chi, lambda] = densityEig(rho);

% Convex-sum function handles for the tangle
f_cr = @(x) convexSum(x, @tangle, ...
                    chi, lambda);
g_cr = @(x) grad_convexSum(x, @tangle, ...
                          @grad_tangle, chi, lambda);

% Dimensions of the Stiefel manifold
r = rank(rho);
k = r + 4;
```

```

% Objective function and gradient
f_opt = @(x) f_cr(buildUnitary(x, k, r));
g_opt = @(x) grad_eh_adapt(x, k, r, g_cr);

% Choose a random starting point
X0 = 2*pi*randn(1, dimSt(k, r));

% Perform the optimization
[t, Xt, info] = bfgs_min(f_opt, g_opt, X0);

```

Notice the use of the auxiliary function `grad_eh_adapt` which calculates the gradient $\nabla_X h(U(X))$ given the derivatives of $h(U)$ with respect to the real and imaginary matrix elements of U . For the convenience of the user, there is a function that hides all the above steps just like in the case of the conjugate-gradient algorithm. It is called `createEHFunctions` and is analogously called, as exemplified here:

```

[f_opt, g_opt] = createEHFunctions(rho, ...
                                k, r, @tangle, @grad_tangle);
[t, Xt, info] = bfgs_min(f_opt, g_opt, X0);

```

Clearly, the same note as in the previous section regarding multiple restarts holds.

Finally, we would like to make a remark about a detail in our implementation of `bfgs_min`. It has shown to be useful in practice to reset the angles modulo 2π every few iterations. This improves numerical stability and convergence in the vicinity of a minimum. It is also advisable to vary the interval size after which this is done as this can improve performance depending on the problem. If `bfgs_min` is to be employed for non-periodic functions, these lines of code must be removed.

General Remarks

Before we end this section and look at some more examples, we would like to make a few comments. At this point, the reader might wonder why we provide our own implementation of a line search and a BFGS quasi-Newton method, instead of resorting to the functions available in MATLAB and OCTAVE. There are several reasons for that. First of all, it makes the library independent of the platform, since the standard routines in MATLAB and OCTAVE work differently and hence generally produce unequal results. Furthermore, having a simple implementation at hand allows the user to quickly make modifications and customize the code to specific needs. In OCTAVE this can only be achieved with quite an effort, whereas in MATLAB it is generally not possible at all. Additional issues are availability and backward-compatibility. While MATLAB's optimization framework is well established, it is only available

through the purchase of the ‘MATLAB Optimization Toolbox’. On the other hand, there is a free octave package for non-linear optimization tasks [8]. But since this is still under active development, its usage within libCreme might potentially become incompatible with future releases of the package.

Next we would like to address the performance of the algorithms as a function of $r = \text{rank } \rho$ and $k \geq r$. The dimension of the Stiefel manifold (and hence the problem size) is given by $\dim St(k, r) = 2kr - r^2$. Since we must have $k \geq r$, we can replace it by $k = r + n$, with $n \geq 0$, yielding $\dim St(k, r) = r^2 + 2nr$. This shows that the computational cost grows quadratically with the rank of ρ , but only linearly with the (user-specified) cardinality. The algorithms in the library are thus most efficient for low-rank density matrices, whereas experimenting with different cardinalities is not that costly. Actually, already choices for n as low as $n \approx 4$ have shown to produce very accurate results in practice (see also below). Since, on the other hand, the scaling with r is less favorable, it is advisable to examine whether the rank of r can be reduced. Particularly in density matrices originating from physical Hamiltonians it is often justified to neglect high-energy states. As mentioned earlier, reducing the rank of ρ can conveniently be achieved by truncating the output of the function `densityEig`.

4.5 Examples

In this section, we demonstrate the usage of libCreme by working through two complete examples. We calculate the entanglement of special states where analytical results are known in order to compare the numerical experiments with theory. Note that we provide initial points for the optimization in separate files instead of generating them randomly, because (i) the random number generators in MATLAB and OCTAVE produce different sequences of random numbers and (ii) not every initial point leads to the convergence to a global minimum in such high-dimensional spaces.

Entanglement of formation of isotropic states using `cg_min`

Isotropic states are defined as a convex mixture of a maximally entangled state and the maximally mixed state in a system of two d -dimensional subsystems. The isotropic state with an amount of mixing specified by f , where $0 \leq f \leq 1$, is given by [TV00]

$$\rho_f = \frac{1-f}{d^2-1}(\mathbb{I} - |\psi^+\rangle\langle\psi^+|) + f|\psi^+\rangle\langle\psi^+|, \quad (4.31)$$

⁸See <http://octave.sourceforge.net/optim/>.

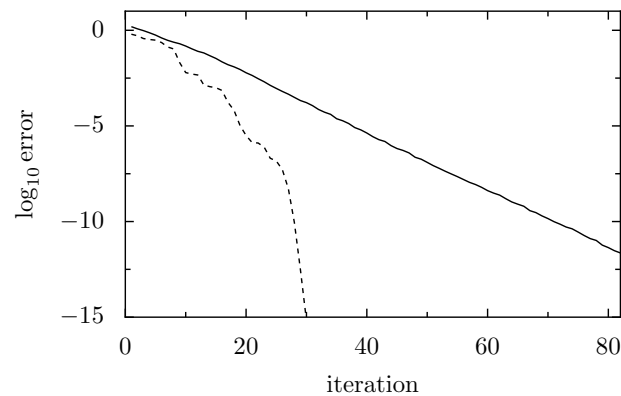


Figure 4.1: Comparison of numerical experiments with theory. The solid line demonstrates the convergence of the entanglement of formation of an isotropic state (example in Sec. 4.5), whereas the dashed line does the same for the tangle of a GHZ/W mixture (example in Sec. 4.5).

where $|\psi^+\rangle = \frac{1}{\sqrt{d}} \sum_{i=1}^d |ii\rangle$. An analytical solution for the entanglement of formation as a function of f and d has been found [TV00] and is implemented in `eofIsotropic`. Let us compare now the numerical results with theory. The full example can be found in the folder `examples/eofIsotropic`, along with all other related files.

We first choose a dimension for the two subsystems,

```
d = 5;
```

then create the maximally entangled state $|\psi^+\rangle$ in these systems and store it in `psi`:

```
psi = 0;
```

```
for i = 1:d
```

```
    tmp = zeros(d, 1);
    tmp(i) = 1;
    psi = psi + kron(tmp, tmp);
```

```
end
```

```
psi = psi/sqrt(d);
```

After choosing a value for the mixing parameter f ,

```
f = 0.3;
```

we can construct the isotropic state specified by d and f as


```
% Note that in M-script, A' is the Hermitian
% conjugate of A.
rho = (1 - f)/(d^2 - 1)*( eye(d^2) - ...
      (psi*psi') ) + f*(psi*psi');
```

and calculate its eigendecomposition with

```
[chi, lambda] = densityEig(rho);
```

In order to keep this example fully reproducible, we unfortunately have to load and overwrite the eigenvectors `chi` from a file at this point. The reason is that the density matrix is degenerate, yielding different eigendecompositions for the degenerate subspace depending on whether one uses `MATLAB` or `OCTAVE` due to the different diagonalization routines employed by these platforms. Clearly, one arrives at comparable results in both cases, but the paths in optimization space are different.

```
chi = load('example_eofIsotropic_chi.txt');
```

After setting an appropriate cardinality

```
r = rank(rho);
k = 2*r;
```

and defining function handles for the entanglement measure and its gradient

```
eoef = @(x) entropyOfEntanglement(x, [d, d]);
grad_eoef = ...
  @(x) grad_entropyOfEntanglement(x, [d, d]);
```

we can create the function handles required in the optimization

```
f_cr = @(x) convexSum(x, eoef, chi, lambda);
g_cr = @(x) grad_convexSum(x, eoef, ...
                          grad_eoef, chi, lambda);
```

Finally, we choose a random initial value `U0` (here initialized from a file)

```
U0r = load('example_eofIsotropic_U0r.txt');
U0i = load('example_eofIsotropic_U0i.txt');
U0 = U0r + 1i*U0i;
```

and perform the optimization:

```
[e_res, U_res, info] = cg_min(f_cr, g_cr, U0);
```

This yields a value of `e_res` $\approx 0.129322085695260$ after 80 iterations. We can check the convergence and the accuracy of the result by plotting the difference between the function value in each iteration and the theoretical value:

```
semilogy(abs(info.fvals - eofIsotropic(f, d)));
```

This produces the solid line in Fig. 1, showing that the result is exact up to an absolute error of $\approx 10^{-12}$.

Three-tangle of GHZ/W mixtures using `bfgs_min`

In this example, we will calculate the three-tangle of a mixture of the two states

$$|\text{GHZ}\rangle = (|000\rangle + |111\rangle)/\sqrt{2} \quad (4.32)$$

$$|\text{W}\rangle = (|001\rangle + |010\rangle + |100\rangle)/\sqrt{3}, \quad (4.33)$$

given by [LOSU06]

$$\rho_p = p|\text{GHZ}\rangle\langle\text{GHZ}| + (1 - p)|\text{W}\rangle\langle\text{W}|. \quad (4.34)$$

The example files are in `examples/tangleGHZW`.

In the code, we define the states

```
GHZ = [1; 0; 0; 0; 0; 0; 0; 0; 1]/sqrt(2);
```

```
W = [0; 1; 1; 0; 1; 0; 0; 0; 0]/sqrt(3);
```

choose a particular value for `p`

```
p = 0.7;
```

and create the mixed state

```
rho = p*GHZ*GHZ' + (1 - p)*W*W';
```

We then specify a value for the cardinality

```
r = rank(rho);
```

```
k = r + 4;
```

and can create the objective function and gradient handles. Note that we use the auxiliary function `createEHFunctions` to do all the required work:

```
[f_ah, g_ah] = createEHFunctions(rho, ...
                                k, r, @tangle, @grad_tangle);
```

After choosing a random initial point (initialized from a file, as before)

```
X0 = load('example_tangleGHZW_X0.dat');
```

we are ready to perform the optimization:

```
[t_res, X_res, info] = ...
    bfgs_min(f_ah, g_ah, X0);
```

The value one obtains in this way after 29 iterations is $t_{\text{res}} \approx 0.190667409058084$. A comparison with the analytical value [LOSU06] is exact within numerical precision. We can again plot the error between the function values and the exact result

```
semilogy(abs(info.fvals - tangleGHZW(0.7)));
```

which yields the dashed line in Fig. 1.

4.6 Conclusion

We have presented our library `libCreme` which serves to evaluate generic convex-roof entanglement measures. The library contains all tools required to deal with this problem, including two optimization algorithms working on the space of density matrix decompositions. The first one is based on a conjugate gradient algorithm operating directly on the group of unitary parameterizations, while the second one is a standard BFGS quasi-Newton method employed with a transformation from the original search space to unconstrained Euclidean space. Both implementations accept generic function handles, making it easy to extend their application to user-defined entanglement measures. All that needs to be done for this is the implementation of the respective pure-state entanglement monotone and the corresponding derivatives with respect to the real and imaginary parts of the input state vector.

Part II

**Self-Correcting Quantum
Memories**

Extending Kitaev's Toric Code with Long-Range Interactions

Adapted from:
S. Chesi, B. Röthlisberger, and D. Loss,
“Self-correcting quantum memory in a thermal environment”,
Phys. Rev. A **82**, 022305 (2010).

The ability to store information is of fundamental importance to any computer, be it classical or quantum. To identify systems for quantum memories which rely, analogously to classical memories, on passive error protection (‘self-correction’) is of greatest interest in quantum information science. While systems with topological ground states have been considered to be promising candidates, a large class of them was recently proven unstable against thermal fluctuations. In this chapter, we propose two-dimensional spin models unaffected by this result. Specifically, we introduce repulsive long-range interactions in the toric code and establish a memory lifetime polynomially increasing with the system size. This remarkable stability is shown to originate directly from the repulsive long-range nature of the interactions. We study the time dynamics of the quantum memory in terms of diffusing anyons and support our analytical results with extensive numerical simulations. Our findings demonstrate that self-correcting quantum memories can exist in 2D at finite temperatures.

5.1 Introduction

Quantum computers cannot be realized without the help of error correction [NC00]. By encoding quantum information into logical states

and designing correction circuits working on them, computations and information can in principle be protected from decoherence. However, the need for such an active control mechanism poses a major challenge for any physical implementation. It is therefore of greatest interest to look for passively protected systems which are intrinsically stable against the destructive influence of a thermal environment. For this reason, the idea to encode quantum information in a topologically ordered ground state $|\Psi_0\rangle$ of a suitable Hamiltonian has attracted a lot of interest [Kit03, DKLP02, Kit06, Bac06, TWT⁺07, TKPS10, VDS09, VTSD09, NO08, AFH09, IPGAP09, IPGAP10, BT09, KC08, PKSC09, PKSC10, HCC09, CLBT09].

Important candidates among such topological models are stabilizer Hamiltonians [NC00, Got97], which are given by a sum of mutually commuting many-body Pauli operators. The advantage of such Hamiltonians is that the full energy spectrum is known and error correction schemes are readily derived [NC00, Got97]. A prototypical example of such models is the toric code proposed in Ref. [Kit03], for which the stability against Hamiltonian perturbations [TWT⁺07, TKPS10, VDS09, VTSD09, PKSC10] and thermal fluctuations [DKLP02, NO08, AFH09, IPGAP09, IPGAP10] was studied extensively. However, recent results [BT09, KC08] show that in one and two spatial dimensions no stabilizer Hamiltonian with finite-range interactions (including the toric code model) can serve as a self-correcting quantum memory due to the errors induced by a thermal environment.

In other words, increasing the size of such a system does not prolong the protection of its ground-state space from decoherence. These negative results point toward the fundamental question whether topologically ordered quantum states, and hence self-correcting quantum memories, can exist at all on a macroscopic scale. In the following, we will demonstrate that self-correcting properties of two-dimensional (2D) stabilizer Hamiltonians can indeed be established when we allow for long-range repulsive interactions between the elementary excitations (anyons). While the purpose of the present work is of principal nature, we note that such interacting models can be expected to be realized in physical systems. We discuss this issue in greater detail at the end, where we also show how tunable repulsive long-range interactions could be mediated via photons in an optical cavity.

The outline of this chapter is as follows: In Sec. 5.2 we introduce a toric code model with repulsive long-range interactions between anyons. In Sec. 5.3 we describe how to simulate the dynamics of the model in contact with Ohmic or super-Ohmic thermal baths. A discussion of the decoherence caused by anyon diffusion and an expression of the memory lifetime as a function of system parameters is provided in Sec. 5.4. The main results of our work are in Secs. 5.5 and 5.6 where, first by an analytical mean-field treatment and then by direct numerical simulation,

we demonstrate the self-correcting properties of our model. Section 5.7 contains a discussion of the possible implementations of the long-range anyon interaction and Sec. 5.8 concludes the chapter with our final remarks.

5.2 Repulsive long range interactions in the Kitaev model

The model under study is defined on a $L \times L$ square lattice with periodic boundary conditions (a ‘torus’), and a spin- $\frac{1}{2}$ is placed on each of its $2L^2$ edges. Starting from the toric code model [Kit03], we consider the more general stabilizer Hamiltonian

$$H_0 = \frac{1}{2} \sum_{pp'} U_{pp'} n_p n_{p'} + \frac{1}{2} \sum_{ss'} V_{ss'} n_s n_{s'}, \quad (5.1)$$

where $n_p = (1 - \prod_{i \in p} \sigma_{z,i})/2$, $n_s = (1 - \prod_{i \in s} \sigma_{x,i})/2$, and $\sigma_{x,i}, \sigma_{z,i}$ denote the usual single-spin x and z Pauli operators applied to spin i . The indices p and p' run over all ‘plaquettes’ (involving the four spins on the edges of a unit cell), whereas s and s' run over all ‘stars’ (involving the four spins around a corner of a unit cell), see Fig. 5.1. The operator n_p (n_s) has eigenvalues 0, 1 and counts the number of plaquette- (star-) anyons at site p (s). The fourfold degenerate energy levels encode two qubits with logical operators given by $Z_i = \prod_{k \in \ell_i} \sigma_{z,k}$ and $X_i = \prod_{k \in \ell'_i} \sigma_{x,k}$, $i = 1, 2$, where ℓ_i and ℓ'_i are strings of spins topologically equivalent to single loops around the torus (see Fig. 5.1 for an example). These operators commute with all n_p and n_s and obey themselves the usual spin commutation relations.

Note that by specializing to $U_{pp'} = 2J\delta_{pp'}$ and $V_{ss'} = 2J\delta_{ss'}$, where $J > 0$ is the single-anyon excitation energy, the Kitaev original toric code model is recovered. Except for the boundary conditions, the structure of the toric code is very similar to an earlier model by Wegner [Weg71, Kog79]. Wegner’s Ising lattice gauge theory involves only plaquette operators in the Hamiltonian ($U_{pp'} = 2J\delta_{pp'}$ and $V_{ss'} = 0$), while the stars play the role of a gauge symmetry group. Both the Kitaev Hamiltonian and the two-dimensional Wegner model have no finite-temperature phase transition, as can be obtained by mapping them to one-dimensional Ising chains [Weg71, Kog79, DKLP02, NO08]. Finally, the Kitaev model is also equivalent to a model proposed later by Wen [Wen03, NO09].

Since all n_p and n_s are mutually commuting, the Hamiltonian Eq. (5.1) describes two independent lattice gases of plaquettes and stars, respectively. Without loss of generality, we can thus restrict our analysis to the dynamics of plaquettes and their influence on one of the Z_i operators, say $Z_1 \equiv Z$. A corresponding logical operator Z_{ec} is defined by the error correction procedure (see Fig. 5.1 and Sec. 5.3). Consequently, we set

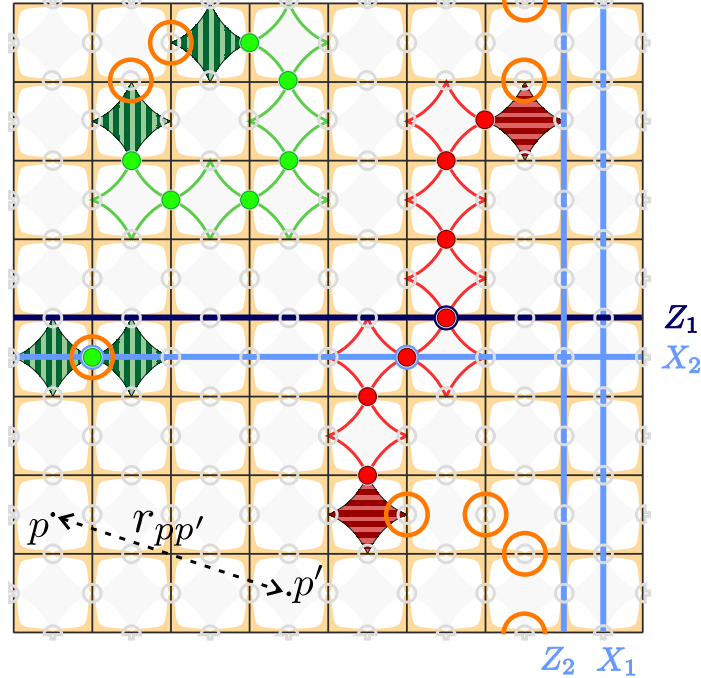


Figure 5.1: Quantum memory based on the toric code. Illustrated is an 8×8 lattice (periodic boundary conditions) with a total of 128 spins- $\frac{1}{2}$ [gray (smaller) circles] on its edges. The four-body plaquette and star operators are indicated in the background. A particular choice for all logical operators X_1 , Z_1 , X_2 , and Z_2 is shown, although we will focus only on the decay of $Z_1 \equiv Z$ (see main text). A number of spins is affected by σ_x -errors (solid dots), leading to excited plaquettes, or ‘plaquette anyons’ (striped plaquettes). Measuring the plaquette operators yields the positions of the excited plaquettes, but reveals no information about how they were originally paired or which path (indicated by the framed plaquettes) they took. A minimum-weight error correction procedure (see Sec. 5.3) applies σ_x -operators to the spins marked by the larger orange circles. While the vertically striped green anyons are annihilated ‘properly’ (with a trivial loop of errors remaining from the top pair and no error from the bottom pair), the horizontally striped red pair is connected around a topologically non-trivial loop on the torus. Although this last pair is annihilated as well, an uncorrected σ_x -error remains on the logical Z string, having thereby introduced a logical error in the state stored in the memory.

$V_{ss'} = 0$ for all stars while assuming the plaquette interactions $U_{pp'}$ to be of the generic form

$$U_{pp'} = 2J\delta_{pp'} + \frac{A}{(r_{pp'})^\alpha}(1 - \delta_{pp'}), \quad (5.2)$$

where $r_{pp'}$ denotes the shortest distance on the torus between the centers of plaquettes p and p' , see Fig. 5.1. The strength of the repulsive plaquette interaction is given by the energy $A \geq 0$, and the interaction is long-range for $0 \leq \alpha < 2$ (see below). The model is also equivalent to a long-range Ising model, see Appendix D.1. The case of a positive logarithmically diverging interaction (which results in attractive forces between the anyons [DKLP02]) was recently discussed in Ref. [HCC09].

5.3 Error models and simulations

Error models

We model the interaction of the system with a thermal environment by coupling each spin to a bath which can introduce σ_x -errors [¹] in the initial state $|\Psi_0\rangle$, assumed to be a ground state of Eq. (5.1). From a standard master equation approach in the weak coupling limit [Dav74, AFH09], we derive a rate equation for the probabilities p_m of the system to be in state $|\Psi_m\rangle = \prod_{i \in m} \sigma_{x,i} |\Psi_0\rangle$, where $\{m\}$ is the set of all possible patterns of σ_x -errors. This rate equation reads

$$\dot{p}_m = \sum_i [\gamma(-\omega_i(m))p_{x_i(m)} - \gamma(\omega_i(m))p_m], \quad (5.3)$$

where we have defined $x_i(m)$ to be the state m with an additional σ_x -error applied to spin i , and $\omega_i(m) = \epsilon_m - \epsilon_{x_i(m)}$ is the energy difference between the states m and $x_i(m)$. The time evolution of the probabilities p_m determines the decay of the expectation values $\langle Z_{(\text{ec})} \rangle = \sum_m p_m \langle \Psi_m | Z_{(\text{ec})} | \Psi_m \rangle$.

The rates $\gamma(\omega)$ describe the transition probabilities between states with energy difference ω . A standard expression for $\gamma(\omega)$ can be obtained from a spin-boson model and reads [LCD⁺87, DL05]

$$\gamma(\omega) = 2\kappa_n \left| \frac{\omega^n}{1 - e^{-\beta\omega}} \right| e^{-|\omega|/\omega_c}. \quad (5.4)$$

Here, $\beta = 1/T$, with T being the temperature of the bath (we set Boltzmann's constant to one). For simplicity, we assume in the following a large cut-off energy $\omega_c \rightarrow \infty$. For $n = 1$, the bath is called 'Ohmic', whereas for $n \geq 2$ it is called 'super-Ohmic'. We find in this work that n

¹ σ_z -errors are irrelevant for the dynamics of plaquettes.

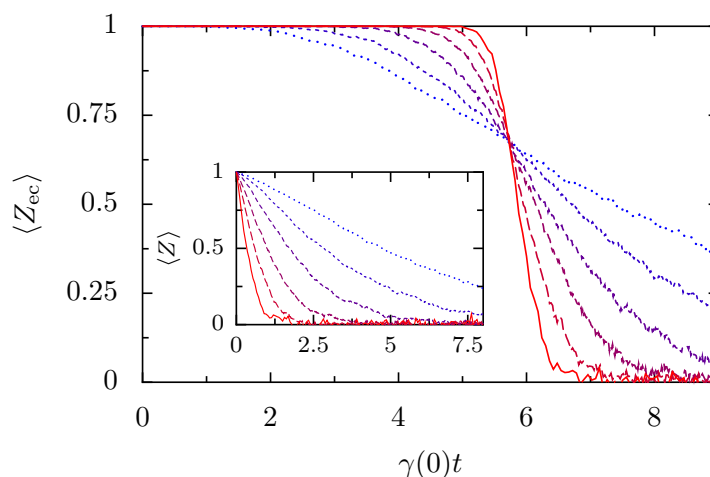


Figure 5.2: Decay of the logical Z operator in the non-interacting toric code. The simulation data is obtained for grid sizes L increasing by powers of two from 16 (dotted blue) to 512 (solid red). All curves are ensemble averages over 10^4 runs. The main plot displays $\langle Z_{ec} \rangle$, which is the average value of Z one would find if an error correction scheme would be applied at the readout time t . The inset shows the expectation value of the bare (uncorrected) logical Z operator. We have used $T/J = 0.3$, and $\gamma(0) = \gamma(2J)$. See Sec. 5.3 for further details on the simulation.

has a strong influence on the decay times of the encoded states, with super-Ohmic baths providing the best scaling of the memory lifetime with L . These are not uncommon and emerge, e.g., for quantum dot spins in contact with phonons [GKL04].

Simulations and error correction

The eigenstates of Eq. (5.1) are highly entangled, but it is nevertheless possible to perform classical simulations of the quantum memory in the simple framework discussed above. In order to achieve a time evolution in accordance with Eq. (5.3), each iteration of a simulation consists of the following steps. (i) We record the relevant parameters of the system. (ii) We calculate the total spin flip rate $R = \sum_i \gamma(\epsilon_s - \epsilon_{x_i(s)})$, where s is the current state of the system. (iii) We draw the time Δt it takes for the next spin to flip from an exponential distribution, $\Delta t \sim \text{Exp}(1/R)$, and then add this to the current total time. (iv) We calculate all individual spin flip probabilities $p_i = \gamma(\epsilon_s - \epsilon_{x_i(s)})/R$ and flip a spin at random accordingly. After some initially specified time has been reached, we stop and have obtained a single ‘run’. The final data presented in this work is then generated by averaging over many (typically several thousand) runs.

Although continuous monitoring and error-correction are not required

in a passive memory during the storage time, it is still beneficial to apply an error correction scheme once the memory is being read out. By $\langle Z_{ec} \rangle(t)$, we denote in this work the average value of Z we would have obtained if we had performed error correction at time t . The goal here is to properly annihilate corresponding anyons (by applying σ_x -operations), thereby reverting the undesired operations performed by anyon paths crossing the logical operator strings. However, since only the positions of the anyons are known, this correspondence has to be guessed. We do this by choosing the pairing with the minimal sum of connection path lengths using Blossom V [Kol09], which is the latest improvement on Edmonds' minimal-weight perfect matching algorithm [Edm65]. If many anyons are present, using the complete graph as the input to this algorithm is numerically infeasible. In excellent approximation, we therefore replace the complete graph by a Delaunay triangulation [2].

As a useful reference, we show in Fig. 5.2 numerical results for the non-interacting system, i.e., $A = 0$. The relevant rates entering Eq. (5.3) are $\gamma(0)$ (rate for an anyon to hop to a free neighboring site), $\gamma(-2J)$ (rate to create an anyon pair) and $\gamma(2J) = \gamma(-2J)e^{2J\beta}$ (rate to annihilate a pair of adjacent anyons, obtained from the detailed balance condition). Figure 5.2 illustrates the typical behavior of $\langle Z \rangle$ and $\langle Z_{ec} \rangle$, in agreement with previous literature [AFH09, NO08, HCC09, BT09, KC08]. We refer to Sec. 5.4 for a more detailed discussion.

5.4 Diffusion of anyons and memory lifetime

It is the purpose of this section to establish a formula for the lifetime of the quantum memory. A static criterion was discussed in Ref. [DKLP02]: assuming independent errors, the toric code can be mapped to a random-bond Ising model, and a threshold probability $f_c = 0.11$ is obtained. In the thermodynamic limit, retrieval of the encoded information is impossible if the relative number of errors is above this value. Below f_c , recovery is achieved with probability one. Numerically, we find a similar threshold $f_c \approx 0.1$ for the same error model, see Fig. 5.3. This shows that our implementation of the minimum-weight error correction scheme works close to optimal.

Also in the dynamical simulations of the non-interacting model (see Fig. 5.2), we observe a sharp transition in time similar to Fig. 5.3. Starting from an initial state without errors, the thermal environment introduces a growing number of spin-flips which eventually cause the memory to fail. This occurs again at a certain threshold probability f_c which is for this case, however, different from 0.1, see the inset of Fig. 5.3. To understand this difference, we note that a main mechanism for the creation of

²We have used the code `Triangle` [She96]. See also Ref. [Kol09] and references therein for a justification of this approximation.

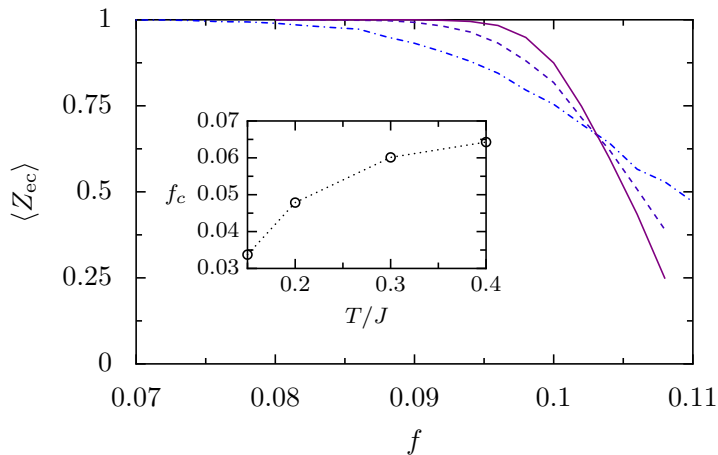


Figure 5.3: Average of the corrected operator Z_{ec} for a model with independent σ_x -errors occurring with probability f at each spin. The dashed-dotted, dashed, and solid curves refer to our numerical simulations with lattice sizes $L = 40, 100, 200$, respectively. The error correction fails at a value $f_c \simeq 0.1$, which is slightly smaller than the value 0.11 from Ref. [DKLP02]. In the inset, we plot the value of f_c from simulations of the non-interacting toric code in contact with a bath at temperature T and $\gamma(0) = \gamma(2J)$. The fraction f_c is extracted at the time τ when $\langle Z_{ec} \rangle$ decays to zero in the limit of large L (see Fig. 5.2). This value is always smaller than $f = 0.11$ and depends on T .

errors is the diffusion of anyons. Clearly, errors created by the anyons in their diffusive motion have strong spatial correlations, rather than being independent and uniformly distributed across the memory. We find that such correlations yield values of f_c strictly smaller than 0.1 but still of the order of a few percent, see Fig. 5.3. Although the value of f_c is difficult to determine in general, we will assume in the following that such threshold probability exists and derive from it an expression for the memory lifetime.

Direct and indirect diffusion of anyons

To estimate the error creation rate, we first study the diffusive motion of anyons in the non-interacting model. To determine the diffusion constant D , we consider an isolated anyon in the lattice and its probability $p_{i,j}$ to be at site (i, j) . In the Ohmic case, we have $\gamma(0) \neq 0$, and direct hopping to neighboring sites is thus allowed. In the continuum limit, a standard diffusion equation $\frac{dp(\mathbf{r})}{dt} = D\nabla^2 p(\mathbf{r})$ with $D = \gamma(0)$ is obtained. The resulting decay of the bare and error-corrected logical operators in the simple case of a single pair is discussed in Appendix D.2.

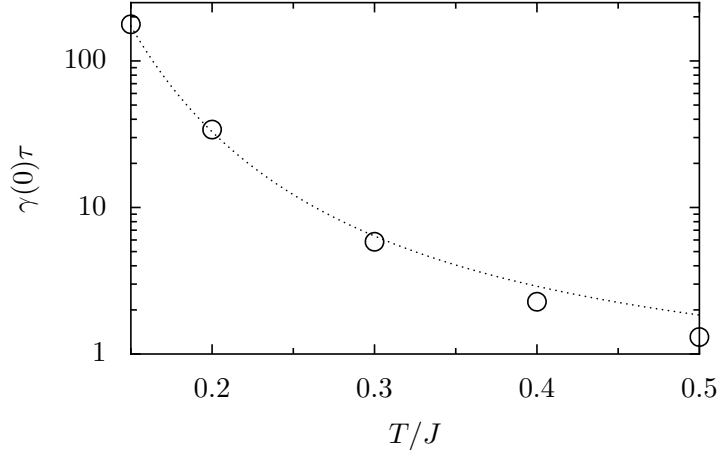


Figure 5.4: The values of τ extracted at the sharp transitions of the $\langle Z_{ec} \rangle$ decay (circles). As in Fig. 5.2, we use $\gamma(0) = \gamma(2J)$. Comparison to Eq. (5.5) (dotted curve) gives good agreement for $f_c \simeq 0.1$.

For a super-Ohmic bath where $\gamma(0) = 0$, diffusion is still possible due to ‘indirect hopping’. We assume $2\beta J \gg 1$, such that, since $\gamma(2J) = e^{2\beta J} \gamma(-2J)$, the recombination of a pair of anyons is essentially instantaneous. Hopping from the site (i, j) to, e.g., $(i, j+2)$ is possible by creation of an anyon pair occupying sites $(i, j+1)$ and $(i, j+2)$. This event occurs with rate $\gamma(-2J)$. Since the intermediate state can decay back to the initial state, the actual rate for the indirect hopping process is $\gamma(-2J)/2$. Similar considerations hold for all other sites. Accounting for all of these, we write

$$\begin{aligned} \frac{dp_{i,j}}{dt} = & \frac{\gamma(-2J)}{2} (-12p_{i,j} + p_{i+2,j} + p_{i-2,j} + p_{i,j+2} + p_{i,j-2} \\ & + 2p_{i+1,j+1} + 2p_{i+1,j-1} + 2p_{i-1,j+1} + 2p_{i-1,j-1}), \end{aligned}$$

which, in the continuum limit, yields $D = 4\gamma(-2J)$. We can expect that the properties of the memory improve by lowering the value of $\gamma(0)$, but only as long as $\gamma(0) \gtrsim 4\gamma(-2J)$. In the interacting case, J can be replaced by an appropriate excitation energy (e.g., a mean-field gap, see Sec. 5.5).

Lifetime of the non-interacting model

We can now express the error creation rate in terms of the diffusion constant. An isolated anyon can have either one or three σ_x -errors at its plaquette spins. In the first case, the anyon can hop to a neighboring site either by creating an error on one of the initially unaffected spins, or by removing the one pre-existing error. Therefore, such an anyon contributes to the error rate with $2D = 3D - D$. If three σ_x -errors are present,

an opposite rate $-2D$ is obtained from an analogous reasoning. However, three-error plaquettes can be expected to be less likely: they require that an anyon hopped on a plaquette with two pre-existing errors from one of the two directions without errors. From the above discussion, it is justified to estimate the rate at which errors are created to be of order D per anyon.

Finally, assuming N diffusing anyons present in the system, the fraction f of spins affected by a σ_x -error after a time t is estimated as $f \simeq NDt/2L^2$ and the error correction fails when f is larger than some critical value f_c [DKLP02]. This gives a lifetime τ for the memory

$$\tau \simeq 2f_c \frac{e^{\beta J} + 1}{\max\{\gamma(0), 4\gamma(-2J)\}}, \quad (5.5)$$

where we have replaced the factor N/L^2 by the equilibrium occupation $\langle n_p \rangle = 1/(e^{\beta J} + 1)$.

An analogous result can be obtained based on the following different reasoning [AFH09, HCC09]. The distance between the two anyons of a pair after a time τ is of order $\Delta\ell = \sqrt{D\tau}$ and is required to be much smaller than the average anyon separation $\sim \sqrt{L^2/N}$. This gives $\tau \ll (e^{\beta J} + 1)/\max\{\gamma(0), 4\gamma(-2J)\}$. Interestingly, this upper bound coincides with the right-hand side of Eq. (5.5) if the probability for each spin to be flipped is $\frac{1}{2}$ (which is realized at long times).

Equation (5.5) generally gives reasonable estimates of the memory lifetime. For example, the value $f_c \simeq 0.11$ of [DKLP02] yields $\tau \simeq 5.8$ for the same parameters as used in Fig. 5.2, in remarkable agreement with the simulations. However, the real threshold directly obtained by the simulation is smaller (inset of Fig. 5.2). This seems not surprising considering the approximations introduced when deriving Eq. (5.5). We generally adopt the practice of using f_c as a single fitting parameter to study the functional dependence of the lifetime, e.g., as a function of L or T . An example of the temperature dependence of τ in the non-interacting case is shown in Fig. 5.4 and is also well described by Eq. (5.5).

More importantly, Eq. (5.5) allows one to describe the asymptotic dependence of the lifetime on L . For the non-interacting case, τ is independent of the system size, consistent with previous findings [AFH09, NO08, HCC09, BT09, KC08]. This fact is confirmed by our simulations, as shown in Fig. 5.2, where $\langle Z_{ec} \rangle$ clearly approaches a step-function with increasing L . We also see that the bare expectation value $\langle Z \rangle$ decays even faster with larger L . Indeed, at sufficiently short times $t \ll 1/\max\{\gamma(0), 4\gamma(-2J)\}$, when anyon pairs have not yet diffused apart from each other (the 'nonsplit-pair' regime, indicated by an asterisk), we obtain $\langle Z \rangle = (1-1/L)^{N^*/2} \simeq e^{-N^*/2L}$. By using $N^* \simeq 4L^2\gamma(-2J)t$, it follows that $\langle Z \rangle$ decays exponentially with L .

For the interacting case, we find good agreement of a modified version of Eq. (5.5) with the simulations [see Eq. (5.12) and Fig. 5.6]. Fitting

the data always yields values of f_c smaller than $f_c = 0.11$, but still of the order of a few percent. These values are thus consistent with the original meaning of f_c . For a more extended discussion, we refer to Secs. 5.5 and 5.6.

5.5 Mean-field analysis of the interacting model

We now turn to the interacting case $A > 0$ and perform a mean-field analysis, which becomes accurate in the relevant limit of large L .

Mean-field anyon density

We first consider the equilibrium number of anyons N within a mean-field treatment (mean-field values will be indexed with a subscript 'mf'). We obtain the single-particle energy at plaquette p as $\epsilon_p = \delta H_0 / \delta n_p = J + \sum_{p' \neq p} U_{pp'} n_{p'}$. Replacing $n_{p'}$ by the average value $n_{\text{mf}} = N_{\text{mf}} / L^2$ and taking the continuum limit, we find the mean-field value for ϵ_p to be

$$\epsilon_{\text{mf}} = J + n_{\text{mf}} \int_{L \times L} \frac{A}{r^\alpha} d\mathbf{r} = J + n_{\text{mf}} T L_\alpha, \quad (5.6)$$

where we use the notation

$$L_\alpha = c_\alpha \beta A L^{2-\alpha}. \quad (5.7)$$

The constant c_α is a geometrical factor of order 1, given by the integration of $1/r^\alpha$ on a unit square centered at the origin. In particular, $c_0 = 1$. On the other hand, we have $n_{\text{mf}} = 1/(e^{\beta \epsilon_{\text{mf}}} + 1)$ since the occupation numbers n_p can only assume the values 0 or 1. By using Eq. (5.6) to calculate n_{mf} , we find the self-consistent equation

$$n_{\text{mf}} = \frac{1}{e^{\beta J + n_{\text{mf}} L_\alpha} + 1}, \quad (5.8)$$

with the following expansion at large L_α

$$n_{\text{mf}} = \frac{1}{L_\alpha} [\ln L_\alpha - \ln \ln L_\alpha - \beta J + \dots]. \quad (5.9)$$

Higher order terms in the square brackets are small if $\ln L_\alpha \gg \beta J, |\ln \ln L_\alpha|$. For fixed temperature T and interaction strength A , these conditions are always satisfied at sufficiently large L since $L_\alpha \propto L^{2-\alpha}$.

We have confirmed the validity of the mean-field approximation by Monte Carlo simulations. By using the Metropolis algorithm [MRR⁺53] to sample the probability distribution $\propto e^{-\beta/2 \sum_{p,p'} U_{pp'} n_p n_{p'}}$, see Eq. (5.1),

the equilibrium number of excited plaquettes can be approximated with arbitrary accuracy. This can be used to study the accuracy of the mean-field value $N_{\text{mf}} = n_{\text{mf}}L^2$ [see Eq. (5.8)], in particular for values $\alpha \neq 0$. Due to the long-range nature of the interaction, N_{mf} compares very well to the equilibrium value of N obtained from these simulations at generic values of the temperature and interaction exponent α . This is illustrated in Fig. 5.5, which further shows a satisfactory agreement already at moderate values of L .

We also note that, for the case of constant interaction ($\alpha = 0$), the average number can be calculated directly from the grand-canonical partition function

$$\sum_{2k \leq L^2} \binom{L^2}{2k} e^{-\beta E_{2k}}, \quad (5.10)$$

since the energy of a given anyon configuration does not depend on the positions of the anyons, but only on their total number $N = \sum_p n_p$. In the presence of a sufficiently strong anyon interaction or at low temperature, the number of excited plaquettes is much smaller than L^2 . Therefore, one can restrict the sum (5.10) to the first few relevant terms.

Lifetime of the interacting model

From Eq. (5.9) we obtain that, even though the number of anyons N_{mf} grows with the system size L , the anyon density n_{mf} goes to zero for long-range repulsive interactions with $0 \leq \alpha < 2$. Hence, the population of anyons is increasingly diluted and the system is essentially frozen in the ground state at large system size. This remarkable effect can be attributed to the divergence of the excitation energy $\epsilon_{\text{mf}} \simeq T \ln L_\alpha$, which is self-consistently determined from the anyon population in the *whole* system due to the long-range nature of the interactions. Note also that, despite the fact that ϵ_{mf} is diverging, the total excitation energy density $n_{\text{mf}}\epsilon_{\text{mf}}/2$ goes to zero for large L .

Secondly, the divergence of ϵ_{mf} leads to a vanishing anyon pair creation rate at large L ,

$$\gamma(-2\epsilon_{\text{mf}}) \simeq \kappa_n T^n \frac{(2 \ln L_\alpha)^{n+2}}{2L_\alpha^2}. \quad (5.11)$$

This fact allows us to revise the lifetime for the non-interacting memory Eq. (5.5), simply by substituting J with the equilibrium value ϵ_{mf} , yielding

$$\tau \simeq \frac{2f_c/n_{\text{mf}}}{\max\{\gamma(0), 4\gamma(-2\epsilon_{\text{mf}})\}}. \quad (5.12)$$

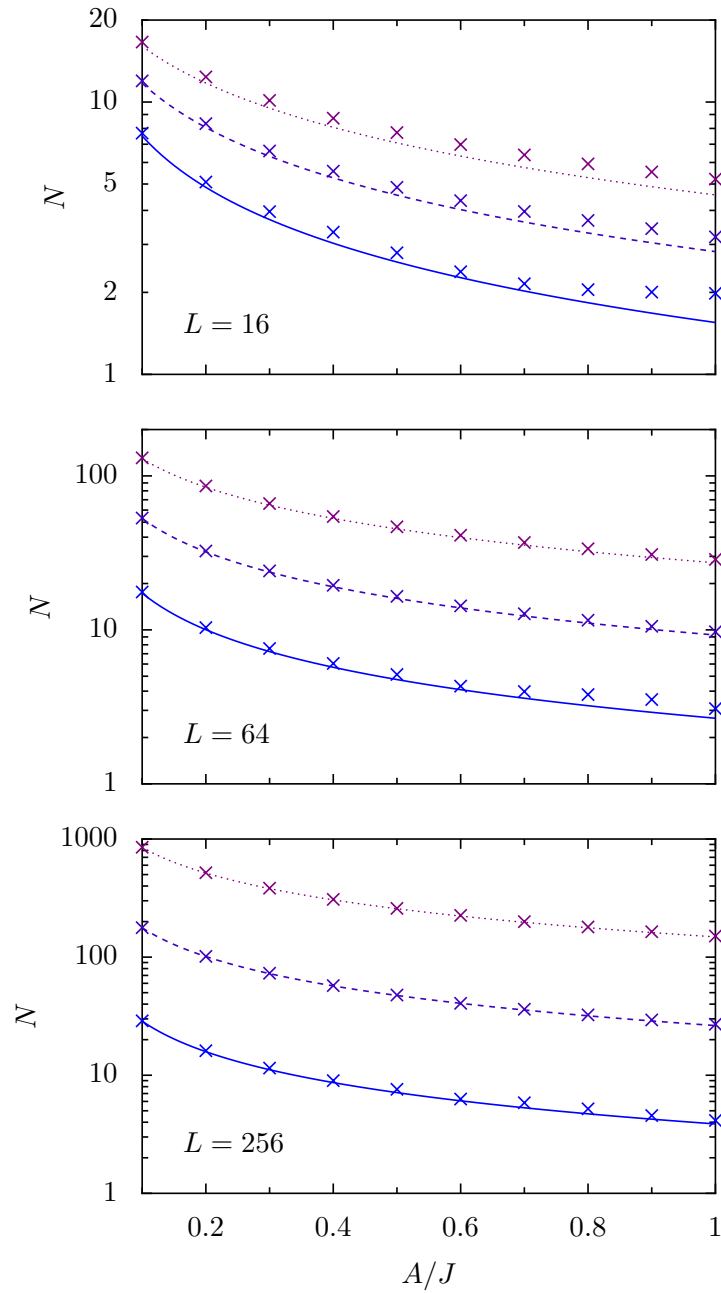


Figure 5.5: Comparison of the equilibrium value of N obtained numerically (crosses) with N_{mf} (curves) for different grid sizes. We have used the interaction exponents $\alpha = 0$ (solid line), $\alpha = 0.5$ (dashed line), and $\alpha = 1.0$ (dotted line), and the temperature $T/J = 0.5$.

From this we obtain the lifetime of an interacting memory in case of an Ohmic ($n = 1$) or super-Ohmic ($n > 1$) bath as

$$\tau \simeq \begin{cases} \frac{f_c L_\alpha}{\kappa_1 T \ln L_\alpha}, & \text{Ohmic} \\ \frac{2f_c L_\alpha^3}{\kappa_n T^n (2 \ln L_\alpha)^{n+3}}, & \text{super-Ohmic} \end{cases} \quad (5.13)$$

in the limit of large grid size [see after Eq. (5.9)]. It is clear from these expressions that the memory lifetime is diverging with L , in strong contrast to the non-interacting case where it was bounded by a constant. In the Ohmic case, this divergence of τ is entirely due to the vanishing density, since $\gamma(0) = 2\kappa_1 T$ is non-zero. In the super-Ohmic case, however, an additional divergence due to the vanishing of $\gamma(-2\epsilon_{\text{mf}})$ is obtained, see Eq. (5.11). Since the energy gap grows logarithmically with L , τ grows polynomially, but with a rather favorable power. For instance, constant interaction ($\alpha = 0$, see also below) leads to $\tau \propto L^2 / \ln L$ in the Ohmic case and to $\tau \propto L^6 / \ln^5 L$ in the super-Ohmic ($n = 2$) case.

Effects beyond the mean-field treatment

Equation (5.12) is valid in the mean-field limit and does not include effects of the fluctuations of the number of anyons and their positions. These result in additional errors and correlated spin-flips across the memory, due to the long-range nature of the anyon interactions. Although we expect in general deviations from Eq. (5.12), the memory remains self-correcting both for an Ohmic and for a super-Ohmic bath.

Indeed, for an Ohmic bath, we can neglect the effect of the repulsive force if the change of energy ω in a diffusive step is smaller in magnitude than T [see Eq. (5.4)], so that we can approximate $\gamma(\omega) \simeq \gamma(0)$. In particular, for a single pair of anyons at distance r , we have $|\omega| \lesssim \alpha A / r^{\alpha+1}$, which defines a critical radius

$$r_c = (\alpha A \beta)^{\frac{1}{\alpha+1}}, \quad (5.14)$$

beyond which the fluctuations become negligible. For $\alpha = 0$ one has $r_c = 0$. For $\alpha > 0$, since the average distance $\sim 1/\sqrt{n_{\text{mf}}}$ between anyons grows with L while r_c is independent of L , the fluctuations also become negligible. The validity of Eq. (5.12) for the Ohmic case is confirmed by numerical simulations both for $\alpha = 0$ (see Fig. 5.6) and for $\alpha > 0$ (see Fig. 5.8).

Concerning the super-Ohmic case, Eq. (5.12) could become inaccurate if the fluctuations of $\omega \simeq 0$ are more effective for the anyon motion than the indirect diffusion mechanism which is proportional to the rate in Eq. (5.11). However, due to the decreasing interaction strength,

such fluctuations in ω become small at large L and still result in a vanishing diffusion coefficient. Therefore, Eq. (5.12) might overestimate the lifetime in this case, but the asymptotic dependence on L would still be better than in the Ohmic case. Furthermore, at $\alpha = 0$ direct hopping is impossible and Eq. (5.12) is valid (see Fig. 5.6).

5.6 Dynamics of the interacting model

We turn now to the numerical simulations of our model, Eq. (5.1), and focus first on constant long-range interactions ($\alpha = 0$). In this case, the total energy $E_N = NJ + \frac{A}{2}N(N-1)$ depends only on the number of anyons N , but not on their position. This simplifies the numerical treatment considerably. Our results are displayed in Fig. 5.6. The numerical data show a clear increase of the memory lifetime τ with L . Note that this holds already for the *bare* logical Z operator. Like in the non-interacting case (see Fig. 5.2), the beneficial effect of the error correction at read-out is to prolong the lifetime by maintaining $\langle Z_{ec} \rangle$ close to 1 (see inset of Fig. 5.6).

Our analytical results describe the numerical data remarkably well. By fitting f_c in Eq. (5.12) to the simulation data, excellent agreement is found for an Ohmic bath (top panel of Fig. 5.6), while for a super-Ohmic bath (lower panel), analytics and numerics agree well for $L \gtrsim 64$. Furthermore, the fit yields values for f_c of about 0.01 – 0.02, which is reasonable in comparison to the upper bound $f_c = 0.11$ found for a model of uncorrelated errors (dashed-dotted lines in Fig. 5.6) [DKLP02]. See also the discussion in Sec. 5.4.

The lifetime τ can be compared to the physical time scales of single spin flips, $1/\gamma(0)$ and $1/\gamma(-2J)$. For instance, for the $L = 256$ super-Ohmic case in Fig. 3 we obtain $\tau\gamma(-2J) \simeq 5 \times 10^5$, i.e., already for a moderate system size the lifetime τ of the memory is about a 10^6 times longer than the single-spin lifetime. For quantum dots, the latter is typically in the range of milliseconds to seconds at about 100 mK [GKL04, AMR⁺08].

The nonsplit pair regime

We consider now in greater detail the super-Ohmic case at $\alpha = 0$, which has the most favorable scaling. The initial dynamics of the memory can be nicely characterized by a regime of nonsplit pairs. Under this assumption, the rate equation

$$\frac{dN_{mf}^*}{dt} = 4L^2\gamma(-2\epsilon_{mf}^*) - N_{mf}^*\gamma(2\epsilon_{mf}^*) \quad (5.15)$$

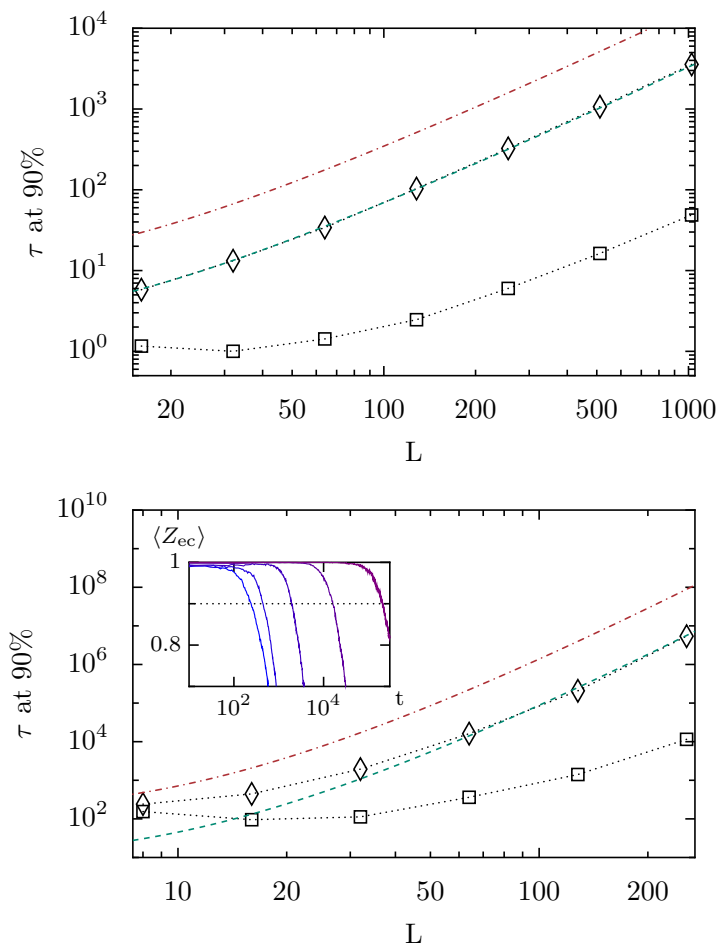


Figure 5.6: Thermal stability of the interacting memory. The data in the top (bottom) panel were obtained for an Ohmic (super-Ohmic, $n = 2$) bath. Plotted as a function of L are the numerically simulated times at which the expectation values of the bare (squares) and error-corrected (diamonds) logical Z operator have decayed from 1 to 0.9. The dotted lines serve as a guide to the eye. The red dashed-dotted curves are calculated from Eq. (5.12) with $f_c = 0.11$, where we have used the self-consistent values of n_{mf} and ϵ_{mf} from Eqs. (5.6) and (5.8). Similarly, the green dashed lines are also due to Eq. (5.12), but here f_c is fit to the numerical data of the 90% threshold times, yielding $f_c = 0.022$ for an Ohmic, and $f_c = 0.007$ for a super-Ohmic bath. The inset shows the decay of $\langle Z_{ec} \rangle$ with time for $L = 8, \dots, 128$ (from left to right), and the 90% threshold is illustrated by the dotted line. It is seen that choosing this particular value has no substantial influence on the scaling behavior with L . Parameters used in these simulations were $A/J = 0.1$, and $T/J = 0.3$. Times are in units of $(\kappa_1 J)^{-1}$ and $(\kappa_2 J^2)^{-1}$ for the first and second panel, respectively.

describes the initial time-evolution of the system well, since in this non-diffusive regime only pair creation [3] and annihilation takes place. In Eq. (5.15) we denote with N_{mf}^* the total number of anyons, appearing as $N_{\text{mf}}^*/2$ nonsplit pairs.

We confirm Eq. (5.15) by comparing its solution, obtained by numerical integration, with a direct simulation presented in Fig. 5.7. After a rapid initial ‘build-up’ phase, N_{mf}^* saturates to a value determined by the self-consistent condition $N_{\text{mf}}^* = 4L^2 e^{-2(J+AN_{\text{mf}}^*)\beta}$, obtained by setting $dN_{\text{mf}}^*/dt = 0$ in Eq. (5.15). In this state, the excitation energy is diverging with L , since we have $\epsilon_{\text{mf}}^* \simeq AN_{\text{mf}}^* \simeq AN_{\text{mf}}/2 \propto \ln L$. This effectively suppresses the indirect diffusion of anyons. Therefore, the system remains in a quasi-stationary state which evolves to the final anyon density on a time scale also diverging with L . In this regime of nonsplit pairs, one has $\langle Z \rangle \simeq e^{-N_{\text{mf}}^*/2L}$. This leads to the quasi-stationary value $\langle Z \rangle \simeq e^{-\frac{\ln L}{2\beta AL}}$, which approaches 1 for large L (see Fig. 5.7).

Similar to the calculation of the total number of anyons [see Eq. (5.10)], the exact quasi-stationary number of paired anyons N^* (crosses in Fig. 5.7) can be calculated from a partition function reading

$$\sum_{k \leq 2L^2} \binom{2L^2}{k} e^{-\beta E_{2k}}. \quad (5.16)$$

Here we have assumed that k sufficiently diluted errors are present in the memory such that $2k$ anyons are created in the nonsplit-pair regime. The average number of anyons N^* calculated from Eq. (5.16) is in very good agreement with the simulations, see Fig. 5.7.

Non-constant interaction

For non-constant long-range interaction ($0 < \alpha < 2$), simulating the time dynamics of the memory is numerically more costly due to an $O(L^2)$ overhead coming from recalculating all spin flip rates. Nevertheless, we were able to study the (more tractable) case of an Ohmic bath. The results are presented in Fig. 5.8 for $\alpha = 0.5$ and $\alpha = 1$. Clearly, the memory lifetime is still increasing with L , proving the memory to be self-correcting also for $\alpha \neq 0$. Furthermore, the data are in very good agreement with the analytically calculated lifetime Eq. (5.12). The super-Ohmic case for $\alpha > 0$ is more difficult to simulate due to the increased memory lifetime and will be examined elsewhere.

³Note that in Eq. 5.15, we have approximated the number of spins without errors by the total number $2L^2$, neglecting corrections of order $\ln L$.

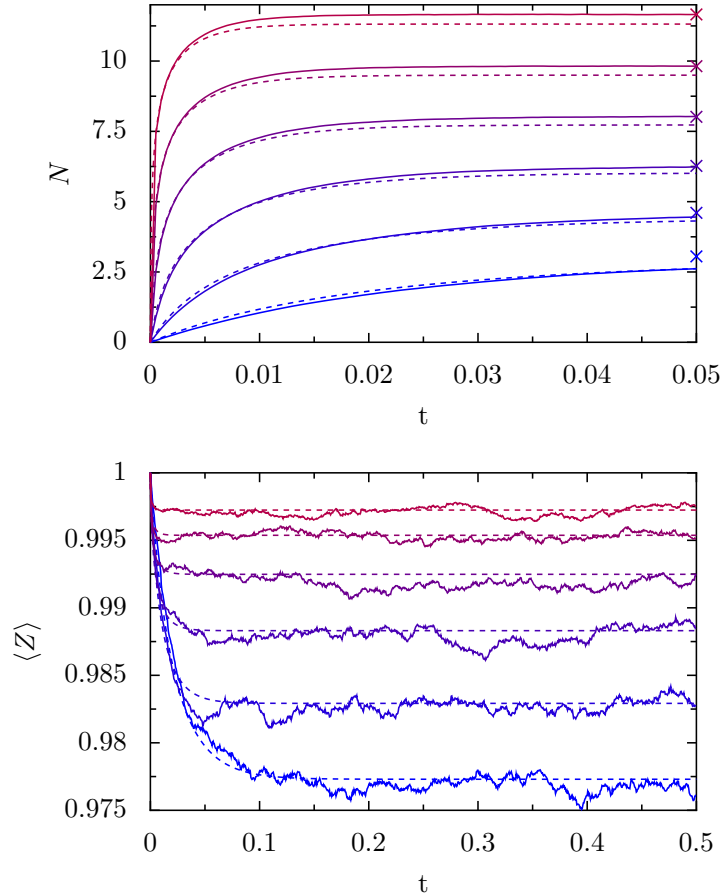


Figure 5.7: Short-time dynamics of the interacting memory in a super-Ohmic bath. In this case, the memory is in the nonsplit-pair regime. The curves refer to different values of L increasing in powers of 2 from $L = 64$ (lowest curves in both panels) to $L = 2048$ (highest curves). Upper panel: The time dependence of the anyon number N obtained from the simulations (solid lines) is compared to the solutions of Eq. (5.15) (dashed lines). The crosses are the exact values N^* obtained from the partition function of pairs Eq. (5.16). Good agreement with N^* is also obtained for the lower curves at longer times (not shown). Lower panel: The expectation value of the bare Z obtained from the simulations (solid lines) is compared to $e^{-N^*/2L}$ (dashed lines), where $N^*(t)$ is obtained from the upper plot. Parameters used are $A/J = 0.1$, and $T/J = 0.3$. The time axes are in units of $(\kappa_2 J^2)^{-1}$.

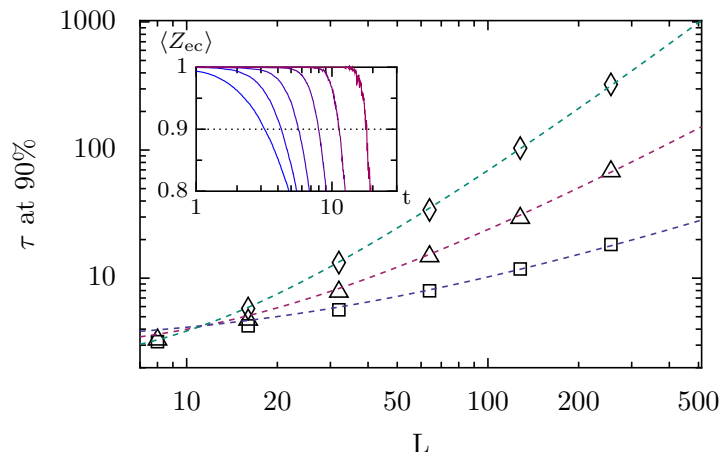


Figure 5.8: Thermal stability of the interacting memory with $\alpha \neq 0$ and an Ohmic bath. Data points refer to the numerically calculated times at which the error-corrected logical Z operator has decayed from 1 to 0.9 in the cases $\alpha = 0$ (diamonds), $\alpha = 0.5$ (triangles), and $\alpha = 1$ (squares). Note that we have replotted the data from $\alpha = 0$ merely for comparison. The dashed lines are from Eq. (5.12) (as in Fig. 5.6), with a fit of f_c yielding $f_c = 0.027$ for $\alpha = 0.5$ and $f_c = 0.032$ for $\alpha = 1$. Inset: Decay of $\langle Z_{ec} \rangle$ as a function of time for different grid sizes, $L = 8, 16, \dots, 256$ (left to right), and $\alpha = 1$. Parameters used in the simulations were $A/J = 0.1$, and $T/J = 0.3$. Times are in units of $(\kappa_1 J)^{-1}$.

5.7 Discussion of the long range interaction

So far we have assumed the presence of long-range anyon interactions. We briefly comment here on their possible realization. Concerning the many-body nature of the interactions involved, general n -body couplings can in principle be engineered from two-body interactions [KKR06, BDLT08, Wol08, JF08]. For example, toric codes with interacting anyons are derived in [HCC09, SDV08]. A systematic procedure to construct such effective low-energy Hamiltonians can be rigorously founded on the Schrieffer-Wolff transformation [BDLT08, Wol08]. In a similar way, physical long-range interactions of the type considered in this work could also be generated perturbatively. A well-known example is the Ruderman-Kittel-Kasuya-Yosida (RKKY) interaction [Kit87], e.g., for a 2D Kondo-lattice of nuclear spins [SL07]. Alternatively, constant interactions ($\alpha = 0$) can be realized for qubits coupled to photon modes in QED-cavities [Dic54, PGCZ95, IAB⁺99, WSB⁺04, BI06, TGL08]. The interaction range is determined by the wavelength of the photon and can reach macroscopic distances, in particular in superconducting cavity striplines [WSB⁺04, BI06, TGL08]. Another promising candidate system to realize topological models are ultracold atoms or molecules in optical

lattices [JBG⁺08, WML⁺10].

As a most elementary example, consider all plaquette operators interacting with a delocalized two-level system (acting as an ancilla qubit), in analogy to the so-called central spin problem. For example, $H_{\text{int}} = \Delta\sigma_z + \sum_p g_p n_p \sigma_x$ with eigenvalues $\pm \sqrt{\Delta^2 + (\sum_p g_p n_p)^2}$. A quadratic expansion of the higher eigenvalue $\simeq \Delta + \frac{1}{2\Delta} \left(\sum_p g_p n_p\right)^2$ (if $\Delta > 0$) gives a repulsive interaction between the anyons. Note that in this example the central spin has to be kept in the excited state.

A physically more interesting case is the two-photon coupling described by the Hamiltonian

$$H_{\text{int}} = \sum_{i=1}^2 \omega_i a_i^\dagger a_i + \sum_p g_p n_p (a_1^\dagger a_2 + a_1 a_2^\dagger). \quad (5.17)$$

Here, ω_i are the photon frequencies, and g_p is the coupling strength of plaquette p to the modes. This type of coupling naturally emerges in the perturbative derivation of the toric code model from the Kitaev honeycomb model [Kit06] if a quadratic coupling to electric (or magnetic) cavity fields such as $E_x E_y$ is added. We start from the expression of the anyon excitation energy obtained in leading order of perturbation theory, given by

$$J_0 = \frac{J_x^2 J_y^2}{8J_z^3}, \quad (5.18)$$

where J_k are the exchange couplings in the honeycomb lattice [Kit06, SDV08]. Since the couplings J_k are determined by exchange integrals, they can be modified by electric perturbations: In multiferroic materials, electric fields can couple to the spin (-texture) via a modification of the exchange interaction such as $J_k \rightarrow J_k + \delta_k (a_k + a_k^\dagger)$ [TTSL08, TTSL10] (with $\delta_{x,y,z}$ being some coupling constants and $a_{x,y} \equiv a_{1,2}$). Thus, if, for example, one J_x and one J_y occurring in $J_x^2 J_y^2 / 8J_z^3$ get modified in this way (by locally modifying the corresponding links), we end up with a coupling of the desired form with

$$g_p = \frac{J_x J_y \delta_x \delta_y}{2J_z^3}. \quad (5.19)$$

A possible concern is that the spin-electric couplings introduce several other interaction terms in addition to Eq. (5.17) [4]. By imposing the resonance condition $\omega_1 \approx \omega_2$, the quadratic term ($a_1^\dagger a_2 + a_2^\dagger a_1$) can be made dominant over the linear ones (which are non-resonant). Furthermore,

⁴As a simple example, we note that since the gap of the star anyons is also given by Eq. (5.18), an additional term $\sum_s g_s n_s (a_1^\dagger a_2 + a_2^\dagger a_1)$ appears in Eq. (5.17) which generates repulsive star-star as well as star-plaquette interactions.

higher-order terms can be neglected for $\delta_k \ll J_k$ (a more detailed analysis will be presented elsewhere [PCL11]).

The Hamiltonian Eq. (5.17) can be brought to the diagonal form $H_{\text{int}} = \sum_{i=1}^2 \Omega_i b_i^\dagger b_i$ by making use of a standard Bogoliubov transformation of the boson operators. Since g_p is spatially constant over the photon wavelength λ_i [Dic54], we assume in the following a constant value $g_p = g$, such that $\sum_p g_p n_p = gN$. Therefore,

$$b_1 = \cos \theta a_1 + \sin \theta a_2, \quad (5.20)$$

$$b_2 = \cos \theta a_2 - \sin \theta a_1, \quad (5.21)$$

with $\tan 2\theta = 2gN/(\omega_1 - \omega_2)$ and

$$\Omega_{1,2} = \frac{\omega_1 + \omega_2}{2} \pm \sqrt{\left(\frac{\omega_1 - \omega_2}{2}\right)^2 + (gN)^2}. \quad (5.22)$$

By expanding H_{int} to lowest order in g we obtain the desired constant anyon interaction,

$$H_{\text{int}} \simeq \sum_{i=1}^2 \omega_i b_i^\dagger b_i + \frac{b_1^\dagger b_1 - b_2^\dagger b_2}{\omega_1 - \omega_2} (gN)^2. \quad (5.23)$$

The same result can also be derived with the general method of the Schrieffer-Wolff transformation [IAB⁺99, TGL08] (see also Appendix D.3). The strength and sign of the interaction are tunable via the difference in frequencies and occupation numbers of the modes, and can consequently be made repulsive in a steady-state regime. We identify the parameters of Eqs. (5.1) and (5.2) as follows

$$J = J_0 + \frac{g^2}{\omega_1 - \omega_2} \langle b_1^\dagger b_1 \rangle \quad \text{and} \quad A = \frac{2g^2}{\omega_1 - \omega_2} \langle b_1^\dagger b_1 \rangle. \quad (5.24)$$

The value of J includes a small self-energy correction. For definiteness, we assumed that only the first mode (with $\omega_1 > \omega_2$) is populated while $\langle b_2^\dagger b_2 \rangle = 0$.

Similarly to the first example, the case of repulsive interaction corresponds to a larger occupation of the mode with higher frequency. This condition is never realized in equilibrium and thus requires excitation of the cavity mode, which is easily accomplished by an external laser. Therefore, this specific realization of the long-range interaction corresponds to some sort of optical pumping of the memory into its ground state. It allows to avoid the full machinery of active error-correction, but cannot be considered passive in the strict sense of the term.

Finally, while a non-equilibrium regime is generally needed for interactions obtained in second-order perturbation theory, it might be possible to derive repulsive interactions in the ground state at higher orders by a more elaborate construction.

at small L but it can also lead to a stable memory at a sufficiently large system size, if the initial encoding is in a state full of anyons ($n_p = 1$ at each plaquette, instead of $n_p = 0$).

5.8 Conclusion

We have discussed a generalization of the Kitaev toric code to include repulsive long-range anyon interactions. The properties of the system have been analyzed within a mean-field treatment, which we find to become accurate at large system size. Additionally, we have numerically studied the system dynamics via direct simulations. This has allowed us to demonstrate robust storage of the information encoded in the ground state manifold at large system size.

A similar model to ours, but with attractive instead of repulsive long-range interactions, was studied in Ref. [HCC09], and was also found to possess self-correcting properties. In that case, however, the interaction is logarithmically divergent with distance while we consider here more physical interactions, i.e., polynomially decaying. A dependence of this type is commonly found in condensed matter systems and, more specifically, we show that local coupling of the anyon operators to long-range optical modes would allow to realize such interactions. As for the periodic boundary conditions, these are not an essential ingredient to a topological stabilizer code [BK98, FM01].

Another important aspect of our study is that the properties of the memory are strongly influenced by the type of thermal bath. We obtained the size dependence of the memory lifetime for Ohmic and super-Ohmic baths, the latter representing an especially advantageous situation. For example, for typical stripline cavities with $\lambda_i \sim \text{cm}$ and typical lattice constants of 100 nm (e.g. quantum dots), we see that the anyon interaction stays constant over system sizes L as large as 10^5 . Extrapolating the super-Ohmic curve of Fig. 5.6, an enhancement factor $\sim 10^{20}$ is obtained at this value of L . With a single-spin lifetime $1/\gamma(-2J) \sim 1\mu\text{s} - 1\text{s}$ [HKP⁺07, AMR⁺08] this gives a memory lifetime $\tau \sim 10^{14} - 10^{20}$ s. However, the assumption that the super-Ohmic scaling is valid up to this large size might be violated (e.g., because $\gamma(0) = 0$ can only hold approximately).

In conclusion, we have demonstrated the existence of 2D stabilizer quantum memories at finite temperatures. In our model, the stability of the memory is due to a large effective gap created by the repulsive interactions, which results in a vanishing anyon density. Furthermore, the diffusive motion of the anyons is quenched in a super-Ohmic bath, when the diffusion process requires creation of new anyon pairs. We expect that similar systems in the presence of such interactions also prove useful as self-correcting quantum memories.

Incoherent Dynamics in the Toric Code Subject to Disorder

Adapted from:

B. Röthlisberger, J. R. Wootton, R. M. Heath, J. K. Pachos, and D. Loss,
“Incoherent dynamics in the toric code subject to disorder”,
Phys. Rev. A **85**, 022313 (2012).

We numerically study the effects of quenched disorder on the incoherent dynamics of anyons in two variations of the toric code. A new class of error-correcting codes based on random lattices of stabilizer operators is presented and is shown to be superior to the toric code for certain forms of biased noise. It is further argued that these codes are close to optimal, in that they tightly reach the upper bound of error thresholds beyond which no correctable CSS codes can exist. Additionally, we study the classical motion of anyons in toric codes with randomly distributed onsite potentials. In the presence of repulsive long-range interaction between the anyons, a surprising increase in the lifetime of encoded states with disorder strength is reported and explained by an entirely incoherent mechanism. Finally the coherent transport of the anyons in the presence of both forms of disorder is investigated, and a significant suppression of the anyon motion is found.

6.1 Introduction

A working quantum computer performing meaningful calculations unarguably requires information processing to be carried out in a fault-tolerant manner [NC00, Mer07]. This not only means protecting the information from the action of imperfect gates, but also storing it in a reliable way

during the course of computation. In the theory of quantum error correction, the state of a logical qubit can be encoded in the code space of a number of physical qubits [Got10]. The resulting redundancy allows one to implement fault-tolerant quantum gates and to periodically check for the occurrence of single-qubit errors using syndrome measurements. However, this kind of active error monitoring imposes an additional overhead on an already deeply involved vision. Therefore, the idea to manipulate and store quantum states in systems that already provide ‘built-in’ protection from errors has gained a lot of attention recently [Kit03, DKLP02, Bac06, NO09]. A promising approach in this direction is to encode information in the degenerate topologically ordered ground state of a suitable many-body Hamiltonian. Information is encoded in an entangled state distributed across a large number of qubits and can only be distinguished and modified non-locally. In this context, Kitaev’s toric code [Kit03] is arguably the best studied model to date. It is robust against local perturbation at zero temperature, as well as against thermal errors if long-range interaction between its fundamental excitations is present (see Refs. [HCC09, PCL11], and chapter 5).

Recent studies have focussed on coherent phenomena in the toric code that arise due to the additional presence of various forms of quenched disorder [TOC11, WP11, SPIbuR11, BK11]. Conversely, in this chapter, we numerically study incoherent (classical) effects caused by two particular forms of randomness. First, we consider a class of models similar to the toric code, but differing from the latter in that the syndrome check operators are chosen randomly from a set of 3-body and 6-body operators. We find that these models bear advantage over the toric code for biased noise, where bit-flip and phase-flip errors occur with different probabilities. We also present strong evidence that these codes are almost optimal, in the sense that they reach error thresholds close to the overall upper bound valid for any Calderbank-Shore-Steane (CSS) code [CS96, Ste96]. Second, we investigate the effect of random onsite potentials on the lifetime of states encoded in the regular toric code coupled to a thermal bath. We identify and describe an interesting regime, where, in the presence of long-range interactions, the lifetime of this quantum memory is enhanced for increasing disorder strength. Finally the effects of the random lattices on coherent anyon transport is investigated, both with and without additional randomness in the onsite potentials. The resultant slowdown of the anyonic motion is determined and its effect on the stability of the quantum memory is discussed.

This chapter is organized as follows: Section 6.2 reviews the toric code, which is the basis of all further studies in this chapter. We then show in Sec. 6.3 how to simulate the classical dynamics of excitations in the systems considered subsequently and also give some details on the numerics. Our main results are presented in Sections 6.4, 6.5, and 6.6,

followed by a conclusion in Sec. 6.7.

6.2 Review of the 2D toric code

The starting point of our investigation is Kitaev's 2D toric code [Kit03] which will be modified in the following sections to incorporate randomness. We provide here a brief outline of the original model for the sake of completeness. The 2D toric code consists of $2L^2$ spins- $\frac{1}{2}$ with each spin placed on an edge of an underlying $L \times L$ square lattice with periodic boundary conditions. One then defines two sets of mutually commuting four-body operators, called plaquettes and stars, respectively, in the following way (cf. Fig. 6.1a). A plaquette is the product of the Pauli σ_z operators associated with the four spins belonging to a single face of the square lattice, whereas a star is the product of the four σ_x operators of the spins on edges adjacent to a single vertex of the lattice. In this way, one obtains two sets of L^2 plaquette and star operators, out of which $L^2 - 1$ in each set are independent. Note that these operators can only have eigenvalues $+1$ and -1 .

One can then define a subspace \mathcal{C} of the total Hilbert space given by the $2^{[2L^2 - 2(L^2 - 1)]} = 4$ states which are simultaneous eigenstates of all independent plaquettes and stars with eigenvalue $+1$. This space can thus accommodate two logical qubits, and measuring the plaquette and star operators allows one to gather information about possible spin- and phase-flip errors without disturbing the encoded state. A negative plaquette (star) indicates the presence of one or three σ_x (σ_z) spin errors. The toric code belongs to the class of stabilizer codes, and the plaquettes and stars are in that context often referred to simply as stabilizer operators.

Notably, the code space \mathcal{C} is the degenerate ground space of the Hamiltonian

$$H = -J \sum_s A_s - J \sum_p B_p. \quad (6.1)$$

Here, $J > 0$ is the energy gap, and A_s and B_p are the stars and plaquettes, respectively, explicitly given by

$$A_s = \prod_{i \in \text{adj}(s)} \sigma_x^i, \quad (6.2)$$

$$B_p = \prod_{i \in \text{adj}(p)} \sigma_z^i, \quad (6.3)$$

where $\text{adj}(s)$ [$\text{adj}(p)$] denotes the set of spins on edges adjacent to the star (plaquette) s (p). The elementary excitations of the Hamiltonian Eq. (6.1) are stabilizer operators with negative eigenvalue and are referred to as 'anyons'.

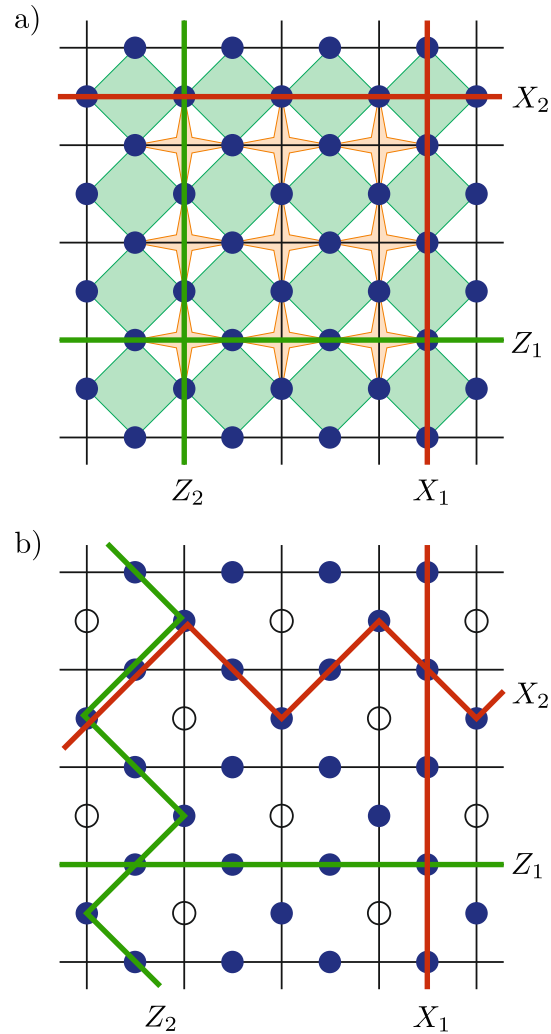


Figure 6.1: Toric codes. a) Kitaev's original 2D toric code. Shown is a 4×4 subregion of the $L \times L$ lattice. The blue solid dots on the edges of the lattice represent spins, the 4-body plaquette and star operators are shown in light green and orange, respectively (note that stabilizers containing spins outside the figure are not shown). All four logical Pauli operator strings are displayed as thick horizontal and vertical lines. b) The same region after modifying the lattice in order to incorporate randomness. The modified plaquette and star operators are not shown yet, see Fig. 6.2. The empty circles indicate the defect positions, i.e., the edges of the lattice where spins are removed. This requires altering the logical operators Z_2 and X_2 in the way shown. Note that all commutation relations between the logical operators are preserved.

Associated with the two logical qubits encoded in \mathcal{C} are four string-like operators (products of single-spin σ_x 's or σ_z 's) which wrap around the torus and commute with all plaquettes and stars, but act non-trivially

in the form of logical Pauli X and Z operators on the two qubits encoded in \mathcal{C} . We choose to label the operators such that X_1 is a vertical string on horizontal edges and Z_1 is a horizontal string on horizontal edges. Correspondingly, X_2 and Z_2 are horizontal and vertical strings, respectively, on vertical edges (see Fig. 6.1a).

When the system described by the Hamiltonian Eq. (6.1) is coupled to a noisy environment causing single-spin errors, pairs of anyons are created and can subsequently move diffusively on the toric surface. Eventually, the creation and diffusion of anyons leads to a pattern of errors containing undetectable loops around the torus, acting as unnoticed logical Pauli operators on the code space \mathcal{C} and therefore corrupting the state contained therein. Measuring the plaquette and star operators to locate anyons reveals some, but not all information about the underlying error pattern and is generally ambiguous. It is up to an error correction procedure (see Sec. 6.3) to deal with this problem in a satisfactory way.

The toric code has gained attention due to a series of interesting and advantageous properties. Namely, the stabilizer operators are local and independent of the system size L , while the code distance grows linearly with L . Closely related is the fact that the ground-state degeneracy is exponentially protected (in L) against local perturbations. Quite remarkably, the toric code is in a sense almost optimal within the class of all CSS codes [DKLP02], even though the latter contains codes with arbitrarily large stabilizer operators. We will revisit this topic in greater detail in Sec. 6.4.

6.3 Classical dynamics and numerical simulations

Classical dynamics from single-spin errors

Since the Hamiltonian Eq. (6.1) does not couple the star and plaquette operators, we can treat the two corresponding types of anyonic excitations independently. Furthermore, because the stars are simply plaquettes on the dual lattice, it is sufficient to study the dynamics of only one type, e.g., the plaquette anyons. We assume that each spin is coupled to an auxiliary system that can cause the spin to flip via σ_x errors. In the limit of weak coupling [Dav74, AFH09], one can derive the following system of coupled rate equations describing the classical dynamics of the system (see the Sec. 5.3):

$$\frac{d}{dt}p_{\mathcal{E}}(t) = \sum_i [\gamma_{i,\mathcal{E}}^{in} p_{x_i(\mathcal{E})}(t) - \gamma_{i,\mathcal{E}}^{out} p_{\mathcal{E}}(t)]. \quad (6.4)$$

Here, $p_{\mathcal{E}}(t)$ is the time-dependent probability to find the system in the state $|\mathcal{E}\rangle$ obtained by applying σ_x errors to all spins with indices in \mathcal{E} , i.e.,

$|\mathcal{E}\rangle = \prod_{k \in \mathcal{E}} \sigma_x^k |\psi_0\rangle$, where $|\psi_0\rangle$ is the initial state of the system. Similarly, $p_{x_i(\mathcal{E})}(t)$ describes the probability to be in the state $\sigma_x^i |\mathcal{E}\rangle$. Finally, $\gamma_{i,\mathcal{E}}^{in}$ and $\gamma_{i,\mathcal{E}}^{out}$ are the transition rates to arrive at or leave the state $|\mathcal{E}\rangle$, respectively, via a σ_x -error at the spin with index i .

In this chapter, we will consider two types of error environments. The first one is a constant error rate model, i.e., we set $\gamma_{i,\mathcal{E}}^{in} = \gamma_{i,\mathcal{E}}^{out} = \text{const}$. In this case, spin-flips are caused independently of any previously existing anyons and σ_x errors. The second model mimics the coupling to a thermal environment, where the transition rates are in general energy dependent. Consequently, we set $\gamma_{i,\mathcal{E}}^{in} = \gamma(-\omega_{i,\mathcal{E}})$ and $\gamma_{i,\mathcal{E}}^{out} = \gamma(\omega_{i,\mathcal{E}})$, where $\omega_{i,\mathcal{E}} = \epsilon_{\mathcal{E}} - \epsilon_{x_i(\mathcal{E})}$ is the energy difference between the states $|\mathcal{E}\rangle$ and $\sigma_x^i |\mathcal{E}\rangle$. An expression for $\gamma(\omega)$ often found in the literature is given by

$$\gamma(\omega) = 2\kappa_n \left| \frac{\omega^n}{1 - e^{-\beta\omega}} \right| e^{-|\omega|/\omega_c} \quad (6.5)$$

and can be derived from a spin-boson model [LCD⁺87, DL05]. Here, κ_n is a constant with units $1/\text{energy}^n$ setting the time scale, $\beta = 1/k_B T$, with T being the temperature of the bath and k_B denoting Boltzmann's constant, and ω_c is the cutoff frequency of the bath. In the following, we set $\omega_c \rightarrow \infty$ for simplicity. A bath with $n = 1$ is called 'Ohmic', whereas one with $n \geq 2$ is called 'super-Ohmic'. Only the former case is considered in this chapter. Unless otherwise stated, all energies will be expressed in units of $k_B T$. Consequently, the unit of time is $(\kappa_1 k_B T)^{-1}$.

Simulations and error correction

Clearly, it is impossible to solve Eq. (6.4) analytically for meaningful system sizes, because the number of states $p_{\mathcal{E}}$ grows exponentially with L^2 . We thus have to stochastically simulate the system and obtain the quantities of interest, such as the number of anyons or the expectation values of the logical operators, by averaging over many (typically several thousand) instances. In greater detail, the iteration of the simulation at time t consists of these steps: (i) Calculate all unnormalized single spin-flip probabilities $p_i = \gamma(\epsilon_{\mathcal{E}} - \epsilon_{x_i(\mathcal{E})})$, then obtain from them the total spin flip rate $R = \sum_i p_i$. (ii) Draw the time Δt until the next spin flip from an exponential distribution with rate R . (iii) Calculate and record all quantities of interest for time sampling points lying in the interval $[t, t + \Delta t]$. Namely, these quantities are the number of anyons, the number of σ_x errors, and the uncorrected and error-corrected (see below) logical operators Z_1 and Z_2 . (iv) Determine a random spin according to the probabilities p_i/R , flip it, and set t to $t + \Delta t$.

The error correction step in the toric code consists of pairing up all detected anyons and then annihilating them by connecting each pair with a string of errors from one partner to the other. The pairing is usually

chosen such that all anyons are annihilated with the smallest total number of single-spin operators. This is known as the minimal-weight perfect matching and can be found in polynomial time with the help of the ‘blossom’ algorithm due to Edmonds [Edm65]. The runtime complexity of this algorithm has been improved several times since its discovery. We are employing the library Blossom V [Kol09] which implements the latest version running in $O(mn \log n)$ time, where n is the number of anyons (vertices) and m the number of connections (edges) between them.

In order to find the true matching with minimal weight, one in principle would need to choose the set of edges to include all connections from every anyon to every other. However, since the size of this set grows quadratically with the number of anyons n , the overall scaling of the matching algorithm becomes $O(n^3 \log n)$ which is infeasible for large n . We therefore first perform a Delaunay triangulation in negligible $O(n \log n)$ time using the library Triangle [She96]. The result is that only anyons close to each other are connected using a number of edges linear in the number of anyons. It turns out that this is an excellent approximation yielding results that are nearly indistinguishable from those obtained from a matching over the complete graph.

Within the paradigm of active error correction, where the anyons are detected and corrected periodically on sufficiently small time intervals, the encoded state can be kept free of logical errors almost indefinitely. However, since we are interested in the use of the toric code as a passive quantum memory, we are mostly concerned with the lifetime τ of the encoded information in a scenario where error correction is only performed once at readout. Hence, whenever we show plots of the ‘error-corrected’ logical operators decaying as a function of time, we thereby refer to their value if error correction had been performed at that time, without actually performing it. We then define the lifetime of the system as the time it takes for the expectation values of the error-corrected logical operators to decay to 90% of their initial value.

6.4 Random lattices

In this section, we study the error thresholds of a family of models obtained by randomly modifying the toric code in a way that preserves its basic features. We first describe how we create our random lattices and then present and discuss the results of the simulations within the context of optimal quantum codes.

Generating the lattices

Starting from the toric code on an $L \times L$ lattice, we remove $\frac{1}{2}L^2$ spins at specific and regularly distributed ‘defect’ locations. The structure of

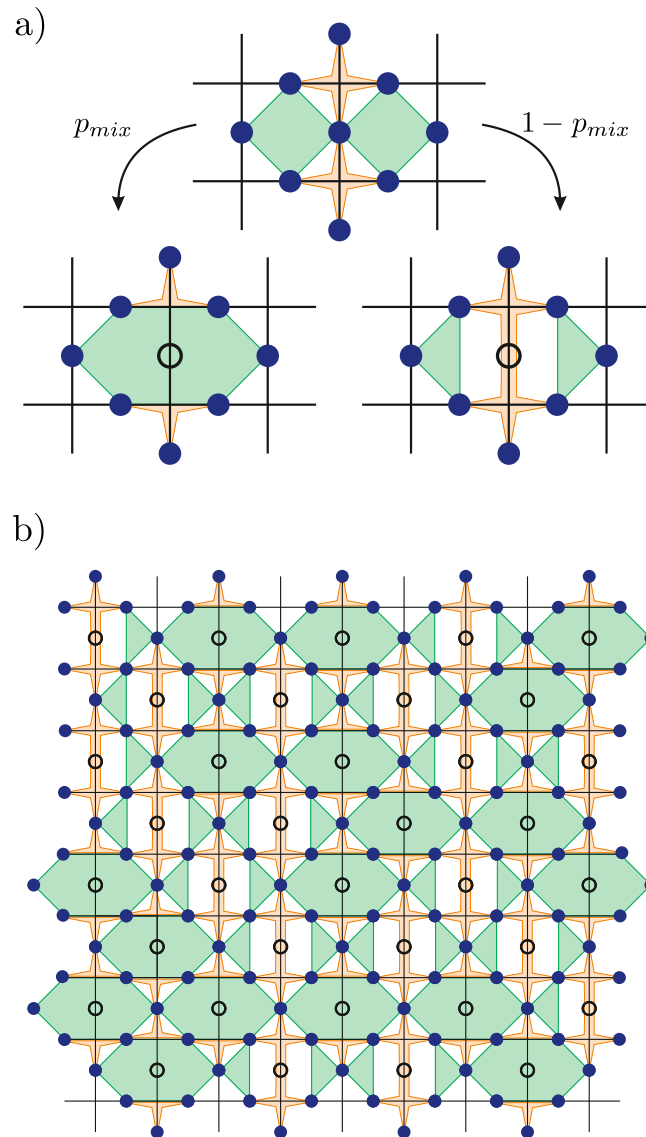


Figure 6.2: Modifying the stabilizer operators. a) When removing a spin (empty circle), we choose between two ways of adapting the affected stabilizer operators. With probability p_{mix} we join the two plaquette operators to one large 6-body operator and reduce the two stars from 4- to 3-body operators. Alternatively, with probability $1-p_{mix}$, we perform the dual operation, namely we define two 3-body plaquettes and one large 6-body star. Spins and operators not affected by removing the central spin are not shown in this example. b) Typical 8×8 subregion of a (larger) random lattice with $p_{mix} = 0.5$. Logical operators as well as some spins and operators at the edges with the rest of the lattice are not shown.

the defect pattern can be easily understood from Fig 6.1b. Basically, every second vertical edge is labelled a defect, with the first defect of each row alternatingly being created on the first or second vertical edge of that row. Note that the height and width of the grid both must be even in order for this procedure to be consistent with the periodic boundary conditions. We now have to modify all plaquettes and stars as well as the logical Pauli X and Z operators such that all original commutation relations remain unaltered.

Let us start with the logical operators. Clearly, both X_1 and Z_1 (with single-spin operators exclusively on horizontal edges) are unaffected by the introduction of defects on vertical edges of the lattice. However, the pair of operators in the original code acting on the second encoded qubit is defined on vertical edges and thus needs to be adapted. Clearly, the operators must remain connected strings wrapping around both dimensions of the torus. The ‘zig-zag’ pattern shown in Fig. 6.1b achieves this with the smallest increase in the number of single-spin operators. It is straightforward to verify that these new X_2 and Z_2 operators, together with the unaltered pair acting on the first encoded qubit, indeed fulfill all original commutation relations between each other.

We now discuss the modification of the plaquette and star operators. Removing one spin, i.e., creating one defect, affects exactly two adjacent plaquettes and two adjacent stars. We will consider two possible ways of dealing with this situation (cf. Fig. 6.2). We can either (i) define two restricted 3-body plaquettes and one ‘vertical star’ consisting of the product of the remaining 6 single-spin σ_x operators, or (ii), perform the dual operation, namely defining one large 6-body ‘horizontal plaquette’ and two restricted 3-body stars. The two ways of modifying the original operators are depicted in Fig 6.2a. It is relatively easy to see that these new 3-body and 6-body operators remain mutually commuting, and furthermore commute with all modified logical Pauli operators just as in the original code. Note that also the dimension of the code space is left unchanged since it generally only depends on the genus of the surface covered by the anyon operators [Kit03]. We can now create a random lattice by choosing at each defect site to create a 6-body plaquette with probability p_{mix} and two 3-body plaquettes with probability $1 - p_{mix}$. See Fig. 6.2b for a typical example. The special case $p_{mix} = 0$ corresponds to a regular lattice of 3-body plaquettes and 6-body stars, whereas $p_{mix} = 1$ conversely yields a regular lattice of 6-body plaquettes and 3-body stars. In both cases, the 3-body operators are the vertices of an underlying hexagonal lattice, whereas the 6-body operators form the vertices of its dual, the triangular lattice.

Results

Before we start discussing the results, we would like to briefly point out a modification to the error correction scheme we had to incorporate in order to deal with the random lattices. Since it would be difficult to adapt the Delaunay triangulation to an irregular graph, we have replaced this step by a breadth-first search performed on each anyon. This procedure connects every anyon to at most k of its nearest neighbors, where distance is measured not in a Euclidean sense, but as the number of errors in a connecting string. For constant k , this requires a runtime of $O(n)$, where n is the number of anyons. We have found that $k = 10$ is an excellent approximation to $k = \infty$ and have used this value in all calculations.

We have performed a series of Monte Carlo simulations to determine the critical fraction of errors f_{cr}^Z independent of any form of anyon dynamics (see Appendix E for additional results in the case of thermal errors). If the probability for each spin to independently be affected by a σ_x error becomes larger than this critical value in the limit $L \rightarrow \infty$, the error correction scheme undergoes a transition from performing fully accurate error recovery to randomly guessing the error-corrected state with the lowest possible success rate of 50%. We can determine f_{cr}^Z by plotting the expectation values of the error-corrected logical Z operators as a function of the error probability f for different lattice sizes and observe at which value of f the curves intersect [1].

Fig. 6.3a displays typical results for a few different values of p_{mix} . We observe that the expectation values of Z_1 and Z_2 in general have a different dependence on the error probability f . This is due to the fact that on a lattice with, e.g., a majority of 6-body plaquettes, it takes on average fewer spins to form a loop around the horizontal direction of the torus than around the vertical one. The opposite argument holds in the case of a 3-body plaquette majority. Not surprisingly, Z_1 and Z_2 decay identically for a 50 per cent mixing of 3- and 6-body plaquettes. Note that, despite the typically unequal decay of Z_1 and Z_2 as a function of f , the error thresholds for the two operators are always identical for a given value of p_{mix} . This is consistent with the general understanding that the correctability of the memory as a whole is related to the phase of a corresponding random-bond Ising model [DKLP02]. Indeed, our numerically determined thresholds for the regular 3-body and 6-body plaquette lattices agree well with the recently calculated multicritical points in spin glass models on hexagonal and triangular lattices, respectively [Ohz09]. Specifically, we find $f_c \approx 0.1585$ for $p_{mix} = 0$ (theoretical value: $f_c = 0.1640$) and $f_c \approx 0.0645$ for $p_{mix} = 1$ (theoretical value: $f_c = 0.0674$). The discrepancy of about 4 – 5% between the numerical and theoretical

¹Note that f_{cr}^Z could equivalently be obtained from dynamical simulations in the presence of a bath with constant error rates at the time where the error-corrected logical Z operators for different system sizes intersect.

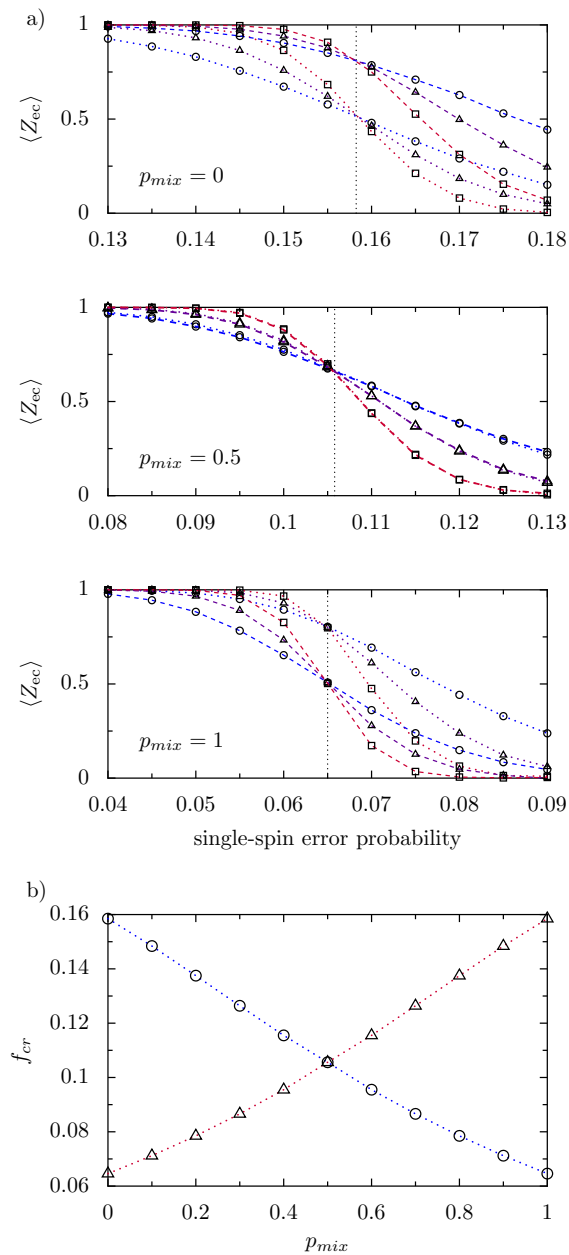


Figure 6.3: Critical error thresholds of random models. a) Three example plots of data used to determine the critical error thresholds. Each plot shows, for a specific value of p_{mix} , the expectation values of the logical Z_1 (dotted lines) and Z_2 (dashed lines) operators for grid sizes $L = 32$ (circles), 64 (triangles), and 128 (squares). The vertical dotted lines indicate the position of the error threshold. Data points are obtained by bootstrapping 1000 sample values, each of which is obtained by averaging over 200 random error distributions on a single instance of a random lattice. b) Error thresholds [as determined in a)] of Z (circles) and X (triangles) operators as a function of p_{mix} . The dotted lines are guides to the eye.

thresholds is of the same size as in the case of the toric code on a square lattice (where we had found $f_c \approx 0.1055$ as compared to the theoretical value $f_c = 0.1092$, see Sec.5.4) and can generically be attributed to the failure of the minimal-weight perfect matching close to the threshold. Interestingly, our numerical results suggest that the thresholds of the toric code and our random lattice models with $p_{mix} = 0.5$ are identical.

We show in Fig. 6.3b the critical fraction of errors f_{cr}^Z for the logical Z operators determined in the way described above as a function of the lattice mixing probability p_{mix} . Since the plaquette and star lattices are dual to each other (to every 6-body plaquette correspond two 3-body stars and vice versa), the critical fraction f_{cr}^X of σ_z errors for which error correction of the logical X operators fails (also plotted in Fig. 6.3b) is simply given by

$$f_{cr}^X(p_{mix}) = f_{cr}^Z(1 - p_{mix}). \quad (6.6)$$

At equal mixing, i.e., $p_{mix} = 0.5$, the threshold values are given by $f_{cr}^X(0.5) = f_{cr}^Z(0.5) \approx 0.1055$.

Consequently, one of the thresholds for the two different types of Pauli operators, either f_{cr}^X or f_{cr}^Z is always smaller than or equal to the threshold of the toric code. Our random lattices thus bear no advantage over the latter in the case of a uniform error model, where σ_x and σ_z errors occur with the same probability. The situation is different, however, for biased noise. If bit-flips and phase-flips are created with different probabilities, we can make use of the asymmetry in the error thresholds for $p_{mix} \neq 0.5$. Assuming, for instance, that σ_x errors are more frequent than σ_z errors would lead to an overall lifetime decrease of encoded states in the toric code due to the shorter lifetimes of the logical Z operators. However, starting from a random model at $p_{mix} = 0.5$, a decrease in p_{mix} will lead to an increase of the Z lifetimes and a decrease of the X lifetimes. If the error frequencies are not too different, the lifetimes will become identical at some value $0 \leq p_{mix} < 0.5$ and will be larger than the overall lifetime of the toric code. We thus conclude that the random lattices can be employed to increase the lifetime of encoded states compared with the toric code on a square lattice in the presence of biased noise. While these lattices require both error probabilities to fall in the range $0.0674 \leq p \leq 0.1640$ (and below the boundary in Fig. 6.4, see next section), it should in principle be possible to extend this range to $0 \leq p \leq 0.5$ by defining stabilizers with more than 6 single-spin operators in a similar fashion.

Relation to optimal quantum codes

We now discuss our random lattices within the context of optimal quantum coding. It is well known that, assuming a biased constant error model, there is an upper bound on the fraction of logical qubits k and

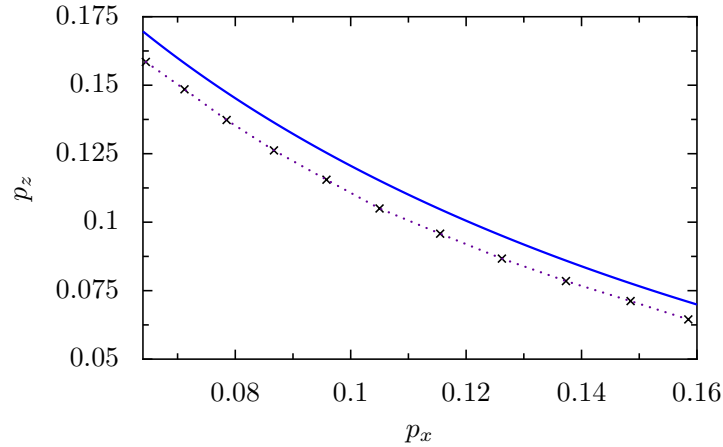


Figure 6.4: Theoretical upper bound on biased noise correctable by CSS codes. Given an error model of independent σ_x and σ_z errors occurring with constant probabilities p_x and p_z , respectively, there exists no CSS code able to cope with pairs of error probabilities lying above the solid line given by the zero-contour of Eq. (6.7). The crosses are the numerically determined pairs of thresholds of the random models for $p_{mix} = 1$ down to $p_{mix} = 0$ from left to right. The dotted line is a guide to the eye.

physical qubits n that encode them, valid for all CSS codes. This bound is given by [Ste96, DKLP02, GL03]

$$k/n \leq 1 - H(p_x) - H(p_z), \quad (6.7)$$

where $H(x) = -x \log_2 x - (1-x) \log_2 (1-x)$ is the Shannon entropy, and p_x and p_z are the probabilities for a single spin to be affected by a σ_x and σ_z error, respectively. The bound Eq. (6.7) can be motivated with the following intuitive (but somewhat hand-waving) argument we were not able to find in the literature.

An ideal CSS code would be able to detect for each physical qubit if it was suffering from a σ_x or a σ_z error. Assuming that these errors are uncorrelated, the number of classical bits required to store this information is asymptotically given by $nH(p_x) + nH(p_z)$. If we are to store the same information in qubits instead of bits, the Holevo bound [NC00] requires the usage of at least as many qubits to do so. Since our optimal CSS code needs to store the information of k encoded qubits, as well as all possible occurrences of errors, we have

$$n \geq k + nH(p_x) + nH(p_z). \quad (6.8)$$

Dividing by n and rearranging the terms yields the desired bound Eq. (6.7).

For unbiased errors with $p = p_x = p_z$, the right-hand side of Eq. (6.7) becomes zero at $p \approx 0.110028$, implying that there cannot be any CSS code coping with an error rate larger than this value. Quite remarkably,

the critical error probability for the toric code has been determined to be $f_{cr} = 0.109187$ [Ohz09]. This is astonishingly close to the upper bound, especially when taking into account that all stabilizers are local 4-body operators. Moreover, inserting the error thresholds for the regular 6-body plaquette lattice and its dual lattice of 3-body stars ($p_{mix} = 1$) into the right-hand side of Eq. (6.7) evaluates to

$$1 - H(0.0674) - H(0.1640) \approx 6 \times 10^{-5}, \quad (6.9)$$

which is virtually zero, indicating that the code is close to optimal for this particular biased error model. Due to the symmetry of Eq. (6.7) with respect to the error probabilities and the duality of the triangular and hexagonal lattices, the same argument holds for a lattice with 3-body plaquettes and 6-body stars ($p_{mix} = 0$) with the values of p_x and p_z exchanged. With our random lattices, we can thus continuously interpolate between two optimal models by changing p_{mix} . This suggests that the random models are optimal for all values of p_{mix} , in the sense that for every $0.0674 \leq p_x \leq 0.1640$ there is a random model with a theoretically (close to) maximal possible threshold for p_z . The results plotted in Fig. 6.4 strongly support this claim. The solid line is the zero-contour of the upper bound Eq. (6.7) and the crosses are the threshold pairs of the random lattices determined numerically. Note that the numerical data is within the typical 5% distance of theoretical bound. This can once again be explained by the failure of the minimal-weight error correction algorithm close to the thresholds. This observation, together with the knowledge from theory that the models are virtually optimal for $p_{mix} = 0$ and $p_{mix} = 1$ leads us to conjecture that the random models are virtually optimal for all values of p_{mix} . However, carrying out a theoretical study in the fashion of Ref. [Ohz09] is outside of the scope of the present work and is deferred for future research.

6.5 Random onsite potentials

This section is devoted to the study of the classical dynamics of anyons in the regular toric code on a square lattice, but with randomly modified anyon onsite energies. We are also particularly interested in the case where long-range anyon-anyon interaction is present, as this has been shown in the previous chapter to generally enhance the lifetime of the memory due to the suppression of the anyon density with increasing system size. For this, it is convenient to introduce the new stabilizer operators $n_s = (1 - A_s)/2$ and $n_p = (1 - B_p)/2$, where A_s and B_p are the usual star and plaquette operators, respectively. These operators are zero in the absence of an anyon on the respective site, and equal to 1 otherwise. The

more general Hamiltonian can then be written as

$$H = \frac{1}{2} \sum_{pp'} U_{pp'} n_p n_{p'} + \frac{1}{2} \sum_{ss'} V_{ss'} n_s n_{s'}, \quad (6.10)$$

where $U_{pp'}$ and $V_{ss'}$ contain the onsite energy and repulsive anyon interaction terms. Since in this model plaquette and star anyons are still independent, we can set $V_{ss'} = 0$ and note again that all results for the plaquette anyons hold equally for the stars. We then set

$$U_{pp'} = 2J_p \delta_{pp'} + \frac{A}{(r_{pp'})^\alpha} (1 - \delta_{pp'}), \quad (6.11)$$

where J_p is the onsite energy of an anyon on the plaquette with index p , A is the interaction strength, $r_{pp'}$ is the shortest distance on the torus between plaquettes p and p' , and $0 \leq \alpha < 2$ is the (long-range) interaction exponent. The onsite energies J_p are chosen randomly from a distribution with mean zero in order to discriminate effects caused by the randomness from such potentially caused by the system having a non-zero mean gap.

We focus on the case of constant interaction, i.e., $\alpha = 0$, and Ising-like randomness, meaning that the J_p are chosen from $\{-\sigma, +\sigma\}$ with equal probabilities. We refer to $\sigma \geq 0$ as the disorder strength. This model is interesting mostly for two reasons. First, it is the most convenient system incorporating randomness with respect to numerical simulation. Since the interaction is constant and thus simply depends on the total number of anyons, only six different single-spin flip rates need to be updated at each iteration step, depending on the number and configuration of adjacent anyons and onsite energies, respectively. Second, this simple model already displays all dynamical effects also present in more complicated systems (e.g., $\alpha \neq 0$ and Gaussian distribution of J_p 's, see Appendix F) and thus serves as an ideal playground for studying and understanding these effects. Naively, one would expect that the presence of negative onsite energies in the system simply favors the creation of anyons and is thus always disadvantageous for the lifetime of the memory. While this is indeed true for a non-interacting system, we find a regime in the interacting case where, quite surprisingly, the lifetime is enhanced for increasing disorder strength.

Fig 6.5 presents the results for the two cases. The non-interacting system is stable against disorder strengths that are roughly equal to the temperature but then decays for larger σ . This can be understood easily from the detailed balance condition satisfied by the rates Eq. (6.5): The ratio of the creation and annihilation rates of a pair of anyons on two sites with negative onsite energy is given by $\gamma(2\sigma)/\gamma(-2\sigma) = \exp(2\beta\sigma)$, which becomes large for σ 's exceeding the temperature. It is thus exponentially more likely for a pair of anyons to be created than annihilated for $\sigma > k_B T$, thereby quickly cluttering the system with anyons and

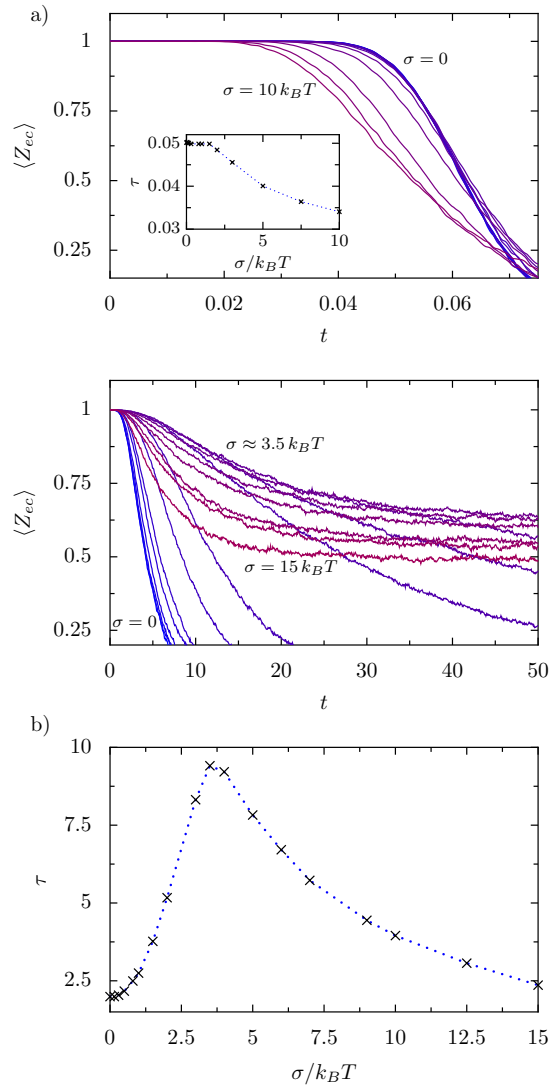


Figure 6.5: Influence of disorder on the memory lifetime. a) Time evolution of error corrected Z operators for a non-interacting (top) and interacting (bottom, $\alpha = 0$, $A = 0.5$) model. Both systems are of size 32×32 unit cells (2×32^2 spins) and are coupled to an Ohmic bath at temperature $T = 1$. The different curves display $\langle Z_{ec}(t) \rangle$ for different disorder strengths σ of Ising-like randomness with onsite energies $J_p = \pm\sigma$. In the non-interacting system, σ is increased from 0 to $10 k_B T$ as indicated in the panel. The inset displays the lifetime of the memory, i.e., the time at which $\langle Z_{ec} \rangle$ hits 0.9, as a function of σ . The disorder strengths examined in the interacting case have been chosen as $0 \leq \sigma \leq 15 k_B T$ (see main text and labels in the panel). b) The lifetimes of the interacting model extracted from the curves of the lower panel in a). The dotted line is a guide to the eye.

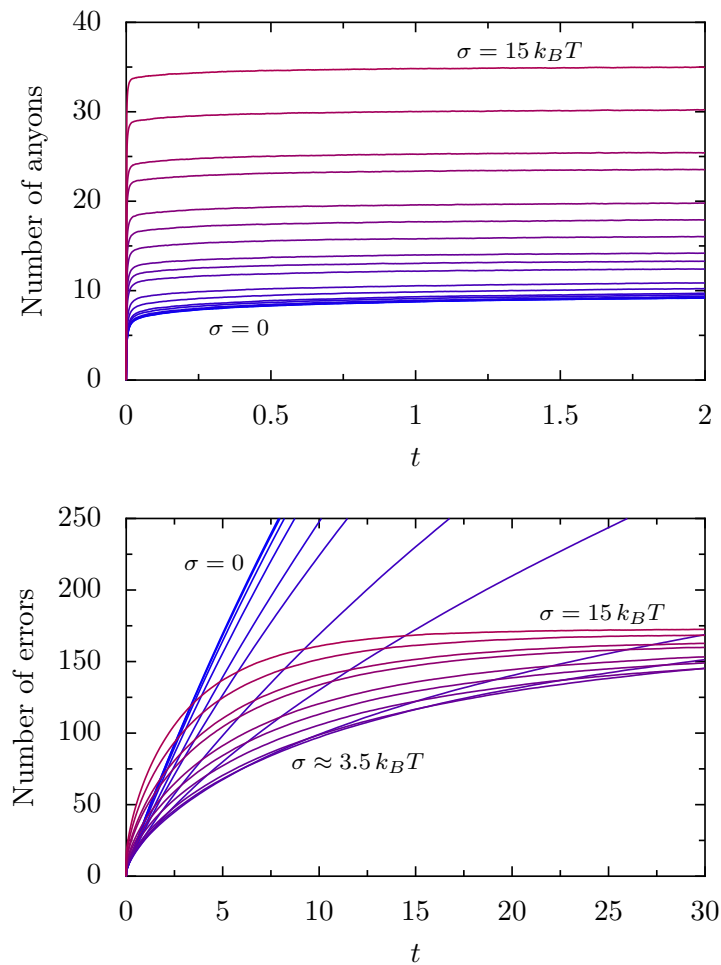


Figure 6.6: Number of anyons (top) and number of single-spin errors (bottom) as a function of time in an interacting system ($\alpha = 0, A = 0.5 k_B T$) of size 32×32 coupled to an Ohmic bath. The strength of the Ising-like randomness is increased from $\sigma = 0$ to $\sigma = 15 k_B T$ as indicated in the panels (see also main text).

crossing the critical fraction of errors. This situation changes completely in the presence of interactions between the anyons. The data shown in Fig. 6.5 displays a steep increase in the lifetime as a function of the disorder strength, peaking at around $\sigma \approx 3.5 k_B T$ for that particular system, followed by a slower decay.

We can shed some light on this effect by additionally looking at the number of anyons and the number of errors as shown in Fig. 6.6. For any fixed value of σ , the number of anyons again increases quickly but then saturates almost instantaneously at the equilibrium value. At this point, creating a new pair of anyons costs an energy penalty due to the repulsive interaction that can no longer be compensated by the negative onsite potentials. One can clearly see that the equilibrium number of

anyons increases linearly with σ , which implies that the corresponding enhanced memory lifetimes cannot be explained by a suppression of the anyon density.

However, the error creation rate (i.e., the slope of the curves in the lower panel of Fig. 6.6) exhibits a pronounced minimum at the same value $\sigma \approx 3.5 k_B T$ that also yields the maximal lifetime. Such an initial decrease in the error rate despite an increasing number of anyons can only be consistently explained by a suppression of the anyon diffusion. For disorder strengths $\sigma \gg k_B T$, processes that create anyons on two positive sites or that move an anyon from a negative to a positive site are exponentially suppressed. The positive sites thus effectively act as infinite barriers that greatly reduce the mobility of the anyons, and the encoded state is solely destroyed by diffusing anyons restricted to the negative sites [2]. As the disorder strength is lowered, two competing effects come into play. On the one hand, the number of anyons is reduced linearly. On its own, this would lead to a longer lifetime due to the presence of fewer diffusing anyons. On the other hand, the barriers separating the regions of negative sites are lowered, which facilitates the diffusion across longer distances and promotes a reduction in lifetime. The observed maximum in the memory lifetime can thus be understood as a tradeoff between having few but relatively freely moving anyons for $\sigma \ll k_B T$, and more but very restricted anyons for $\sigma \gg k_B T$. The interaction merely plays the role of restricting the anyons to a small enough (for $\sigma \lesssim k_B T$) and constant number. Appendix G contains results that further support the picture described above.

6.6 Quantum dynamics

The toric code ground state has been shown to be stable against local perturbations of sufficiently small strength [BHM10, DKOSV11]. The effect on excited states, however, is more disastrous. Perturbations allow the hopping of any anyons that are present, causing the quantum memory to become unstable [Kay09, PKSC10]. It has been found that this problem can be solved by the presence of disorder in the couplings of the model [WP11, SPIbuR11], since the disorder suppresses anyon motion through a localization effect. In this section we study the effects of the disorder introduced by using the random lattices.

²Note that the error correction is unaware of the distribution of negative and positive onsite energies. If it were, this information could in principle be used to improve the lifetime of the memory.

Error model

Consider the toric code Hamiltonian, perturbed by a magnetic field of strength h . For concreteness, let us choose this to be of the form,

$$H = \sum_p J_p n_p + \sum_s J_s n_s + h \sum_i \sigma_x^i. \quad (6.12)$$

The effects of such a perturbation have been studied using the methods of Refs. [WP11, SPIbuR11], where it was noted that, since the σ_x^i do not commute with the n_p , the perturbation will have the effect of creating, annihilating and transporting plaquette anyons. For $h \ll J_p$ all these effects apart from the transport are suppressed by the energy gap, allowing the system to be modelled as the following many-particle quantum walk Hamiltonian,

$$\begin{aligned} H_p &= \sum_{p,p'} M_{p,p'} t_{p,p'} + U \sum_p n_p (n_p - 1), \\ M_{p,p'} &= \delta_{\langle p,p' \rangle} h + \delta_{p,p'} J_p. \end{aligned} \quad (6.13)$$

Here $\delta_{\langle p,p' \rangle} = 1$ only when the plaquettes p and p' share a spin. The operator $t_{p,p'}$ maps a state with an anyon on the plaquette p to that with the anyon moved to p' , and annihilates any state without an anyon initially on p . Since the anyons are hardcore bosons, we are interested in the case of $U \rightarrow \infty$.

This effective description in terms of quantum walks of anyons holds also for a more general magnetic field and other local perturbations. The effects of anyonic braiding occur at a higher order of perturbation theory than those of this effective description, and hence may be ignored. The dynamics of the plaquette and vertex anyons can therefore be considered separately. Since they are dual to each other, once again only the plaquette anyons are considered here without loss of generality.

The Hamiltonian H_p is difficult to solve in general. However, note that the dynamics of H_p are driven by the matrix M , i.e., the Hamiltonian for a single particle walk. Hence, by considering the case of a single anyon, important aspects of the behavior for the many-particle walks can be determined. It is this approach that is taken here. The Hamiltonian M is applied to a single anyon, initially placed on an arbitrary plaquette of the code. The motion of the anyon can be characterized by the time evolution of its standard deviation, Δ . Since finite values of the system size L must be used in the numerics, the walks will, at some point, interact with the boundary. In order for this effect to be ignored, the run time of the walks is limited to ensure this interference always remains negligible.

The behavior of Δ over time for walks on square, triangular and hexagonal lattices for which all J_p are uniform can be found in Fig. 6.7. In each case the standard deviation of the distance increases linearly with

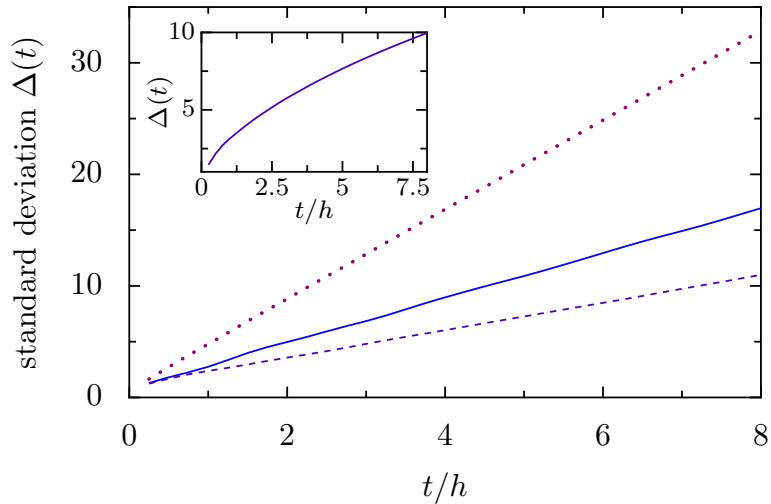


Figure 6.7: Time evolution of the standard deviation $\Delta(t)$ of a single quantum walker on lattices with uniform couplings $J_p = J$ for all p . The different curves correspond to a square lattice (solid), 3-body plaquette lattice (dashed), and 6-body plaquette lattice (dotted). Inset: $\Delta(t)$ on the random lattices from Sec. 6.4 with $p_{mix} = 0.5$, where each point has been averaged over 1000 samples.

time, demonstrating the ballistic motion expected from quantum walks when no disorder is present.

The ballistic motion caused by the field is highly damaging to the quantum information stored within the code. Suppose that the toric code initially has some density ρ of anyon pairs, due perhaps to noisy preparation of the state or interaction with the environment. If ρ is sufficiently small then the pairs will be far apart, allowing error correction to be performed reliably. However, when the perturbation is present this will only remain true for a finite lifetime τ , after which the motion of the anyons prevents them from being paired reliably. This occurs when they have moved a distance comparable to the average distance between pairs, and hence when $\Delta(\tau) \sim 1/\sqrt{\rho}$. Since $\Delta(t)$ grows linearly with time for ordered quantum walks (cf. Fig. 6.7), the quantum memory will fail within a time of order $\tau = O(1/\sqrt{\rho})$. Mechanisms which slow down the anyons are therefore favorable to the quantum memory, since they lead to longer lifetimes. It is this effect that is expected from the disorder.

Random lattices

Let us now introduce disorder by using the random lattice of Sec. 6.4 while still keeping the J_p (and J_s) uniform, all taking the same value J . Specifically the case of $p_{mix} = 0.5$ is considered, to maintain the symmetry between plaquette and star anyons. The behavior of the standard

deviation of the distance moved by a single walker is shown for this lattice in the inset of Fig. 6.7. Rather than increasing linearly with time t , as in the ordered case, it is found that $\Delta(t)$ grows with the square root of t . The motion of a quantum walker is therefore diffusive rather than ballistic in this case. As such, the random lattice leads to a significant slowing of the anyon motion, increasing the lifetime to $\tau = O(\rho^{-1})$ (note that we always have $\rho \leq 1$). It is possible that the random lattice also induces Anderson localization [And58], in which case the lifetime will be increased further, but the system sizes which may be probed are too small for this to be evident.

Random lattices together with J disorder

It is known that, when disorder in the J_p couplings is present in the toric code, Anderson localization is induced [WP11, SPIbuR11]. This effect exponentially suppresses the motion of the walkers, and causes the standard deviation of the distance to converge to a constant value. We therefore have $\tau \rightarrow \infty$, i.e., the memory stays stable against the perturbation for an arbitrarily long time. It is now important to determine whether the combination of randomness in both the lattice and the J_p couplings enhances or diminishes this effect.

To study this, disorder in the J_p couplings are considered. Specifically, each J_p randomly takes either the value $J - \sigma$ or $J + \sigma$ with equal probabilities. The value J is unimportant, but the ratio of σ/h characterizes the strength of the disorder in comparison to the magnetic field. Guided by the numerical results of [WP11], we consider here disorder of strength $\sigma/h = 250$ to ensure that the localization effect is observed for moderately sized systems.

In Fig. 6.8, the time evolution of the standard deviation is shown for the case of J disorder on a square and a random lattice. In both cases the localization effect is seen, with the walk unable to move far beyond a few times the length scale separating neighboring vertices. The walks with and without the lattice disorder give very similar results, especially at longer times. The effect of localization in the random lattice therefore seems the same as that of the square, without significantly enhancing or diminishing the effect.

6.7 Conclusion

We have studied the influence of quenched disorder on the incoherent (classical) motion of anyons in modified forms of the toric code. We have first described a class of random models that can be obtained from the toric code by removing a regular sublattice of spins, and then for each defect site randomly choosing one of two ways to adapt the affected stabi-

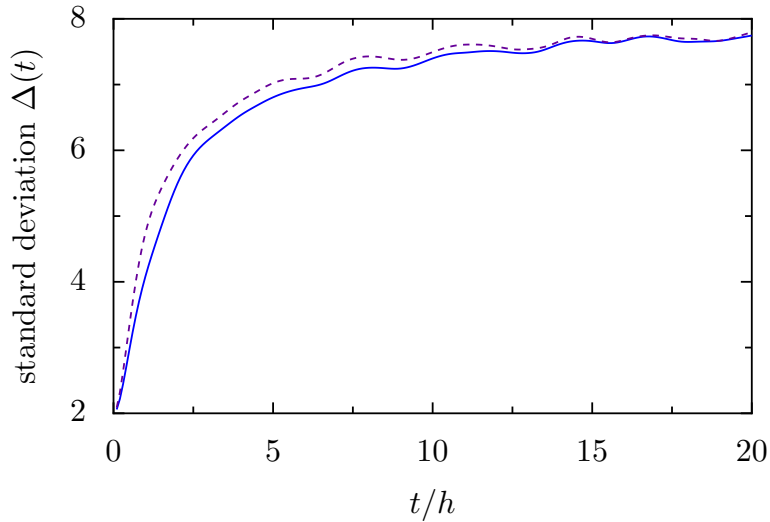


Figure 6.8: Time evolution of the standard deviation $\Delta(t)$ for a single anyonic walker with disorder in the J_p of $\sigma/h = 250$, on both a square lattice (solid line) and a random lattice (dashed line) with $p_{mix} = 0.5$. Each point has been averaged over 1000 samples.

lizers with a probability p_{mix} . The critical fractions of independent errors at which these codes become uncorrectable have then been determined numerically as a function of p_{mix} . We have shown that in the presence of biased noise, where bit flips and phase flips occur at different probabilities, the models based on random lattices can tolerate higher thresholds than the toric code in one type of errors, given the other type is correspondingly lower. These thresholds have been demonstrated to be close to the upper bound correctable by any CSS code. Second, we have studied the toric code subject to randomness in the onsite potentials. Specifically, we have demonstrated that in the presence of repulsive long-range interaction between anyons, there is a pronounced maximum in the lifetime of encoded states as a function of disorder strength. This effect has been attributed to a reduction of anyon diffusion due to the sites with positive onsite energy acting as barriers for the anyons.

Appendix

Derivatives of the Meyer-Wallach Entanglement Measure

Within our numerical framework, the evaluation of the Meyer-Wallach measure $\gamma(|\psi\rangle)$ [see Eq. (3.45)] requires its partial derivatives with respect to the real and imaginary components of $|\psi\rangle$ [see Eqs. (3.10, 3.11)]. They are given by

$$\left. \frac{\partial \gamma}{\partial \operatorname{Re} \psi^{(i)}} \right|_{|\psi\rangle} = -\frac{8}{N} \sum_{k=1}^N \sum_{\mu=0}^1 \operatorname{Re} \left(\psi^{(\nu_1, \nu_2, \dots, \nu_{k-1}, \mu, \nu_{k+1}, \dots, \nu_N)} \cdot \rho_k^{\nu_k, \mu} \right), \quad (\text{A.1})$$

$$\left. \frac{\partial \gamma}{\partial \operatorname{Im} \psi^{(i)}} \right|_{|\psi\rangle} = -\frac{8}{N} \sum_{k=1}^N \sum_{\mu=0}^1 \operatorname{Im} \left(\psi^{(\nu_1, \nu_2, \dots, \nu_{k-1}, \mu, \nu_{k+1}, \dots, \nu_N)} \cdot \rho_k^{\nu_k, \mu} \right). \quad (\text{A.2})$$

Here, we represented the i th component of $|\psi\rangle$ by the tuple $i = (\nu_1, \dots, \nu_N)$, with the indices $\nu_j \in \{0, 1\}$ corresponding to some arbitrary product basis $\{|\nu_1\rangle|\nu_2\rangle \cdots |\nu_N\rangle\}_{\nu_j=0}^1$ of the spin system. Furthermore, $\rho_k^{\nu, \mu}$ denotes the matrix element with indices (ν, μ) of the reduced density matrix

$$\rho_k = \operatorname{Tr}_{\nu_1, \nu_2, \dots, \nu_{k-1}, \nu_{k+1}, \dots, \nu_N} |\psi\rangle\langle\psi| \in \mathbb{C}^{2 \times 2}. \quad (\text{A.3})$$

In case of the systems studied in Sec. 3.4, the computation of the Meyer-Wallach measure (3.45) and its derivatives can be greatly simplified by exploiting the rotational symmetry of the Hamiltonian H . Since we have $[H, \mathcal{R}] = 0$, where \mathcal{R} is the symmetry operator for the rotation by an angle of $2\pi/N$ about the central axis perpendicular to the plane of the spin ring, all ρ_k in Eq. (3.45) are unitary equivalent for a simultaneous eigenstate $|\psi\rangle$ of H and \mathcal{R} . This reduces Eq. (3.45) to the simple form

$$\gamma(|\psi\rangle) = 2[1 - \operatorname{Tr}(\rho_1^2)]. \quad (\text{A.4})$$

The corresponding derivatives read

$$\left. \frac{\partial \gamma}{\partial \operatorname{Re} \psi^{(i)}} \right|_{|\psi\rangle} = -8[\rho_1^{0,0} \operatorname{Re} \psi^{(i)} + \operatorname{Re}(\rho_1^{0,1} \psi^{(2^{N-1}+i)})], \quad (\text{A.5})$$

$$\left. \frac{\partial \gamma}{\partial \operatorname{Im} \psi^{(i)}} \right|_{|\psi\rangle} = -8[\rho_1^{0,0} \operatorname{Im} \psi^{(i)} + \operatorname{Im}(\rho_1^{0,1} \psi^{(2^{N-1}+i)})], \quad (\text{A.6})$$

for $0 \leq i \leq 2^{N-1} - 1$, and

$$\left. \frac{\partial \gamma}{\partial \operatorname{Re} \psi^{(i)}} \right|_{|\psi\rangle} = -8[\rho_1^{1,1} \operatorname{Re} \psi^{(i)} + \operatorname{Re}(\rho_1^{0,1} \psi^{*(i-2^{N-1})})], \quad (\text{A.7})$$

$$\left. \frac{\partial \gamma}{\partial \operatorname{Im} \psi^{(i)}} \right|_{|\psi\rangle} = -8[\rho_1^{1,1} \operatorname{Im} \psi^{(i)} - \operatorname{Im}(\rho_1^{0,1} \psi^{*(i-2^{N-1})})], \quad (\text{A.8})$$

for $2^{N-1} \leq i \leq 2^N - 1$. In practice, we first diagonalize H numerically ^[1], subsequently diagonalize further any degenerate spaces with respect to \mathcal{R} , and then apply the simplified formulas above.

¹Since for the number of particles N considered in Sec. 3.4 the splitting between the lowest and the next higher multiplet is still always large compared with temperature, we diagonalize only the lowest-lying $(N + 1)$ -dimensional subspace of H using a Lanczos algorithm.

Derivatives of Entanglement Measures

In the following, we provide the calculations for the derivatives of all entanglement measures included in `libCreme`.

B.1 Entropy of entanglement

Let $|\Psi\rangle$ be a state vector from a bipartite system with subsystem dimensions d_1 and d_2 . Let us rewrite Eq. (4.1) in the form

$$E(|\Psi\rangle) = S(\text{Tr}_B \rho), \quad (\text{B.1})$$

where

$$S(X) = -\text{Tr} X \log X, \quad (\text{B.2})$$

and $\rho = |\Psi\rangle\langle\Psi|$. Let ψ be an arbitrary (complex) entry of the state vector $|\Psi\rangle$. Then, using the chain rule, we have

$$\frac{\partial E(|\Psi\rangle)}{\partial \psi} = \sum_{i,j,k,l} \frac{\partial S(X)}{X_{ij}} \Big|_{X=\text{Tr}_B \rho} \frac{\partial(\text{Tr}_B \rho)_{ij}}{\partial \rho_{kl}} \frac{\partial \rho_{kl}}{\partial \psi}. \quad (\text{B.3})$$

Note that the indices k and l in the above sum run over the full Hilbert space dimension $d_1 d_2$, whereas i and j only run over the first subsystem with dimension d_1 . We now evaluate each term in the sum separately.

For the gradient of $S(X)$ we get

$$\begin{aligned}
\nabla_X S(X) &= -\nabla_X \operatorname{Tr} [(X - \mathbb{I}) \log X + \log X] \\
&= -\nabla_X \left\{ \sum_{n=1}^{\infty} \frac{(-1)^{n+1}}{n} \operatorname{Tr} [(X - \mathbb{I})^{n+1}] \right. \\
&\quad \left. + \sum_{n=1}^{\infty} \frac{(-1)^{n+1}}{n} \operatorname{Tr} [(X - \mathbb{I})^n] \right\} \\
&= -\left\{ \sum_{n=1}^{\infty} \frac{(-1)^{n+1}(n+1)}{n} (X - \mathbb{I})^n \right. \\
&\quad \left. + \sum_{n=1}^{\infty} (-1)^{n+1} (X - \mathbb{I})^{n-1} \right\}^T \\
&= -\left\{ -\sum_{n=1}^{\infty} (\mathbb{I} - X)^n \right. \\
&\quad \left. + \sum_{n=1}^{\infty} \frac{(-1)^{n+1}}{n} (X - \mathbb{I})^n + \sum_{n=0}^{\infty} (\mathbb{I} - X)^n \right\}^T \\
&= -\log X^T - \mathbb{I},
\end{aligned}$$

where we have made use of the formula $\nabla_X \operatorname{Tr}(X^n) = n(X^{n-1})^T$ and the fact that the series expansion of the logarithm is valid because in our case X is always a density matrix, thus having real eigenvalues between 0 and 1.

Next we evaluate the derivatives of the partial trace Tr_B . We will write coordinate indices of vectors in the full Hilbert space as $k = (k_1 - 1)d_2 + k_2 \equiv [k_1, k_2]$, where $k_1 \in \{1, \dots, d_1\}$ and $k_2 \in \{1, \dots, d_2\}$. Then

$$(\operatorname{Tr}_B \rho)_{ij} = \sum_{k=1}^{d_2} \rho_{[i,k][j,k]} \quad (\text{B.4})$$

and thus

$$\begin{aligned}
\frac{\partial (\operatorname{Tr}_B \rho)_{ij}}{\partial \rho_{mn}} &= \sum_{k=1}^{d_2} \delta_{i,m_1} \delta_{k,m_2} \delta_{j,n_1} \delta_{k,n_2} \\
&= \delta_{i,m_1} \delta_{j,n_1} \delta_{m_2,n_2}.
\end{aligned}$$

Finally, we have to consider the derivatives of the density matrix itself with respect to the entries of the state vectors. This is the part where we have to treat $\operatorname{Re} \psi$ and $\operatorname{Im} \psi$ as independent variables because ρ is not

analytic in the entries of $|\Psi\rangle$. One quickly finds

$$\frac{\partial \rho_{kl}}{\partial \operatorname{Re} \psi_n} = \delta_{kn} \psi_l^* + \delta_{ln} \psi_k, \quad (\text{B.5})$$

$$\frac{\partial \rho_{kl}}{\partial \operatorname{Im} \psi_n} = i \delta_{kn} \psi_l^* - i \delta_{ln} \psi_k. \quad (\text{B.6})$$

Putting all this together we find, after eliminating all Kronecker δ -symbols,

$$\frac{\partial E(|\Psi\rangle)}{\partial \operatorname{Re} \psi_n} = \sum_{i=1}^{d_1} \{ [\nabla S(\rho)]_{n_1 i} \cdot \psi_{[i, n_2]}^* + [\nabla S(\rho)]_{i n_1} \cdot \psi_{[i, n_2]} \} \quad (\text{B.7})$$

and analogously for the derivatives with respect to the imaginary parts. Exploiting the fact that $\nabla S(\operatorname{Tr}_B \rho) = -\log(\operatorname{Tr}_B \rho)^T - \mathbb{I}$ is Hermitian, we arrive at the final expressions

$$\frac{\partial E(|\Psi\rangle)}{\partial \operatorname{Re} \psi_n} = 2 \sum_{i=1}^{d_1} \operatorname{Re} \{ [\nabla S(\operatorname{Tr}_B \rho)]_{i n_1} \cdot \psi_{[i, n_2]} \}, \quad (\text{B.8})$$

$$\frac{\partial E(|\Psi\rangle)}{\partial \operatorname{Im} \psi_n} = 2 \sum_{i=1}^{d_1} \operatorname{Im} \{ [\nabla S(\operatorname{Tr}_B \rho)]_{i n_1} \cdot \psi_{[i, n_2]} \}. \quad (\text{B.9})$$

B.2 Three-tangle

Defining $d = d_1 - 2d_2 + 4d_3$, where d_1, d_2, d_3 are given in Eqs. (4.3, 4.4, 4.5), it is easy to see that

$$\frac{\partial \tau(|\Psi\rangle)}{\partial \operatorname{Re} \psi_n} = \frac{4}{|d|} \operatorname{Re} \left(\frac{\partial d}{\partial \psi_n} \cdot d^* \right), \quad (\text{B.10})$$

$$\frac{\partial \tau(|\Psi\rangle)}{\partial \operatorname{Im} \psi_n} = -\frac{4}{|d|} \operatorname{Im} \left(\frac{\partial d}{\partial \psi_n} \cdot d^* \right). \quad (\text{B.11})$$

Note that the derivatives $\partial d / \partial \psi_n$ are well-defined because d is an analytic function of the elements ψ_n of $|\Psi\rangle$.

B.3 Meyer-Wallach measure

We start by calculating the derivative of $\gamma(|\Psi\rangle)$ with respect to an arbitrary complex element ψ of $|\Psi\rangle$ until the point where non-analyticities

appear:

$$\frac{\partial \gamma(|\Psi\rangle)}{\partial \psi} = -\frac{2}{N} \sum_{k=1}^N \sum_{j=1}^2 \frac{\partial}{\partial \psi} (\rho_k^2)_{jj} \quad (\text{B.12})$$

$$= -\frac{2}{N} \sum_{k=1}^N \sum_{j,l=1}^2 \frac{\partial}{\partial \psi} [(\rho_k)_{jl} (\rho_k)_{lj}] \quad (\text{B.13})$$

$$= -\frac{4}{N} \sum_{k=1}^N \sum_{j,l=1}^2 \text{Re} \left[(\rho_k^*)_{jl} \cdot \frac{\partial}{\partial \psi} (\rho_k)_{jl} \right] \quad (\text{B.14})$$

$$= -\frac{4}{N} \sum_{k=1}^N \sum_{j,l=1}^2 \text{Re} \left\{ (\rho_k^*)_{jl} \sum_{\alpha,\beta=1}^{2^N} \left[\frac{\partial (\rho_k)_{jl}}{\partial \rho_{\alpha\beta}} \cdot \frac{\partial \rho_{\alpha\beta}}{\partial \psi} \right] \right\}. \quad (\text{B.15})$$

The derivatives of the $\rho_{\alpha\beta}$ (depending non-analytically on ψ) with respect to the real and imaginary part of ψ have already been stated in Eqs. (B.5, B.6). We are thus left to calculate the slightly cumbersome derivatives of multiple partial traces of ρ with respect to the matrix elements $\rho_{\alpha\beta}$.

Similarly to the calculation in Sec. B.1, we will now rewrite indices $\nu \in \{1, \dots, 2^N\}$ of the full Hilbert space in the binary representation $\nu = (\nu_1 - 1)2^{N-1} + (\nu_2 - 1)2^{N-2} + \dots + 2\nu_{N-1} + \nu_N \equiv [\nu_1, \nu_2, \dots, \nu_N]$, where $\nu_i \in \{1, 2\}$ for all $i \in 1, \dots, N$ (we will also employ this representation for the indices α, β , and n below). Then, the matrix elements of ρ_k can be written as

$$(\rho_k)_{i,j} = \sum_{\nu_1} \sum_{\nu_2} \cdots \sum_{\nu_{k-1}} \sum_{\nu_{k+1}} \cdots \sum_{\nu_N} \rho_{[\nu_1, \nu_2, \dots, \nu_{k-1}, i, \nu_{k+1}, \dots, \nu_N]} [\nu_1, \nu_2, \dots, \nu_{k-1}, j, \nu_{k+1}, \dots, \nu_N], \quad (\text{B.16})$$

where $i, j \in \{1, 2\}$. Hence we have

$$\frac{\partial (\rho_k)_{jl}}{\partial \rho_{\alpha\beta}} = \delta_{\alpha_1 \beta_1} \cdot \delta_{\alpha_2 \beta_2} \cdots \delta_{\alpha_{k-1} \beta_{k-1}} \cdot \delta_{\alpha_k, j} \cdot \delta_{\beta_k, l} \cdot \delta_{\alpha_{k+1} \beta_{k+1}} \cdots \delta_{\alpha_N \beta_N}. \quad (\text{B.17})$$

Inserting this into Eq. (B.15) and working out all Kronecker δ symbols, we arrive at

$$\left. \frac{\partial \gamma}{\partial \text{Re } \psi_n} \right|_{|\psi\rangle} = -\frac{8}{N} \sum_{k=1}^N \sum_{j=1}^2 \text{Re} \left(\psi_{[n_1, n_2, \dots, n_{k-1}, j, n_{k+1}, \dots, n_N]} \cdot (\rho_k)_{n_k, j} \right), \quad (\text{B.18})$$

$$\left. \frac{\partial \gamma}{\partial \text{Im } \psi_n} \right|_{|\psi\rangle} = -\frac{8}{N} \sum_{k=1}^N \sum_{j=1}^2 \text{Im} \left(\psi_{[n_1, n_2, \dots, n_{k-1}, j, n_{k+1}, \dots, n_N]} \cdot (\rho_k)_{n_k, j} \right). \quad (\text{B.19})$$

Derivatives of the Function $h(U)$

We will carry out the calculation explicitly only for the derivatives with respect to the real part of U , but everything works analogously for the imaginary part. For the sake of readability, we will drop the usual ‘ket’ notation and write quantum state vectors as $\psi_i \equiv |\psi_i\rangle$. We write the k th element of ψ_i as $\psi_i^{(k)}$.

Differentiating Eq. (4.15) with respect to the real part of the $k \times r$ matrix U (with matrix elements $U_{\alpha\beta}$) yields

$$\frac{\partial h(U)}{\partial \operatorname{Re} U_{\alpha\beta}} = \sum_{i=1}^k \left\{ \frac{\partial p_i(U)}{\partial \operatorname{Re} U_{\alpha\beta}} m(\psi_i(U)) + p_i(U) \sum_{j=1}^d \frac{\partial m(\psi)}{\partial \psi^{(j)}} \Big|_{\psi=\psi_i} \frac{\partial \psi_i^{(j)}}{\partial \operatorname{Re} U_{\alpha\beta}} \right\}, \quad (\text{C.1})$$

where d is the dimension of the total Hilbert space. Note that we have specifically emphasized the U -dependence of the p_i and ψ_i via Eqs. (4.9, 4.10, 4.11, 4.12). The first derivative in this expression is given by

$$\begin{aligned} \frac{\partial p_i}{\partial \operatorname{Re} U_{\alpha\beta}} &= \sum_j \left(\frac{\partial \tilde{\psi}_i^{(j)*}}{\partial \operatorname{Re} U_{\alpha\beta}} \cdot \tilde{\psi}_i^{(j)} + \tilde{\psi}_i^{(j)*} \cdot \frac{\partial \tilde{\psi}_i^{(j)}}{\partial \operatorname{Re} U_{\alpha\beta}} \right) \\ &= 2 \sum_j \operatorname{Re} \left(\tilde{\psi}_i^{(j)*} \cdot \frac{\partial \tilde{\psi}_i^{(j)}}{\partial \operatorname{Re} U_{\alpha\beta}} \right) \\ &= 2 \sum_j \operatorname{Re} \left(\tilde{\psi}_i^{(j)*} \delta_{i\alpha} \sqrt{\lambda_\beta} \chi_\beta^{(j)} \right) \\ &= 2 \delta_{i\alpha} \lambda_\beta \operatorname{Re} \left(\sum_{l=1}^r U_{il}^* \sum_j \chi_l^{(j)*} \chi_\beta^{(j)} \right) \\ &= 2 \delta_{i\alpha} \lambda_\beta \operatorname{Re} (U_{i\beta}), \end{aligned} \quad (\text{C.2})$$

where we have used in the last step the orthonormality of the χ_i and the fact that $\operatorname{Re} c^* = \operatorname{Re} c$ for any complex number c .

As for the derivatives of the state vector, we obtain

$$\begin{aligned}
\frac{\partial \psi_i^{(j)}}{\partial U_{\alpha\beta}} &= \frac{1}{\sqrt{p_i}} \frac{\partial \tilde{\psi}_i^{(j)}}{\partial U_{\alpha\beta}} - \frac{1}{2} p_i^{-3/2} \frac{\partial p_i}{\partial U_{\alpha\beta}} \\
&= \frac{1}{\sqrt{p_i}} \delta_{i\alpha} \sqrt{\lambda_\beta} \chi_\beta^{(j)} - p_i^{-3/2} \delta_{i\alpha} \lambda_\beta \operatorname{Re}(U_{i\beta}) \tilde{\psi}_i^{(j)} \\
&= \delta_{i\alpha} \left[\sqrt{\frac{\lambda_\beta}{p_i}} \chi_\beta^{(j)} - \frac{\lambda_\beta}{p_i} \operatorname{Re}(U_{i\beta}) \psi_i^{(j)} \right] \\
&\equiv \delta_{i\alpha} \xi_{i\beta}^{(j)}.
\end{aligned} \tag{C.3}$$

We can now insert Eqs. (C.2) and (C.3) into (C.1). The final result (including the derivatives with respect to the imaginary part of U from an analogous calculation) reads

$$\begin{aligned}
\frac{\partial h(U)}{\partial \operatorname{Re} U_{\alpha\beta}} &= 2\lambda_\beta \operatorname{Re}(U_{\alpha\beta}) m(\psi_\alpha(U)) \\
&\quad + p_\alpha(U) \sum_{j=1}^d \left[\operatorname{Re} \xi_{\alpha\beta}^{(j)} \frac{\partial m(\psi)}{\partial \operatorname{Re} \psi^{(j)}} \Big|_{\psi=\psi_k} + \operatorname{Im} \xi_{\alpha\beta}^{(j)} \frac{\partial m(\psi)}{\partial \operatorname{Im} \psi^{(j)}} \Big|_{\psi=\psi_k} \right],
\end{aligned} \tag{C.4}$$

$$\begin{aligned}
\frac{\partial h(U)}{\partial \operatorname{Im} U_{\alpha\beta}} &= 2\lambda_\beta \operatorname{Im}(U_{\alpha\beta}) m(\psi_\alpha(U)) \\
&\quad + p_\alpha(U) \sum_{j=1}^d \left[\operatorname{Re} \zeta_{\alpha\beta}^{(j)} \frac{\partial m(\psi)}{\partial \operatorname{Re} \psi^{(j)}} \Big|_{\psi=\psi_k} + \operatorname{Im} \zeta_{\alpha\beta}^{(j)} \frac{\partial m(\psi)}{\partial \operatorname{Im} \psi^{(j)}} \Big|_{\psi=\psi_k} \right],
\end{aligned} \tag{C.5}$$

where

$$\xi_{\alpha\beta}(U) = \left[\sqrt{\frac{\lambda_\beta}{p_\alpha(U)}} \chi_\beta - \frac{\lambda_\beta}{p_\alpha(U)} \operatorname{Re}(U_{\alpha\beta}) \psi_\alpha(U) \right], \tag{C.6}$$

$$\zeta_{\alpha\beta}(U) = \left[\mathbf{i} \sqrt{\frac{\lambda_\beta}{p_\alpha(U)}} \chi_\beta - \frac{\lambda_\beta}{p_\alpha(U)} \operatorname{Im}(U_{\alpha\beta}) \psi_\alpha(U) \right]. \tag{C.7}$$

Self-Correcting Quantum Memories

D.1 Mapping from lattice gas to Ising model

Note that H_0 in Eq. (5.1) has the general form of two independent lattice gases, which are in turn equivalent to two Ising spin lattices. We explicitly perform the transformation in the plaquette sector by identifying the Ising variables $s_p \equiv 1 - 2n_p$, yielding

$$H_0 = - \sum_p \left(\frac{J}{2} + \sum_{p'}' \frac{U_{pp'}}{4} \right) s_p + \frac{1}{8} \sum_{p,p'}' U_{pp'} s_p s_{p'} + \dots, \quad (\text{D.1})$$

where $U_{pp'}$ is given in Eq. (5.2) and the primes in the summations indicate $p' \neq p$. We have used $U_{pp} = 2J$ and $U_{pp'} = U_{p'p}$. The noninteracting Kitaev model corresponds to noninteracting spins in an external magnetic field. The ground state corresponds to the fully polarized state $s_p = 1$ for all p , where no anyon is present. However, for $T > 0$ a finite density of anyons emerges and is sufficient to destroy the information stored in the memory.

If a short-range ferromagnetic interaction is introduced, ordering of the system is spontaneously favored below some critical temperature. A higher magnetization corresponds to a lower population of anyons and improves the lifetime. However, short range interactions do not improve the scaling of the lifetime with the system size, since a residual density of anyons is left at any finite temperature. As in the noninteracting case, a finite density of excited plaquettes efficiently destroys the stored quantum information, in agreement with the general analysis of [BT09, KC08]. Instead, repulsive long-range interactions lead to a fully polarized system at a given temperature for sufficiently large system size L .

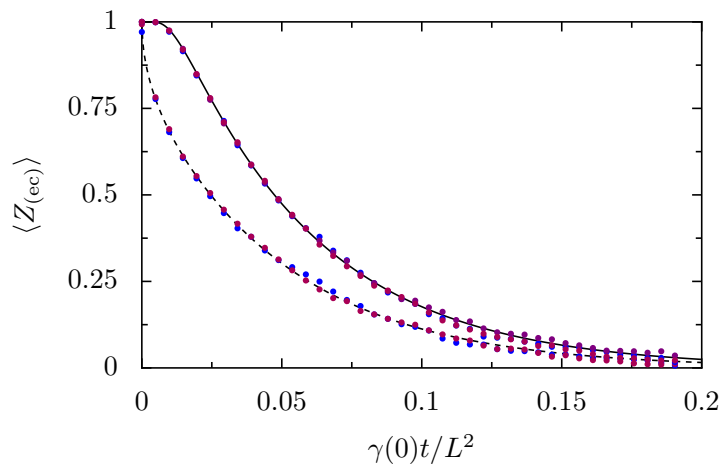


Figure D.1: (Color online.) Decay of the bare and corrected expectation value of Z due to a single pair of anyons in the memory. The dots show numerical data (averaged over 10^4 samples) while the two curves are the continuum limit expressions Eq. (D.4) and (D.6) for $\langle Z_{ec} \rangle$ (solid) and $\langle Z \rangle$ (dashed). The numerical data have been obtained for $L = 32, 64, 128$. All points collapse onto each other when plotted as a function of $\gamma(0)t/L^2$.

D.2 Lifetime in the presence of a single pair

The decay of the bare and logical Z operators is most simply illustrated by assuming only a single anyon pair in the memory. We set $\gamma(2J) = 0$, so that pair creation and annihilation are not allowed. If no anyons were present, the initial values $\langle Z \rangle = \langle Z_{ec} \rangle = 1$ would be stable. We apply one σ_x -operation at a randomly chosen site and thereby create two neighboring anyons at $t = 0$. This causes a partial decay of the bare logical operator already at $t = 0$, since we might have chosen to flip a spin on the logical Z operator, yielding $\langle Z \rangle = 1 - \frac{1}{L}$. This has been used in the main text in the discussion of the nonsplit-pair regime.

We now study the decay for $t > 0$ in the continuum limit and therefore neglect the $1/L$ correction at $t = 0$. We consider a single pair of diffusing anyons with coordinates (x_1, y_1) and (x_2, y_2) created at the origin. We then assume that the probability to find an anyon at position \mathbf{r} is described by the probability density

$$p(\mathbf{r}) = \frac{1}{4\pi\gamma(0)t} e^{-\frac{r^2}{4\gamma(0)t}}. \quad (\text{D.2})$$

We represent the torus as an infinite plane with the points (x, y) and $(x + mL, y + nL)$ being equivalent ($m, n \in \mathbb{Z}$). The logical Z operator is then represented by parallel lines at $y_Z = L/2 + nL$. The two anyons diffuse along y with probability density $p(y_i - y_0) = e^{-(y_i - y_0)^2/4\gamma(0)t} / \sqrt{4\pi\gamma(0)t}$, where $i = 1, 2$ and the initial (random) coordinate satisfies $-L/2 \leq y_0 <$

$L/2$. The average of the logical operator at time t is

$$\langle Z \rangle = \int_{-L/2}^{L/2} \frac{dy_0}{L} \int dy_1 dy_2 p(y_1 - y_0) p(y_2 - y_0) z(y_1, y_2), \quad (\text{D.3})$$

where $z(y_1, y_2)$ gives the sign of Z if the two anyons have diffused to the coordinates y_1 and y_2 . Since Z changes sign each time an anyon crosses the lines at y_Z , we have $z(y_1, y_2) = z(y_1)z(y_2)$ where $z(y) = 1$ if $-L/2 + 2nL \leq y < L/2 + 2nL$ and -1 otherwise ($n \in \mathbb{Z}$). Therefore we can write

$$\langle Z \rangle = \int_{-1/2}^{1/2} dz_0 f(z_0)^2, \quad (\text{D.4})$$

where we have made the change of variables $y_0 = Lz_0$, such that

$$f(z_0) = \frac{1}{2} \sum_{n=-\infty}^{+\infty} (-1)^n \left[\operatorname{erf} \left(\frac{2z_0 + 2n + 1}{4\sqrt{\gamma(0)t/L^2}} \right) - \operatorname{erf} \left(\frac{2z_0 + 2n - 1}{4\sqrt{\gamma(0)t/L^2}} \right) \right]. \quad (\text{D.5})$$

We now consider the average of the error-corrected logical operator Z_{ec} . In this case, only the distance $y_{12} = y_1 - y_2$ between the two anyons is important since the value of Z_{ec} is 1 if $-L/2 + 2nL \leq y_{12} < L/2 + 2nL$, and is -1 otherwise. The probability distribution for y_{12} is $\int dy_2 p(y_{12} - y_2) p(y_2) = e^{-y_{12}^2/8\gamma(0)t} / \sqrt{8\pi\gamma(0)t}$, which gives

$$\langle Z_{\text{ec}} \rangle = \sum_{n=-\infty}^{+\infty} (-1)^n \operatorname{erf} \left(\frac{2n + 1}{2\sqrt{2\gamma(0)t/L^2}} \right). \quad (\text{D.6})$$

Both functions (D.4) and (D.6) are plotted in Fig. D.1 and show perfect agreement with the numerical simulation. An important feature of the above analytical expressions is that the time dependence only enters through the combination $\gamma(0)t/L^2$, which makes it possible to scale curves from different system sizes and diffusion constants onto each other.

D.3 Effective Hamiltonian via Schrieffer-Wolff transformation

In order to find an effective Hamiltonian for Eq. (5.17), we write $H = H_0 + V$, where $H_0 = \sum_{i=1}^2 \omega_i a_i^\dagger a_i$ and $V = \sum_p g_p n_p (a_1^\dagger a_2 + a_1 a_2^\dagger)$, and treat V as a small perturbation. The general expression for the Schrieffer-Wolff transformation of H up to second order in V reads

$$H_{\text{eff}} = H_0 + \frac{i}{2} \lim_{\varepsilon \rightarrow 0} \int_0^\infty dt e^{-\varepsilon t} [V, V(t)] + \mathcal{O}(V^3), \quad (\text{D.7})$$

where $V(t) = \exp(iH_0t)V \exp(-iH_0t)$, which yields in our case

$$V(t) = \sum_p g_p n_p \left(e^{i(\omega_1 - \omega_2)t} a_1^\dagger a_2 + e^{-i(\omega_1 - \omega_2)t} a_2^\dagger a_1 \right). \quad (\text{D.8})$$

With this, the commutator in Eq. (D.7) evaluates to

$$[V, V(t)] = 2i \left(\sum_p g_p n_p \right)^2 (a_2^\dagger a_2 - a_1^\dagger a_1) \sin(\omega_1 - \omega_2)t. \quad (\text{D.9})$$

Inserting this into Eq. (D.7) and performing the integral yields Eq. (5.23).

Critical Fraction of Random Lattices in Contact with an Ohmic Bath

We present here some additional results for the error thresholds of random lattices in the presence of thermal errors. Fig. E.1 shows the fraction of errors f at the lifetime of an infinitely large system as a function of the lattice mixing p_{mix} and for different temperatures T . In this section, the energy scale is set by the anyon gap J . Time is thus measured in units of $(\kappa_1 J)^{-1}$. For given p_{mix} and temperature T , we first simulate systems of several different sizes in contact with an Ohmic bath. We then determine the lifetime τ as the intersection of the decay curves of the corresponding error-corrected logical Z operators (see inset of Fig. E.1). Since the anyon dynamics are independent of the system size (note that the anyons are not interacting with each other), all curves $f(t)$ for different system sizes collapse and the specific value $f(t = \tau) = f_{cr}$ can be read off easily. One can see nicely that these thresholds converge with increasing temperature to the ones given by the model of independent errors. This can be explained by the loss of correlations between errors due to an increasing amount of thermal noise in the form of fluctuating anyons.

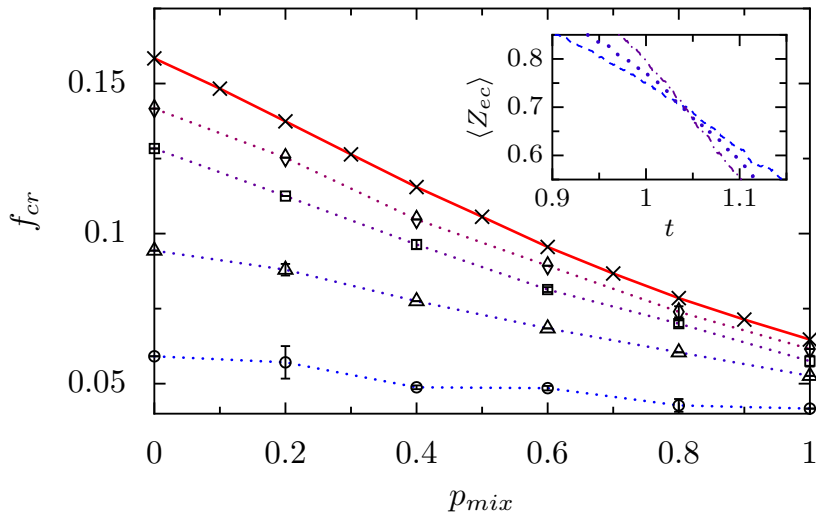


Figure E.1: (color online) Critical fraction of errors $f_{cr} = f(t = \tau)$ as a function of lattice mixing p_{mix} at temperatures $T = 0.2J$ (circles), $0.45J$ (triangles), $1.0125J$ (squares), and $2J$ (diamonds). The lifetime τ is given by the intersection of error-corrected logical Z operators for lattice sizes $L = 38, 56, 86$. Error bars are due to the uncertainty in τ . The solid line is determined by the thresholds from the Monte Carlo simulations of an independent error model (see main text). The inset shows an example of crossing logical Z operators for the particular values $p_{mix} = 0.4$ and $T = 0.45J$.

Gaussian Noise and $1/r$ Interaction

We have also performed simulations with $1/r$ interaction ($\alpha = 1$) and plot the results in Fig. F.1. Apart from Ising-like disorder ($J_p = \pm\sigma$) we have also looked at a Gaussian distribution of onsite potentials J_p with mean zero and standard deviation σ . Generally, the lifetimes are shorter than for constant interaction because the weaker $1/r$ interaction allows for a larger density of anyons. Nevertheless, the results are qualitatively similar to the ones discussed in the main text, namely showing a pronounced maxima of the lifetime as a function of σ . This supports the picture that the interaction is required to limit the number of diffusing anyons, while the initial increase in lifetime with σ is due to their obscured diffusion. In the case of Gaussian noise, the latter effect is even stronger, because anyons are created or get trapped in a few sites with onsite potentials much lower than $-\sigma$, out of which it is difficult for them to escape again. This explains the increased lifetime from Ising to Gaussian randomness.

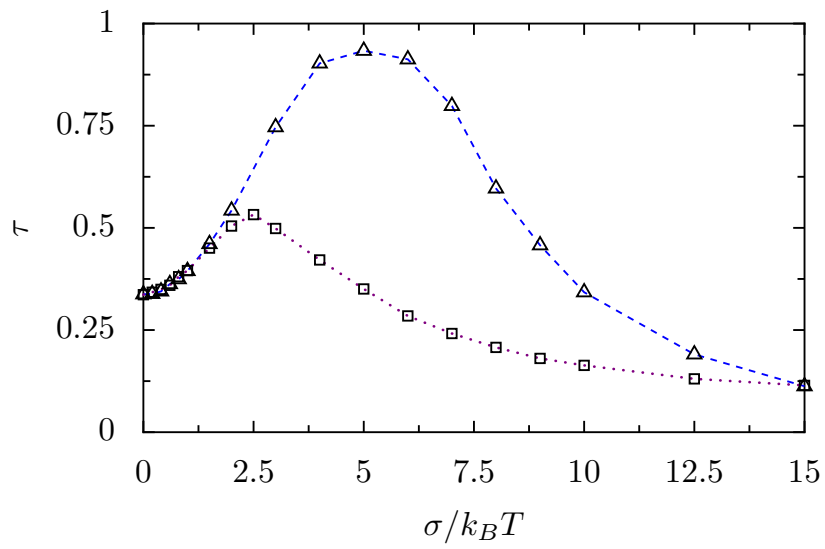


Figure F.1: (color online) Lifetime τ as a function of disorder strength σ in the presence of Gaussian (triangles) and Ising (squares) noise in an interacting system with $\alpha = 1$, $A = 0.5 k_B T$. The lines are guides to the eye. The size of this particular system was $L = 32$.

Supporting Simulations

G.1 Polarized Ising randomness

In order to confirm the picture that it is indeed the sites with $J_p > 0$ that restrict the diffusion by acting as barriers to the anyons, we have determined the lifetime τ of an interacting system ($L = 50$, $\alpha = 0$, $A = 0.5 k_B T$, $\sigma = 5 k_B T$) as a function of the Ising polarization P . The latter is defined as $P = 1 - 2\eta$, where η is the fraction of sites with negative onsite energy.

Starting from $P = -1$, i.e., $J_p = -\sigma$ for all sites p , the lifetime moderately increases as more and more positive sites are randomly added (increasing P), as can be seen in Fig. G.1. Around $P = 0$, where there is an equal number of sites with positive and negative onsite energies, the lifetime drastically increases by about 2 orders of magnitude. At this point, large connected areas of sites with $J_p < 0$ can no longer exist, such that the anyons can move freely only within areas each consisting of just a few negative sites. Consequently, the diffusion is drastically reduced. If and how the polarization at this threshold is related to the site and bond percolation thresholds of the square lattice, which are $\eta \approx 0.5927$ and 0.5 (see, e.g., Ref. [FDB08]), respectively, is not completely clear at the time of writing and remains the subject of future research.

G.2 Artificial cutoff of number of anyons

We can support the claim that the only relevant effect of the repulsive interaction is to reduce the number of anyons by simulating a non-interacting system with an artificial maximal number of anyons. This data is shown in Fig. G.2. Despite the absence of interaction, the lifetime of encoded states is still growing with increasing Ising disorder strength, hence clearly demonstrating that this effect is caused solely by the disorder.

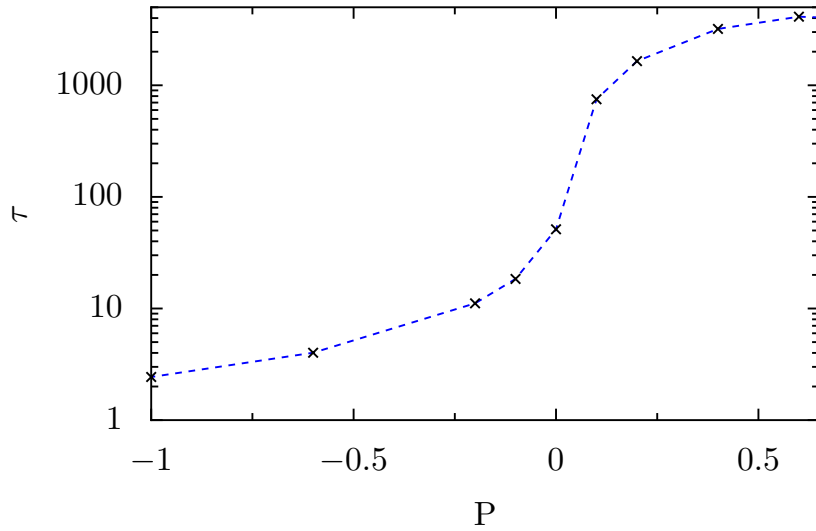


Figure G.1: (color online) Lifetime as a function of Ising polarization P . The parameters for these systems are $L = 50$, $\alpha = 0$, $A = 0.5 k_B T$, $\sigma = 5 k_B T$. The dashed line is a guide to the eye.

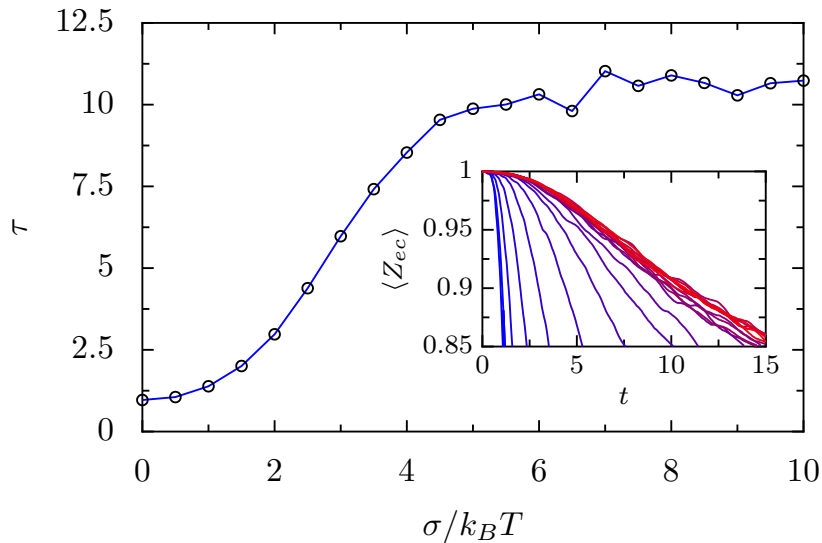


Figure G.2: (color online) Lifetime as a function of Ising disorder strength in a non-interacting system of size $L = 32$ with an artificially engineered maximal number of anyons equal to 20. The solid line is a guide to the eye. Inset: The error-corrected logical Z operator as a function of time for different σ yielding the lifetimes shown in the main plot.

der. Furthermore, the lifetime saturates for large σ , because the energy barriers posed by the sites with $J_p = +\sigma$ are essentially infinitely high and increasing them further bears no more advantage. The observed sat-

uration also confirms that it is indeed the growing number of anyons that is responsible for the subsequent decrease in lifetime at large σ in the data presented in the main text (where the number of anyons was not artificially restricted).

Bibliography

- [AFH09] R. Alicki, M. Fannes, and M. Horodecki. *On thermalization in Kitaev's 2D model*. J. Phys. A **42**, 065303 (2009).
- [AFOV08] L. Amico, R. Fazio, A. Osterloh, and V. Vedral. *Entanglement in many-body systems*. Rev. Mod. Phys. **80**, 517 (2008).
- [AGR81] A. Aspect, P. Grangier, and G. Roger. *Experimental tests of realistic local theories via Bell's theorem*. Phys. Rev. Lett., **47**, 460 (1981).
- [AGR82] A. Aspect, P. Grangier, and G. Roger. *Experimental realization of Einstein-Podolsky-Rosen-Bohm gedankenexperiment: A new violation of Bell's inequalities*. Phys. Rev. Lett. **49**, 91 (1982).
- [AMR⁺08] S. Amasha, K. MacLean, Iuliana P. Radu, D. M. Zumbühl, M. A. Kastner, M. P. Hanson, and A. C. Gossard. *Electrical control of spin relaxation in a quantum dot*. Phys. Rev. Lett. **100**, 046803 (2008).
- [AMS08] P.-A. Absil, R. Mahony, and R. Sepulchre. *Optimization Algorithms on Matrix Manifolds*. Princeton University Press, Princeton, New Jersey, 2008.
- [And58] P. W. Anderson. *Absence of diffusion in certain random lattices*. Phys. Rev. **109**, 1492 (1958).
- [AVDM01] K. Audenaert, F. Verstraete, and B. De Moor. *Variational characterizations of separability and entanglement of formation*. Phys. Rev. A **64**, 052304 (2001).
- [Bac06] D. Bacon. *Operator quantum error-correcting subsystems for self-correcting quantum memories*. Phys. Rev. A **73**, 012340 (2006).
- [BBPS96] C. H. Bennett, H. J. Bernstein, S. Popescu, and B. Schumacher. *Concentrating partial entanglement by local operations*. Phys. Rev. A **53**, 2046 (1996).
- [BC08] J. Batle and M. Casas. *Int. J. Quantum Inf.* **6**, 237 (2008).

- [BDLT08] S. Bravyi, D. P. DiVincenzo, D. Loss, and B. M. Terhal. *Quantum simulation of many-body hamiltonians using perturbation theory with bounded-strength interactions*. Phys. Rev. Lett. **101**, 070503 (2008).
- [BDSW96] C. H. Bennett, D. P. DiVincenzo, J. A. Smolin, and W. K. Wootters. *Mixed-state entanglement and quantum error correction*. Phys. Rev. A **54**, 3824 (1996).
- [Bel64] J. Bell. *On the Einstein Podolsky Rosen paradox*. Physics **1**, 195 (1964).
- [BHM10] S. Bravyi, M. B. Hastings, and S. Michalakis. *Topological quantum order: Stability under local perturbations*. J. Math. Phys. **51**, 093512 (2010).
- [BI06] G. Burkard and A. Imamoglu. *Ultra-long-distance interaction between spin qubits*. Phys. Rev. B **74**, 041307 (2006).
- [BK98] S. B. Bravyi and A. Yu. Kitaev. *Quantum codes on a lattice with boundary*. online preprint, quant-ph/9810055 (1998).
- [BK11] S. Bravyi and R. Koenig. *Disorder-assisted error correction in majorana chains*. online preprint arXiv:1108.3845 (2011).
- [Bos03] S. Bose. *Quantum communication through an unmodulated spin chain*. Phys. Rev. Lett. **91**, 207901 (2003).
- [BPB⁺07] A. Borrás, A. R. Plastino, J. Batle, C. Zander, M. Casas, and A. Plastino. *Multiqubit systems: highly entangled states and entanglement distribution*. J. Phys. A **40**, 13407 (2007).
- [BR01] H. J. Briegel and R. Raussendorf. *Persistent entanglement in arrays of interacting particles*. Phys. Rev. Lett. **86**, 910 (2001).
- [Bre03] G. K. Brennen. *An observable measure of entanglement for pure states of multi-qubit systems*. Quant. Inf. Comp. **3**, 619 (2003).
- [BT09] S. Bravyi and B. Terhal. *A no-go theorem for a two-dimensional self-correcting quantum memory based on stabilizer codes*. New J. Phys. **11**, 043029 (2009).
- [CCGL05] V. Cerletti, W. A. Coish, O. Gywat, and D. Loss. *Recipes for spin-based quantum computing*. Nanotechnology **16**, R27 (2005).
- [CEMM98] R. Cleve, A. Ekert, C. Macchiavello, and M. Mosca. *Quantum algorithms revisited*. Proc. R. Soc. London, Ser. A **454**, 339 (1998).

- [CKW00] V. Coffman, J. Kundu, and W. K. Wootters. *Distributed entanglement*. Phys. Rev. A **61**, 052306 (2000).
- [CLBT09] S. Chesi, D. Loss, S. Bravyi, and B. M. Terhal. *Thermodynamic stability criteria for a quantum memory based on stabilizer and subsystem codes*. New J. Phys. **12**, 025013 (2010).
- [CRL10] S. Chesi, B. Röthlisberger, and D. Loss. *Self-correcting quantum memory in a thermal environment*. Phys. Rev. A **82**, 022305 (2010).
- [CS96] A. R. Calderbank and P. W. Shor. *Good quantum error-correcting codes exist*. Phys. Rev. A **54**, 1098 (1996).
- [Dav74] E. B. Davies. *Markovian master equations*. Comm. Math. Phys. **39**, 91 (1974).
- [Deu85] D. Deutsch. *Quantum theory, the church-turing principle and the universal quantum computer*. Proc. R. Soc. London, Ser. A **400**, 97 (1985).
- [Dic54] R. H. Dicke. *Coherence in spontaneous radiation processes*. Phys. Rev. **93**, 99 (1954).
- [DiV00] D. P. DiVincenzo. *The physical implementation of quantum computers*. Fortschr. Phys., **48**, 771 (2000).
- [DJ92] D. Deutsch and R. Jozsa. *Rapid solutions of problems by quantum computation*. Proc. R. Soc. London, Ser. A **439**, 553 (1992).
- [DKLP02] E. Dennis, A. Kitaev, A. Landahl, and J. Preskill. *Topological quantum memory*. J. Math. Phys. **43**, 4452 (2002).
- [DKOSV11] S. Dusuel, M. Kamfor, R. Orus, K. P. Schmidt, and J. Vidal. *Robustness of a perturbed topological phase*. Phys. Rev. Lett. **106**, 107203 (2011).
- [DL05] D. P. DiVincenzo and D. Loss. *Rigorous born approximation and beyond for the spin-boson model*. Phys. Rev. B **71**, 035318 (2005).
- [DVC00] W. Dür, G. Vidal, and J. I. Cirac. *Three qubits can be entangled in two inequivalent ways*. Phys. Rev. A **62**, 062314 (2000).
- [EAS98] A. Edelman, T. A. Arias, and S. T. Smith. *The geometry of algorithms with orthogonality constraints*. SIAM J. Matrix Anal. Appl. **20**, 303 (1998).

- [EB04] C. Emary and C. W. J. Beenakker. *Relation between entanglement measures and Bell inequalities for three qubits*. Phys. Rev. A **69**, 032317 (2004).
- [EBaA07] J. Eisert, F. G. S. L. Brandão, and K. M. R. Audenaert. *Quantitative entanglement witnesses*. New J. Phys. **9**, 46 (2007).
- [Edm65] J. Edmonds. *Paths, trees, and flowers*. Can. J. Math. **17**, 449 (1965).
- [EPR35] A. Einstein, B. Podolsky, and N. Rosen. *Can quantum-mechanical description of physical reality be considered complete?* Phys. Rev. **47**, 777 (1935).
- [Eul87] L. Euler. *Problema algebraicum ob affectiones prorsus singulares memorabile*. In *Opera Omnia, series I, vol. VI*. Birkhäuser, Basel, 1987.
- [FDB08] X. Feng, Y. Deng, and H. W. J. Blöte. *Percolation transitions in two dimensions*. Phys. Rev. E **78**, 031136 (2008).
- [FJ05] S.-M. Fei and N. Jing. *Equivalence of quantum states under local unitary transformations*. Physics Letters A **342**, 77 (2005).
- [Fey82] R. P. Feynman. *Simulating physics with computers*. Int. J. Theor. Phys. **21**, 467 (1982).
- [Fey86] R. P. Feynman. *Quantum mechanical computers*. Found. Phys. **16**, 507 (1986).
- [Fle00] R. Fletcher. *Practical Methods of Optimization*. Wiley, 2000.
- [FM01] M. H. Freedman and D. A. Meyer. *Projective plane and planar quantum codes*. Found. Comput. Math. **1**, 325 (2001).
- [GHZ89] D. M. Greenberger, M. Horne, and A. Zeilinger. *Bell's Theorem, Quantum Theory, and Conceptions of the Universe*. Kluwer Academic Publishers, Dordrecht, 1989.
- [GKL04] V. N. Golovach, A. Khaetskii, and D. Loss. *Phonon-induced decay of the electron spin in quantum dots*. Phys. Rev. Lett. **93**, 016601 (2004).
- [GL03] D. Gottesman and H.-K. Lo. *Proof of security of quantum key distribution with two-way classical communications*. IEEE Trans. Inform. Theory **49**, 457 (2003).
- [Got97] D. Gottesman. *Stabilizer Codes and Quantum Error Correction*. PhD thesis, California Institute of Technology, 1997. See also: Phys. Rev. A **57**, 127 (1998).

- [Got10] D. Gottesman. *An introduction to quantum error correction and fault-tolerant quantum computation*. In *Quantum Information Science and Its Contributions to Mathematics*, volume 68 of *Proceedings of Symposia in Applied Mathematics*, page 13. Amer. Math. Soc., Providence, Rhode Island, 2010.
- [Gro96] L. K. Grover. *A fast quantum mechanical algorithm for database search*. In *Proceedings, 28th Annual ACM Symposium on the Theory of Computing*, page 212, 1996.
- [GRW07] O. Gühne, M. Reimpell, and R. F. Werner. *Estimating entanglement measures in experiments*. *Phys. Rev. Lett.* **98**, 110502 (2007).
- [GVL96] G. H. Golub and C. F. Van Loan. *Matrix Computations*. Johns Hopkins University Press, Baltimore (1996).
- [HCC09] A. Hamma, C. Castelnovo, and C. Chamon. *Toric-boson model: Toward a topological quantum memory at finite temperature*. *Phys. Rev. B* **79**, 245122 (2009).
- [HHH96] M. Horodecki, P. Horodecki, and R. Horodecki. *Separability of mixed states: necessary and sufficient conditions*. *Phys. Lett. A* **223**, 1 (1996).
- [HHHH09] R. Horodecki, P. Horodecki, M. Horodecki, and K. Horodecki. *Quantum entanglement*. *Rev. Mod. Phys.* **81**, 865 (2009).
- [HJW93] L. P. Hughston, R. Jozsa, and W. K. Wootters. *A complete classification of quantum ensembles having a given density matrix*. *Phys. Lett. A* **183**, 14 (1993).
- [HKP⁺07] R. Hanson, L. P. Kouwenhoven, J. R. Petta, S. Tarucha, and L. M. K. Vandersypen. *Spins in few-electron quantum dots*. *Rev. Mod. Phys.* **79**, 1217 (2007).
- [Hur33] A. Hurwitz. *Über die Erzeugung der Invarianten durch Integration*. In *Mathematische Werke, vol. II*. Birkhäuser, Basel, 1933.
- [IAB⁺99] A. Imamoglu, D. D. Awschalom, G. Burkard, D. P. DiVincenzo, D. Loss, M. Sherwin, and A. Small. *Quantum information processing using quantum dot spins and cavity qed*. *Phys. Rev. Lett.* **83**, 4204 (1999).
- [IPGAP09] S. Iblisdir, D. Pérez-García, M. Aguado, and J. Pachos. *Scaling law for topologically ordered systems at finite temperature*. *Phys. Rev. B* **79**, 134303 (2009).

- [IPGAP10] S. Iblisdir, D. Pérez-García, M. Aguado, and J. Pachos. *Thermal states of anyonic systems*. Nucl. Phys. B **829**, 401 (2010).
- [JBG⁺08] L. Jiang, G. K. Brennen, A. V. Gorshkov, K. Hammerer, M. Hafezi, E. Demler, M. D. Lukin, and P. Zoller. *Anyonic interferometry and protected memories in atomic spin lattices*. Nature Physics **4**, 482 (2008).
- [JF08] S. P. Jordan and E. Farhi. *Perturbative gadgets at arbitrary orders*. Phys. Rev. A **77**, 062329 (2008).
- [Kay09] A. Kay. *Nonequilibrium reliability of quantum memories*. Phys. Rev. Lett. **102**, 070503 (2009).
- [KC08] A. Kay and R. Colbeck. *Quantum self-correcting stabilizer codes*. Online preprint, arXiv:0810.3557 (2008).
- [Kir05] K. A. Kirkpatrick. *The schrödinger-hjw theorem*. Found. Phys. Lett. **19**, 95 (2005).
- [Kit87] C. Kittel. *Quantum Theory of Solids*. Wiley, New York, 1987.
- [Kit03] A. Yu. Kitaev. *Fault-tolerant quantum computation by anyons*. Ann. Phys. **303**, 2 (2003).
- [Kit06] A. Kitaev. *Anyons in an exactly solved model and beyond*. Annals of Physics **321**, 2 (2006).
- [KKR06] J. Kempe, A. Kitaev, and O. Regev. *The complexity of the local hamiltonian problem*. SIAM J. Comput. **35**, 1070 (2006).
- [Kog79] J. B. Kogut. *An introduction to lattice gauge theory and spin systems*. Rev. Mod. Phys. **51**, 659 (1979).
- [Kol09] V. Kolmogorov. *Blossom V: a new implementation of a minimum cost perfect matching algorithm*. Math. Prog. Comp. **1**, 43 (2009).
- [LCD⁺87] A. J. Leggett, S. Chakravarty, A. T. Dorsey, M. P. A. Fisher, A. Garg, and W. Zwerger. *Dynamics of the dissipative two-state system*. Rev. Mod. Phys. **59**, 1 (1987).
- [LDG92] D. Loss, D. P. DiVincenzo, and G. Grinstein. *Suppression of tunneling by interference in half-integer-spin particles*. Phys. Rev. Lett. **69**, 3232 (1992).
- [LOSU06] R. Lohmayer, A. Osterloh, J. Siewert, and A. Uhlmann. *Entangled three-qubit states without concurrence and three-tangle*. Phys. Rev. Lett. **97**, 260502 (2006).

- [Man02] J. H. Manton. *Optimization algorithms exploiting unitary constraints*. IEEE Trans. Signal Process. **50**, 635 (2002).
- [MCKB05] F. Mintert, A. R. R. Carvalho, M. Kuś, and A. Buchleitner. *Measures and dynamics of entangled states*. Phys. Rep. **415**, 207 (2005).
- [Mer90] N. D. Mermin. *Quantum mysteries revisited*. Am. J. Phys. **58**, 731 (1990).
- [Mer93] N. D. Mermin. *Hidden variables and the two theorems of John Bell*. Rev. Mod. Phys. **65**, 803 (1993).
- [Mer07] N. D. Mermin. *Quantum Computer Science: An Introduction*. Cambridge University Press, Cambridge, 2007.
- [Mez07] F. Mezzadri. *How to generate random matrices from the classical compact groups*. Notices of the AMS **54**, 592 (2007).
- [MKB05] F. Mintert, M. Kuś, and A. Buchleitner. *Concurrence of mixed multipartite quantum states*. Phys. Rev. Lett. **95**, 260502 (2005).
- [MRR⁺53] N. Metropolis, A. W. Rosenbluth, M. N. Rosenbluth, A. H. Teller, and E. Teller. *Equations of state calculations by fast computing machines*. J. Chem. Phys. **21**, 1087 (1953).
- [MW02] D. A. Meyer and N. R. Wallach. *Global entanglement in multiparticle systems*. J. Math. Phys. **43**, 4273 (2002).
- [NC00] M. A. Nielsen and I. L. Chuang. *Quantum Computation and Quantum Information*. Cambridge University Press, New York, 2000.
- [NO08] Z. Nussinov and G. Ortiz. *Autocorrelations and thermal fragility of anyonic loops in topologically quantum ordered systems*. Phys. Rev. B **77**, 064302 (2008).
- [NO09] Z. Nussinov and G. Ortiz. *A symmetry principle for topological quantum order*. Annals of Physics **324**, 977 (2009).
- [NW99] J. Nocedal and S. J. Wright. *Numerical Optimization*. Springer, 1999.
- [Ohz09] M. Ohzeki. *Locations of multicritical points for spin glasses on regular lattices*. Phys. Rev. E **79**, 021129 (2009).
- [PCL11] F. L. Pedrocchi, S. Chesi, and D. Loss. *Quantum memory coupled to cavity modes*. Phys. Rev. B **83**, 115415 (2011).

- [PGCZ95] T. Pellizzari, S. A. Gardiner, J. I. Cirac, and P. Zoller. *Decoherence, continuous observation, and quantum computing: A cavity qed model*. Phys. Rev. Lett. **75**, 3788 (1995).
- [PKSC09] F. Pastawski, A. Kay, N. Schuch, and I. Cirac. *How long can a quantum memory withstand depolarizing noise?* Phys. Rev. Lett. **103**, 080501 (2009).
- [PKSC10] F. Pastawski, A. Kay, N. Schuch, and I. Cirac. *Limitations of passive protection of quantum information*. Quantum Inf. Comput. **10**, 580 (2010).
- [Pre98] J. Preskill. *Reliable quantum computers*. Proc. R. Soc. London, Ser. A **454**, 385 (1998).
- [PTVF92] W. H. Press, S. A. Teukolsky, W. T. Vetterling, and B. P. Flannery. *Numerical Recipes in C: The Art of Scientific Computing*. Cambridge University Press, New York, NY, USA, 1992.
- [PV07] M. B. Plenio and S. Virmani. *An introduction to entanglement measures*. Quant. Inf. Comp. **7**, 1 (2007).
- [RBB03] R. Raussendorf, D. E. Browne, and H. J. Briegel. *Measurement-based quantum computation on cluster states*. Phys. Rev. A **68**, 022312 (2003).
- [RF10] T. Radtke and S. Fritzsche. *Simulation of n -qubit quantum systems. v. quantum measurements*. Comp. Phys. Comm. **181**, 440 (2010).
- [RR02] A. K. Rajagopal and R. W. Rendell. *Robust and fragile entanglement of three qubits: Relation to permutation symmetry*. Phys. Rev. A **65**, 032328 (2002).
- [Sch35] E. Schrödinger. *Die gegenwärtige situation in der quantenmechanik*. Naturwissenschaften **23**, 823 (1935).
- [Sco04] A. J. Scott. *Multipartite entanglement, quantum-error-correcting codes, and entangling power of quantum evolutions*. Phys. Rev. A **69**, 052330 (2004).
- [SDV08] K. P. Schmidt, S. Dusuel, and J. Vidal. *Emergent fermions and anyons in the Kitaev model*. Phys. Rev. Lett. **100**, 057208 (2008).
- [She96] J. R. Shewchuk. *Triangle: Engineering a 2D quality mesh generator and Delaunay triangulator*. In Ming C. Lin and Dinesh Manocha, editors, *Applied Computational Geometry: Towards Geometric Engineering*, volume 1148 of *Lecture Notes in Computer Science*, page 203. Springer-Verlag, 1996. From the First ACM Workshop on Applied Computational Geometry.

- [Sho97] P. W. Shor. *Polynomial-time algorithms for prime factorization and discrete logarithms on a quantum computer*. SIAM J. Sci. Statist. Comput. **26**, 1484 (1997).
- [SL07] P. Simon and D. Loss. *Nuclear spin ferromagnetic phase transition in an interacting two dimensional electron gas*. Phys. Rev. Lett. **98**, 156401 (2007).
- [SPIbuR11] C. Stark, L. Pollet, A. Imamoglu, and R. Renner. *Localization of toric code defects*. Phys. Rev. Lett. **107**, 030504 (2011).
- [Ste96] A. M. Steane. *Multiple-particle interference and quantum error correction*. Proc. R. Soc. Lond. A **452**, 2551 (1996).
- [Ter00] B. Terhal. *Bell inequalities and the separability criterion*. Phys. Lett. A **271**, 319 (2000).
- [TGL08] M. Trif, V. N. Golovach, and D. Loss. *Spin dynamics in inas nanowire quantum dots coupled to a transmission line*. Phys.Rev. B **77**, 045434 (2008).
- [THLD02] B. M. Terhal, M. Horodecki, D. W. Leung, and D. P. DiVincenzo. *The entanglement of purification*. J. Math. Phys. **43**, 4286 (2002).
- [TKPS10] I. S. Tupitsyn, A. Kitaev, N. V. Prokof'ev, and P. C. E. Stamp. *Topological multicritical point in the phase diagram of the toric code model and three-dimensional lattice gauge higgs model*. Phys. Rev. B **82**, 085114 (2010).
- [TOC11] D. I. Tsomokos, T. J. Osborne, and C. Castelnovo. *Interplay of topological order and spin glassiness in the toric code under random magnetic fields*. Phys. Rev. B **83**, 075124 (2011).
- [TTSL08] M. Trif, F. Troiani, D. Stepanenko, and D. Loss. *Spin-electric coupling in molecular magnets*. Phys. Rev. Lett. **101**, 217201 (2008).
- [TTSL10] M. Trif, F. Troiani, D. Stepanenko, and D. Loss. *Spin electric effects in molecular antiferromagnets*. Phys. Rev. B **82**, 045429 (2010).
- [TV00] B. M. Terhal and K. G. H. Vollbrecht. *Entanglement of formation for isotropic states*. Phys. Rev. Lett. **85**, 2625 (2000).
- [TWT⁺07] S. Trebst, P. Werner, M. Troyer, K. Shtengel, and C. Nayak. *Breakdown of a topological phase: Quantum phase transition in a loop gas model with tension*. Phys. Rev. Lett. **98**, 070602 (2007).

- [Uhl00] A. Uhlmann. *Fidelity and concurrence of conjugated states*. Phys. Rev. A **62**, 032307 (2000).
- [UTSM⁺07] R. Ursin, F. Tiefenbacher, T. Schmitt-Manderbach, H. Weier, T. Scheidl, M. Lindenthal, B. Blauensteiner, T. Jennewein, J. Perdigues, P. Trojek, B. Ömer, M. Fürst, M. Meyenburg, J. Rarity, Z. Sodnik, C. Barbieri, H. Weinfurter, and A. Zeilinger. *Entanglement-based quantum communication over 144 km*. Nature Phys. **3**, 481 (2007).
- [VDS09] J. Vidal, S. Dusuel, and K. P. Schmidt. *Low-energy effective theory of the toric code model in a parallel magnetic field*. Phys. Rev. B **79**, 033109 (2009).
- [Ved07] V. Vedral. *Introduction to Quantum Information Science*. Oxford University Press, New York, 2007.
- [VT99] G. Vidal and R. Tarrach. *Robustness of entanglement*. Phys. Rev. A **59**, 141 (1999).
- [VTSD09] J. Vidal, R. Thomale, K. P. Schmidt, and S. Dusuel. *Self-duality and bound states of the toric code model in a transverse field*. Phys. Rev. B **80**, 081104 (2009).
- [Weg71] F. Wegner. *Duality in generalized ising models and phase transitions without local order parameters*. J. Math. Phys. **12**, 2259 (1971).
- [Wen03] X.-G. Wen. *Quantum orders in an exact soluble model*. Phys. Rev. Lett. **90**, 016803 (2003).
- [Wer89] R. F. Werner. *Quantum states with Einstein-Podolsky-Rosen correlations admitting a hidden-variable model*. Phys. Rev. A **40**, 4277 (1989).
- [WG03] T.-C. Wei and P. M. Goldbart. *Geometric measure of entanglement and applications to bipartite and multipartite quantum states*. Phys. Rev. A **68**, 042307 (2003).
- [WML⁺10] H. Weimer, M. Müller, I. Lesanovsky, P. Zoller, and H. P. Büchler. *A rydberg quantum simulator*. Nat. Phys. **6**, 382 (2010).
- [Wol08] M. M. Wolf. *Quantum many-body theory: Divide, perturb and conquer*. Nat. Phys. **4**, 834 (2008).
- [Woo98] W. K. Wootters. *Entanglement of formation of an arbitrary state of two qubits*. Phys. Rev. Lett. **80**, 2245 (1998).

- [WP11] J. R. Wootton and J. K. Pachos. *Bringing order through disorder: Localization of errors in topological quantum memories*. Phys. Rev. Lett. **107**, 030503 (2011).
- [WSB⁺04] A. Wallraff, D. I. Schuster, A. Blais, L. Frunzio, R.-S. Huang, J. Majer, S. Kumar, S. M. Girvin, and R. J. Schoelkopf. *Strong coupling of a single photon to a superconducting qubit using circuit quantum electrodynamics*. Nature **431**, 162 (2004).

Curriculum Vitae

Beat Röthlisberger

Date of birth: November 30, 1981

Place of birth: Basel, Switzerland

Education

- 2006-2011 PhD in Theoretical Physics
University of Basel, Switzerland
Advisor: Prof. Daniel Loss
Thesis: *Entanglement Generation and Self-Correcting Quantum Memories*
- 2001-2006 Master of Science in Physics
University of Basel, Switzerland
Advisor: Prof. Daniel Loss
Thesis: *Tripartite Entanglement Measures: Highly Entangled Spin States in Triple Quantum Dot Systems*
- 1997-2000 Matura (Swiss highschool diploma)
Gymnasium Muttenz, Switzerland

List of Publications

An asterisk indicates a publication covered in this thesis.

- * B. Röthlisberger, J. Lehmann, D. S. Saraga, P. Traber, and D. Loss, “*Highly Entangled Ground States in Tripartite Qubit Systems*”, *Phys. Rev. Lett.* **100**, 100502 (2008).
- * B. Röthlisberger, J. Lehmann, and D. Loss, “*Numerical evaluation of convex-roof entanglement measures with applications to spin rings*”, *Phys. Rev. A* **80**, 042301 (2009).
- R. A. Žak, B. Röthlisberger, S. Chesi, and D. Loss, “*Quantum Computing with Electron Spins in Quantum Dots*”, *La Rivista del Nuovo Cimento* **33**, 7 (2010).
- * S. Chesi, B. Röthlisberger, and D. Loss, “*Self-correcting quantum memory in a thermal environment*”, *Phys. Rev. A* **82**, 022305 (2010).
- * B. Röthlisberger, J. Lehmann, and D. Loss, “*libCreme: An optimization library for evaluating convex-roof entanglement measures*”, *Comput. Phys. Commun.* **183**, 155 (2012).
- * B. Röthlisberger, J. R. Wootton, R. M. Heath, J. K. Pachos, and D. Loss, “*Incoherent dynamics in the toric code subject to disorder*”, *Phys. Rev. A* **85**, 022313 (2012).
- A. Hutter, J. R. Wootton, B. Röthlisberger, and D. Loss, “*Self-correcting quantum memory with a boundary*”, arXiv:1206.0991 (2012).